Doctoral Dissertation

Studies on Photocatalytic Activity of Semiconductor Composites for Hydrogen Generation Based on Charge Transfer Kinetics under Solar Light Irradiation

SHI XIAOWEI

June 2018

Division of Applied Chemistry
Graduate School of Engineering,
Osaka University

Preface

The studies presented in this thesis were carried out under the direction of Professor Tetsuro Majima, the Institute of Scientific and Industrial Research (SANKEN), Osaka University during October 2015 to September 2018.

The subject of this thesis is the photocatalytic activity of semiconductor composites for hydrogen generation under light irradiation. The aim of this research is to resolve the problems due to intrinsic wide band gap of TiO_2 by incorporating with noble metal nanoparticle and forming unique structure, and low photocatalytic efficiency of pure semiconductor via facilely fabricating heterostructure and utilizing co-catalyst. In addition, the detailed charge transfer kinetics are investigated. The author hopes that the results and conclusions presented in this thesis could contribute to the further improvement of quantum efficiency for practical application, which will deepen our understanding of influence factors on photocatalytic reactions and help us to resolve the energy shortage and environment crisis.

SHI XIAOWEI

Department of Applied Chemistry
Graduate School of Engineering
Osaka University
2018

Contents

General Introduction

Increased environmental crisis and energy drought have promoted the development of new technologies to harvest energy from solar light. Significant efforts have been devoted to nanostructured semiconductors as building blocks for conversion of solar energy to a viable form. Among the wide variety of green earth and renewable energy projects underway, semiconductor photocatalysis has emerged as one of the most promising technologies because it represents an easy way to utilize the energy of either natural sunlight or artificial indoor illumination, and is thus abundantly available everywhere in the world. Therefore, the photocatalytic reactions are widely employed in many application fields such as (I) photolytic reduction/oxidization of water to generate hydrogen and/or oxygen; (II) photodecomposition or photooxidization of harmful substances; (III) artificial photosynthesis; (IV) photo(electro)-chemical conversion (CO_2 reduction and N_2 fixation), etc.[1-4] Usually in semiconductors, the conduction band electrons have a chemical potential of +0.5 to -1.5V versus the normal hydrogen electrode (NHE), which can act as reductants. While the valence band holes possess a strong oxidative potential of +1.0 to +3.5 V versus NHE.[5] At beginning, the energy of incident photons is stored in semiconductor as electron-hole pairs during the irradiation process and then converted to chemical forms by a series of chemical processes and surface/interface reactions. Contrary to the thermodynamics of traditional catalysis, not only spontaneous reactions ($\Delta G < 0$) but also non-spontaneous reactions ($\Delta G > 0$) could also be promoted by photocatalyst.[4]

Due to the highest specific energy of combustion in all chemical fuels and production of water as a combustion product, hydrogen is therefore regarded as one possible contender for resolving future fuel crisis. The evolution of hydrogen using sunlight is an attractive and sustainable solution to global energy and environmental problems.[6,7] Since the discovery of photo-assisted water splitting by Fujishima and Honda, splitting water using solar energy has attracted a significant attention and extensively studies have been performed.[8-10] Hundreds of novel semiconductor materials are now available

for diversified and multifunctional applications, including oxides of the metallic elements with d^0 and d^{10} configurations,[11] sulfides,[12] (oxy)nitrides,[13,14] metal-free semiconductors,[15] plasmonic metals[16] and elemental photocatalysts.[17]

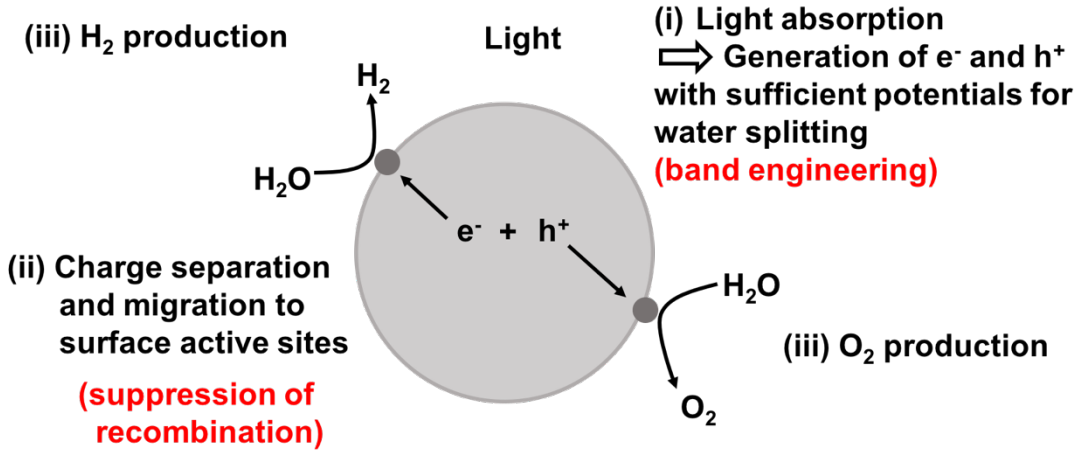

Figure 1 Schematic illustration of basic processes of a semiconductor photocatalytic processes for hydrogen/oxygen generation.

In general, a typical photocatalytic reduction/oxidization to generate hydrogen/oxygen mainly contains three steps, as shown in Figure 1. Firstly, under the light irradiation, electrons will transit from the valence band to conduction band, leaving an equal number of vacant sites (holes) in semiconductors. Then the excited electrons and holes would migrate from the inner part to active sites on the surface of semiconductors. Finally, these electrons and holes could react with H_2O molecules to form hydrogen and/or oxygen at the active sites on the semiconductors. The process of water splitting is well known as a typical "uphill reaction", involving a large positive change in the Gibbs energy ($\Delta G° = 237.13$ kJ mol^{-1}), corresponding to a photon energy of 1.23 eV. However, in fact, due to an activation barrier in the charge transfer process between the photocatalyst and H_2O molecules, it is usually necessary for the photon energy to be greater than the bandgap of the semiconductor to drive the water splitting reaction.[18] Due to the booming of nanotechnology, nanomaterials have emerged as pioneering photocatalysts and accounted for most of the current research. Nanomaterials can provide large surface areas with abundant active sites for photocatalytic reactions, diverse morphologies, and easy device modeling, all of which are properties beneficial to photocatalysis.[19-29] The efficiency of photon utilization and

the limitation of selection of oxidation-reduction reaction, however, still restrict the improvement of water splitting activity of nanomaterial semiconductor photocatalysts. Therefore, improving their photocatalytic activity in order to meet engineering requirements is strongly urgent. In addition, the stability and the cost of these materials should also be considered carefully.

The first key point relevant to the photocatalytic activity of a semiconductor is its energy band configuration, which determines whether it could absorb incident light to generate electron-hole pairs and the redox capabilities of excited state electrons and holes.[30] Therefore, band engineering or band tuning is a quite commonly used method and fundamental aspect of designing and fabricating semiconductor photocatalysts. In order to modulate the bandgap and band-edge positions precisely, both introducing a new kind of elements and solid solution strategies have been extensively explored and applied.[31-35] However, the recombination probability for photo-induced electron-hole pairs would increase if the amount of newly introduced elements is high. Except from doping, noble metal nanoparticles such as Au and Ag have also been frequently used to expand the absorption range of wide bandgap semiconductors and improve charge separation by taking advantage of their unique plasmonic properties.[36-38] What is more, fabricating so-called "hierarchical photocatalysts", referring to the nanostructured semiconductors with various dimensional domains or multimodal pores, could also enhance the efficiency of light harvesting even for the same semiconductor with other shapes.

Another key issue influencing the photocatalytic activity of a semiconductor is that a large proportion of electron-hole pairs would recombine in the second step during their migration from inner part to surface, which dissipates the input energy in the form of heat or light emission. In order to inhibit this recombination of electron-hole pairs, heterostructures or heterojunctions are designed between the host semiconductor and another semiconductor (or co-catalyst). This kind of structure could provide an internal electric field which promotes the separation of electron-hole pairs and induces faster carrier migration. In addition, the nature of surface/interface chemistry of photocatalysts is also an important issue which influences their activity. The surface

active sites and chemisorption properties play crucial roles in the transfer of electrons and in governing the selectivity, rate and overpotential of redox reactions on the photocatalyst surface.[39,40] For example, the hydrogen reduction photocatalyst cannot only reduce H^+ ions to form H_2 but also can reduce the shuttle redox mediator. More importantly, most semiconductor photocatalysts cannot offer active sites for catalytic reactions on the surface, which exhibit a relative low hydrogen evolution reaction even in the presence of sacrificial electron donor. To overcome these disadvantages, co-catalysts are commonly used because of better conductivity, lower overpotential and higher catalytic activity than host semiconductor, which could act as ideal active sites for photocatalytic reactions to take place.

Apart from the important insight being gained, detailed mechanisms involved in photocatalysis are still not fully understood. In order to fulfill this goal, single-particle photoluminescence spectroscopy (SPS) and femtosecond time-resolved transient absorption (fs-TAS) are used as valuable tools in photocatalysis field in recent years because they play significant roles in understanding fundamental photophysical processes and how charge transfer dictates photoactivities. By employing SPS, fluorescence lifetime experiments using pulsed lasers and a time-correlated single-photon counting system are possible.[41,42] By measuring the delay between the arrival time of the excitation pulse and the detection of the emitted photon, it is also to reconstruct a fluorescence decay curve for a semiconductor particle in the excited state. These techniques for SPS detection possess superior advantages compared with conventional ones that rely on the bulk sample, offering us with opportunities, such as the ultimate high sensitivity, the possible observations of the properties hidden in the ensemble measurements. In fs-TAS, a pump pulse is employed to excite the sample, followed by a probe pulse to measure the absorption differences with the ground state sample as a function of time. The accessible range of delay between pump and probe sets the time scales that can be studied.

In this dissertation, a series of methods to enhance the photocatalytic activities for H_2 evolution of semiconductor-based composites under solar light irradiation were investigated. Charge-separation, trapping and recombination processes which were

essential to explain the photocatalytic activity were carefully investigated.

Content of each chapter is shown as below.

In Chapter 1, Au-TiO_2 and 3D-array were fabricated to carefully explore the multi-scattering effect on photocatalytic activity of H_2 generation. 3D-array exhibited a much higher photocatalytic activity of H_2 generation (3.5 folds under visible light irradiation, 1.4 folds under solar light irradiation) than Au-TiO_2. According to the single-particle plasmonic photoluminescence measurement, it was suggested that the hot electrons generated by AuNS under visible light irradiation was responsible for the photocatalytic H_2 evolution process. The enhanced activity of 3D-array is due to the elongation of light path length because of multi-scattering in-between Au-TiO_2.

In Chapter 2, a facile impregnated method was employed to synthesize products gradually varying from N-TiO_2 to N-TCN-x by mixing and calcining TiO_2 hollow nanospheres with cyanamide. Due to the mesoporous structure of TiO_2, g-C_3N_4 was formed both inside and outside of nanospheres. In addition, formation of g-C_3N_4 outside of TiO_2 small grains (3 nm) restrained their recrystallization to large particles (20 nm). Among series of N-TCN-x, N-TCN-700 exhibited the best photocatalytic activity with H_2 evolution of 296.4 μmol g^{-1} h^{-1} under visible light irradiation ($\lambda \geq 420$ nm) without any co-catalyst. Charge carrier lifetimes of N-TCN-x were measured by femtosecond time-resolved diffused reflectance spectroscopy and indicated that photogenerated electrons in CB of g-C_3N_4 transferred to that of N-TiO_2 within several to tens picoseconds, leading to an efficient charge separation and enhanced photocatalytic activity.

In Chapter 3 part 1, facile processes were developed to synthesize g-C_3N_4-based hybrid photocatalysts containing different MoS_2 structures as co-catalyst, nanodot and monolayer. Photocatalytic H_2 evolution activity of g-C_3N_4 with 3.2 wt% MoS_2 (MC-3.2%) is 660 μmol g^{-1} h^{-1} under visible light irradiation, which is 7.9 times higher than that of Mix-6.4% (83.8 μmol g^{-1} h^{-1}). Single-particle photoluminescence measurement demonstrated that MoS_2 had a much higher quenching efficiency compared with monolayer MoS_2. Detailed charge carrier dynamics of g-C_3N_4, MC-3.2%, and Mix-6.4% measured by femtosecond time-resolved diffused reflectance spectroscopy indicated

that the electron injection took place within 1.7 ps in MC-3.2% compared to 4.0 ps in Mix-6.4% and the injection efficiencies were 73.3% and 36.1% in MC-3.2% and Mix-6.4%, respectively. In addition, MoS_2 nanodots with small particle size contained more unsaturated active S atoms than MoS_2 monolayer, which could adsorb more H^+ ions.

In Chapter 3 part 2, quaternary sulfur semiconductor $Zn_{0.4}Ca_{0.6}In_2S_4$ (ZCIS) microspheres composed of cross-linked nanosheets and ZCIS microspheres modified with MoS_2 were designed and prepared *via* hydrothermal methods. Detailed characterizations indicated that the layer structured MoS_2 nanosheets were mainly deposited on the surface of ZCIS nanosheet to form a 2D-2D structure which greatly increased the contact surface area beneficial to charge transfer. It is demonstrated that ZM-3.0 (ZCIS with 3 wt% MoS_2 loading amount) exhibited the fastest electron injection within only 1.1 ps and the highest efficient injection efficiency of 70%. As a result, ZM-3.0 exhibited the H_2 evolution rate of 3.5 μmol h^{-1} under visible light irradiation ($\lambda \geq 420$ nm), which is 27 times higher than that of pure ZCIS (0.13 μmol h^{-1}).

Reference

(1) Hoffmann, M. R.; Martin, S. T.; Choi, W.; Bahnemann, D. W. *Chem. Rev.* **1995**, *95*, 69.

(2) Chen, X.; Mao, S. S. *Chem. Rev.* **2007**, *107*, 2891.

(3) Chen, X.; Shen, S.; Guo, L.; Mao, S. S. *Chem. Rev.* **2010**, *110*, 6503.

(4) Tong, H.; Ouyang, S.; Bi, Y.; Umezawa, N.; Oshikiri, M.; Ye, J. *Adv. Mater.* **2012**, 24, 229.

(5) Fox, M. A.; Dulay, M. T. *Chem. Rev.* **1993**, 93, 341.

(6) Xie, J. F.; Zhang, J. J.; Li, S.; Grote, F.; Zhang, X. D.; Zhang, H.; Wang, R. X.; Lei, Y.; Pan, B. C.; Xie, Y. *J. Am. Chem. Soc.* **2013**, 135, 17881.

(7) Lukowski, M. A.; Daniel, A. S.; Meng, F.; Forticaux, A.; Li, L. S.; Jin, S. *J. Am. Chem. Soc.* **2013**, 135, 10274.

(8) Fujishima, A.; Honda, K. *Nature* **1972**, 238, 37.

(9) Zou, Z. G.; Ye, J. H.; Sayama, K.; Arakawa, H. *Nature* **2001**, 414, 625.

(10) Li, X. B.; Gao, Y. J.; Wang, Y.; Zhan, F.; Zhang, X. Y.; Kong, Q. Y.; Zhao, N. J.; Guo, Q.; Wu, H. L.; Li, Z. J.; Tao, Y.; Zhang, J. P.; Chen, B.; Tung, C. H.; Wu, L. Z. *J. Am. Chem. Soc.* **2017**, 139, 4789-4796.

(11) Maeda, K.; Domen, K. *J. Phys. Chem. C* **2007**, 111, 7851.

(12) Liu, M.; Jing, D.; Zhou, Z.; Guo, L. *Nat. Commun.* **2013**, 4, 2278.
(13) Maeda, K.; Takata, T.; Hara, M.; Saito, N.; Inoue, Y.; Kobayashi, H.; Domen, K. *J. Am. Chem. Soc.* **2005**, 127, 8286.
(14) Maeda, K.; Teramura, K.; Lu, D.; Takata, T.; Saito, N.; Inoue, Y.; Domen, K. *Nature* **2006**, 440, 295.
(15) Liu, J.; Liu, Y.; Liu, N.; Han, Y.; Zhang, X.; Huang, H.; Lifshitz, Y.; Lee, S.-T.; Zhong, J.; Kang, Z. *Science* **2015**, 347, 970.
(16) Li, B. X.; Gu, T.; Ming, T.; Wang, J. X.; Wang, P.; Wang, J. F.; Yu, J. C. *ACS Nano* **2014**, 8, 8152.
(17) Liu, G.; Niu, P.; Yin, L.; Cheng, H.-M. *J. Am. Chem. Soc.* **2012**, 134, 9070.
(18) Kudo, A.; Miseki, Y. *Chem. Soc. Rev.* **2009**, 38, 253.
(19) Pan, J. H.; Han, G.; Zhou, R.; Zhao, X. *Chem. Commun.* **2011**, 47, 6942.
(20) Li, Q. Y.; Yue, B.; Iwai, H.; Kako, T.; Ye, J. H. *J. Phys. Chem. C* **2010**, 114, 4100.
(21) Kamat, P. V.; *J. Phys. Chem. C* **2007**, 111, 2834.
(22) Chen, D.; Ye, J. H. *Chem. Mater.* **2007**, 19, 4585.
(23) Zeng, H. B.; Liu, P. S.; Cai, W. P.; Yang, S. K.; Xu, X. X. *J. Phys. Chem. C* **2008**, 112, 19620.
(24) Chen, D.; Ye, J. H. *Chem. Mater.* **2009**, 21, 2327.
(25) Tong, H.; Ye, J. H. *Eur. J. Inorg. Chem.* **2010**, 1473.
(26) Zeng, H. B.; Cai, W. P.; Liu, P. S.; Xu, X. X.; Zhou, H. J.; Klingshirn, C. *ACS Nano* **2008**, 2 1661.
(27) Li, J.; Li, H.; Zhan, G.; Zhang, L. *Acc. Chem. Res.* **2017**, 50, 112.
(28) Godin, R.; Wang, Y.; Zwijnenburg, M. A.; Tang, J.; Durrant, J. R. *J. Am. Chem. Soc.* **2017**, 139, 5216.
(29) Wu, B.; Liu, D.; Mubeen, S.; Chuong, T. T.; Moskovits, M.; Stucky, G. D. *J. Am. Chem. Soc.* **2016**, 138, 1114.
(30) Zhao, W.; Ma, W.; Chen, C.; Zhao, J.; Shuai, Z. *J. Am. Chem. Soc.* **2004**, 126, 4782.
(31) Zhang, P.; Tachikawa, T.; Fujitsuka, M.; Majima, T. *ChemSusChem* **2016**, 9, 617.
(32)Chen, X.; Burda, C. *J. Am. Chem. Soc.* **2008**, 130, 5018.
(33) Maeda, K.; Domen, K. *Chem. Mater.* **2010**, 22, 612.
(34) Liu, X.; Zhu, G.; Wang, X.; Yuan, X.; Lin, T.; Huang, F. *Adv. Energy Mater.* **2016**, 6, 1600452.
(35) Wang, D. F.; Kako, T.; Ye, J. H. *J. Am. Chem. Soc.* **2008**, 130, 2724.
(36) Jiang, Z.; Lv, X.; Jiang, D.; Xie, J.; Mao, D. *J. Mater. Chem. A* **2013**, 1, 14963.
(37) Shi, X.; Ji, Y.; Hou, S.; Liu, W.; Zhang, H.; Wen, T.; Yan, J.; Song, M.; Hu, Z.; Wu, X. *Langmuir* **2015**, 31, 1537-1546.
(38) Gu, Q.; Long, J.; Zhuang, H.; Zhang, C.; Zhou, Y.; Wang, X. *Phys. Chem. Chem. Phys.* **2014**, 16, 12521-12534.

(39) Thompson, T. L.; Yates, J. T. *Chem. Rev.* **2006**, 106, 4428.
(40) Osgood, R. *Chem. Rev.* **2006**, 106, 4379.
(41) Li, L. Q.; Davis, L. M. *Rev. Sci. Instrum.* **1993**, 64, 1524.
(42) Macklin, J. J.; Trautman, J. K.; Harris, T. D.; Brus, L. E. *Science* **1996**, 272, 255.

Chapter 1. 3D-array of Au-TiO_2 Yolk-shell as Plasmonic Photocatalyst Boosting Multi-Scattering with Enhanced Hydrogen Evolution

1. Introduction

From the environmental points of view, solar energy becomes a promising alternative energy to resolve the energy shortages.[1-4] Hence, various strategies have been developed for utilizing solar light, and among them, photocatalysis is the most attractive one.[5] However, the conversion efficiency is not high enough and how to enhance the photocatalytic activity is still a significant issue. In order to overcome this problem, many approaches have been proposed and examined. Among them, fabricating unique structures with efficient light absorption to generate more electron-hole pairs is quite important, because the first step of photocatalysis is the formation of electron-hole pairs under light irradiation.[6,7] It has been proved that Mie's scattering could increase the light path length, which leads to higher efficient utilization of incident light.[7]

Light can be scattered and redirected to almost all directions. Particularly, when the scattering centers are grouped together, light can be scattered many times (multi-scattering). Multi-scattering in-between nanoparticles is greatly dependent on the shape of nanoparticles and the distance between nanoparticles.[8] When we introduce the multi-scattering phenomenon into three dimensional (3D) nanostructure, light could collide with these particles having comparable structure and scatter inside of the particles. Therefore, the path length of incident light would increase in these particles, enhancing the light absorption efficiency. In this case, fabricating proper structures with suitable shape and inter nanoparticle spacing is a great challenge to clear the multi-scattering effect on photocatalytic activity. The multi-scattering phenomenon has been applied in the dye-sensitized solar cells (DSSC) before,[9,10] however, to the best of our knowledge, there are few studies available on the multi-scattering effect in the application of H_2 evolution.

In the present study, monodispersed gold nanosphere (AuNS) TiO_2 yolk-shell

nanosphere (Au-TiO_2) was synthesized by multi-step SiO_2 protection method. Then this nanosphere were acted as building blocks for fabricating unique 3D assembled array of Au-TiO_2 (3D-array), which was applied for the plasmonic photocatalyst of H_2 generation. After encapsulating AuNS with strong SPR, the absorption of TiO_2 is extended to visible region. Multi-scattering effect on the photocatalytic activity was investigated by comparing H_2 generation under different-wavelength light irradiation. The results showed that 3D-array exhibited much higher activity than Au-TiO_2 under both visible and simulated solar light irradiation. Single-particle plasmonic fluorescence measurement and computational calculation using FDTD method were performed to elucidate the detailed mechanisms. Our result is the first report to clearly show the multi-scattering effect on the photocatalytic activity.

2. Experimental Section

Materials. Chloroauric acid ($HAuCl_4 \bullet 4H_2O$, 99.99%), sodium citrate tribasic dehydrate (98%), 4-mercaptobenzoic acid (4-MBA 90%), ammonium hydroxide (28-30%), tetraethylortosilicate (TEOS, 98%), hydrogen hexachloroplatinate hydrate ($H_2PtCl_6 \bullet nH_2O$, 99.9%), tetrabutyl titanate (TBOT 99%), polyvinylpyrrolidone (PVP, M_w ~ 40000. 2-propanol (99%); absolute ethanol and Milli-Q water were used as solvents.

Preparation of Au@SiO_2@TiO_2@SiO_2 nanospheres. Au@citrate spheres (~50 nm av. diameter 20 mL, [Au]=164 ppm) were prepared as previously reported,[18] centrifuged at 3500 rpm for 20 min and dispersed again in water (12 mL). The seeds were added dropwise under vortex stirring to a mixture of 2-propanol (48 mL) and H_2O (16 mL), containing 4-MBA (560 μL, 5 Mm in ethanol). After stirring for about 1 h to induce self-assembly of the ligands over the surface, ammonium hydroxide (2.4 mL) was added under fast stirring, followed by dropwise addition of TEOS (6 mL, 89.6 mM in 2-propanol), and was stored for ~12 h under slow stirring.

The achieved Au@SiO_2 nanospheres were dispersed in a mixture of ethanol (25 mL) and acetonitrile (7 mL) under stirring. After adding ammonia aqueous solution (200

μL), TBOT (145 μL) in a mixture of ethanol (3 mL) and acetonitrile (1 mL) was injected into the mixture quickly. After stirring for 3 h, the mixture was centrifuged and washed with water. Above multi-layer particles were dispersed into water containing 20 mg PVP overnight to allow for the adsorption of PVP onto the TiO_2 surface, then separated from solution by centrifugation, and re-dispersed in 10 mL ethanol. The solution of $Au@SiO_2@TiO_2$ was sequentially mixed with ethanol (13 mL), water (4.3 mL), TEOS (200 μL) and aqueous ammonia (620 μL). After stirring for 4 h, the resulting particles were centrifuged, washed with water and dried under 80 ºC in oven.

Calcination, SiO_2 etching and assembling. The multi-layer particles were calcined in air at 800 ºC for 2 h to remove all organic compounds and crystallize the amorphous TiO_2. Then the calcined samples were treated by 10 mL 0.6 M NaOH solution at 60 ºC for 2 h. After etching, the Au-TiO_2 yolk-shell particles were separated equally into two samples and centrifuged several times using water and ethanol. Both of the two samples were re-dispersed into water. One of the samples was kept stirring to make the particles monodispered, while another one was settled undisturbed for several days. The supernatant of the undisturbed sample was taken out and the precipitant was dried under 30 ºC overnight. Then the assembled 3D-array were achieved.

FDTD Calculations. The computational simulations were performed by using the finite-difference-time-domain (FDTD) Solutions 8.11 developed by Lumerical Solutions, Inc. During the simulations, an electromagnetic pulse with a different wavelength range was launched in a box containing a target nanostructure, and the override mesh cell size used was $4\times4\times4$ nm^3. During the calculation, we supposed that all the AuNS were in the same place instead of randomly dispersed. The optical constants of Au and TiO_2 were taken from tabulated values bulk gold measured by Johnson and Christy and Tompkins.[19] The size of Au, yolk-shell cavity and TiO_2 thickness were matched with the average values. The refractive index of the medium was water set to be 1.33.

Photocatalytic Hydrogen Generation Test. 3.734 mL of aqueous solution of Au-TiO_2 yolk-shell particles and assembled sample achieved from same amount of solution (weight of particles is 3 mg) were mixed with 266 μL $H_2PtCl_6 \cdot nH_2O$ solution and 1 mL

methanol. The above samples were firstly bubbled with nitrogen for 30 min to remove the dissolved oxygen and then irradiated by UV-LED source (Asahi Spectra, POT-365; 100 mW cm^{-2}) for 20 min to ensure the deposition of Pt on the surface of TiO_2. Finally, the samples were irradiated at different wavelengths using a Xenon lamp for H_2 generation (Asahi Spectra, HAL-320; 650 mW cm^{-2}). The visible light was filtered with nominal 420 nm cutoff filter, while a simulated daylight irradiation was conducted without any filter. Hydrogen evolution was measured by using Shimadzu GC-8A gas chromatograph equipped with an MS-5A column and a thermal conductivity detector. The apparent quantum efficiency (AQE) for hydrogen evolution at 540 nm wavelength of the monochromatic light with width of ± 5 nm (Asahi Spectra HAL-320; 0.7 mW cm^{-2}) was calculated using the following equation: AQE = (2 × number of number of hydrogen molecules / number of incident photons) × 100%.

Single-Particle PL measurements by Confocal Microscopy. Sample preparation for single-particle photoluminescence (PL) experiments: The cover glasses were purchased from DAICO MFG CO., Ltd. (Japan) and cleaned by sonication in a 20% detergent solution (As One, Cleanace) for 7 h, followed by repeated washing with warm water 5 times. Au-TiO_2 and pure AuNS aqueous suspensions were centrifuged and then re-dispersed in water. The well-dispersed aqueous suspensions of nanospheres were spin-coated on the cleaned cover glass. The cover glass was annealed at 100 ºC for 1 h to immobilize the particles on the surface.

Single-particle PL images and spectra of samples were recorded by using an objective scanning confocal microscope system (PicoQuant, MicroTime 200) coupled with an Olympus, UplanSApochromat, 100×, 1.4 NA) and a circular-polarized 488 nm continuous wave laser controlled by a PDL-800B driver (PicoQuant). Typical excitation power for the PL measurements was 170 μW at the sample. The emission from the sample was collected by the same objective and detected by a single photon avalanche photodiode (Micro Photon Devices, PDM 50 CT) through a dichroic beam splitter (Chroma, 405rdc) and long pass filter (Chroma, HQ430CP). For the spectroscopy, only the emission that passed through a slit entered the imaging spectrograph (Acton Research, SP-2356) that was equipped with an electron-

multiplying charge-coupled device (EMCCD) camera (Princeton Instruments, ProEM). The spectra were typically integrated for 5 s. All the experimental data were obtained at room temperature.

Characterization of Materials. The samples were characterized suing X-ray diffraction (XRD, Rigaku Rint-2500, CuKα source), SEM (JEOL JSM-6330FT), and HRTEM (JEOL JEM 3000F, operated at 300kV). The steady-state UV-visible absorption and diffuse reflectance spectra were measured by UV-visible-NIR spectrophotometers (Shimadzu, UV-3100, and Jasco, V-570, respectively) at room temperature.

3. Results and Discussion

In order to synthesize Au-TiO_2 and 3D-array, two layers of SiO_2 were coated outside of AuNS with one layer as void template and another as protector firstly (Scheme 1). Then the sample was calcined under 800 ºC for 2 h. After etching two layers of SiO_2 by alkaline, the Au-TiO_2 could be achieved.

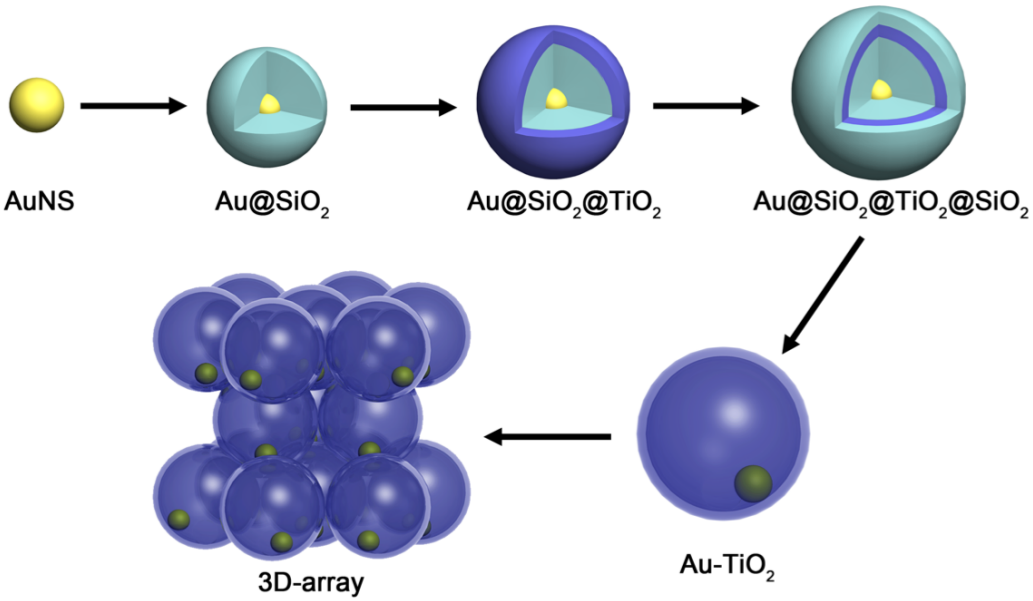

Scheme 1 Schematic illustration of synthesizing Au-TiO_2 and 3D-array.

AuNSs with an average diameter of 51.3 ± 3.8 nm were synthesized by the seed growth method using citrate as stabilizer. Uniform Au-TiO_2 exhibited perfect monodispersibility and high yield without any byproducts (Figures 1A). In addition, TEM image clearly shows that there is a cavity inside of the TiO_2 shell. Amorphous

TiO_2 was crystallized into TiO_2 shell with the extremely small size (approximately 5 nm) after calcination, which is due to the protection of the outside SiO_2 layer. Elemental mapping further confirms that there is only one AuNS in each TiO_2 yolk-shell structure and AuNS is partially attached onto the inner surface of TiO_2 yolk-shell (Figures 1B-E). 3D-assembled array could be fabricated by keeping the monodispersed Au-TiO_2 nanosphere aqueous solution standing undisturbed for one week, as shown in Figure 1F and G. Au-TiO_2 nanospheres were closely packed with each other into a hexagonal structure that is visible over a wide range. The intersection image (Figure 1G) displays that the assembled sample is composed of several layers of Au-TiO_2 particles.

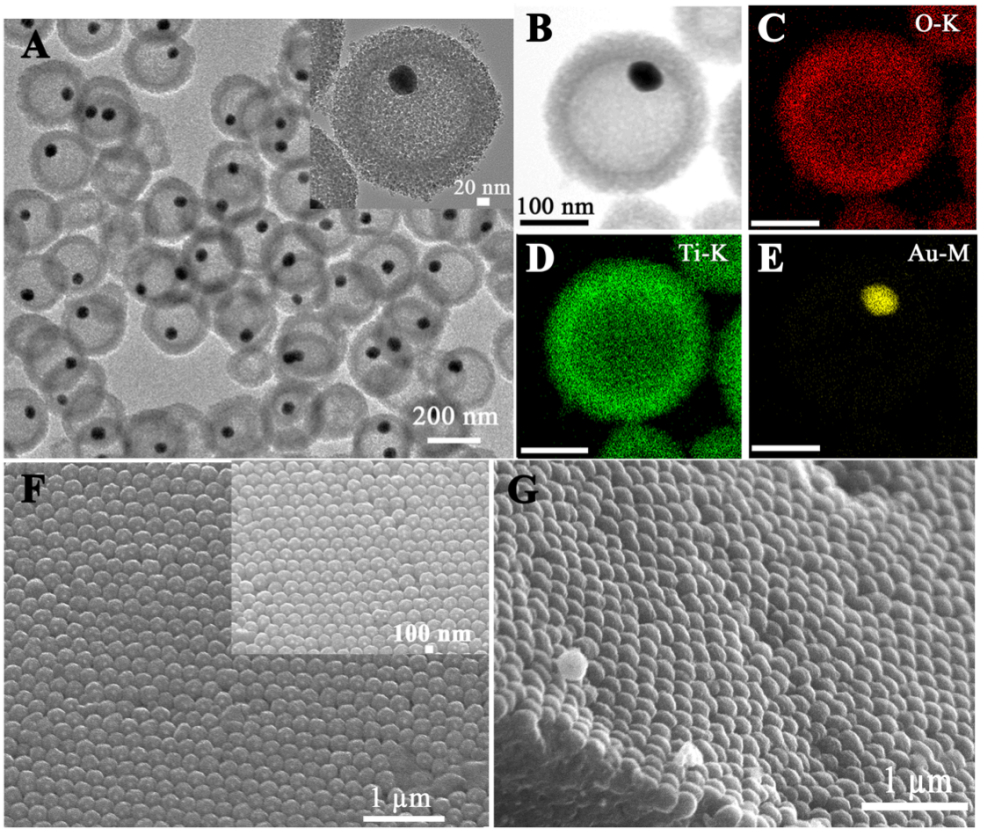

Figure 1 TEM image of Au-TiO_2, inset image is the enlarged one Au-TiO_2 (A). HAADF-STEM image of Au-TiO_2 (B). Elemental mappings of O (C), Ti (D) and Au (E). SEM images of 3D-array, inset is the enlarged image (F). Intersection image of 3D-array (G).

Considering the X-ray diffraction (XRD) pattern of Au-TiO_2 3D-assembled array (Figure 2), two sets of diffraction peaks are present, which could be assigned to the cubic Au phase (PDF 04-0784) and anatase TiO_2 (PDF 21-1272). Interestingly, the peak width of TiO_2 is greatly broadened. This phenomenon is due to the ultrasmall

nanoparticles, about 3 nm according to Scherrer-equation, which is consistent with the results shown in HRTEM images.

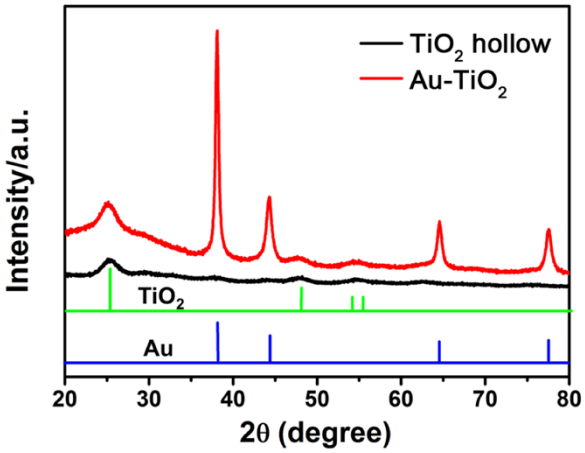

Figure 2 XRD patterns of TiO_2 hollow nanosphere and Au-TiO_2 yolk-shell nanosphere.

Surface plasmon resonance (SPR) is the most remarkable character of Au nanoparticles. Figure 3 shows the typical extinction spectra of original citrate-AuNS and the products achieved during each step are presented. The peak position of AuNS is red-shifted from 530 to 547 nm after coating SiO_2. This red shift is caused by the higher refractive index of SiO_2 (1.43) than that of water (1.33).[11] While if further coating TiO_2 and SiO_2, peak position showed no shift due to the thickness of first layer of SiO_2.[12] After removal of two layers of SiO_2, the peak position was slightly blue-shifted to 541 nm. The optical properties of TiO_2 3D-assembled array were investigated by diffuse reflectance UV-vis spectroscopy (Figure 3B). The reflection spectrum began to change sharply as the wavelength becomes shorter than 380 nm caused by strong intrinsic absorption of light of the anatase TiO_2 semiconductor. The SPR peak position of AuNS, however, did not change after assembling, which was still centered at 541 nm.

The photocatalytic H_2 generation was examined with three samples: monodispersed pure TiO_2 hollow nanosphere, monodispersed Au-TiO_2 yolk-shell nanosphere and Au-TiO_2 3D-assembled array. Figure 3C shows the amount of H_2 generated under visible-light irradiation (λ>420 nm) for 3 h. Because of no light absorption in this wavelength range, no H_2 was detected during the illumination when pure TiO_2 was served as photocatalyst. While after introducing AuNS, the samples exhibited photocatalytic

ability under visible light. Compared with monodispersed sample, 3D-assembled array displayed almost 3.5 times higher performance. This excellent visible-light photocatalytic activity can be attributed to the novel structure. When these three samples were irradiated under simulated solar light, the H_2 production activity follows the same order as in the case of visible light irradiation (Figure 3D). 3D-assembled array showed about 1.4 times higher performance than the monodispered sample, and both of these two samples exhibited 3~4 times higher performance than pure TiO_2 hollow nanosphere. We believe the AuNS encapsulating inside of TiO_2 shell plays an important role in enhancing photocatalytic performance.

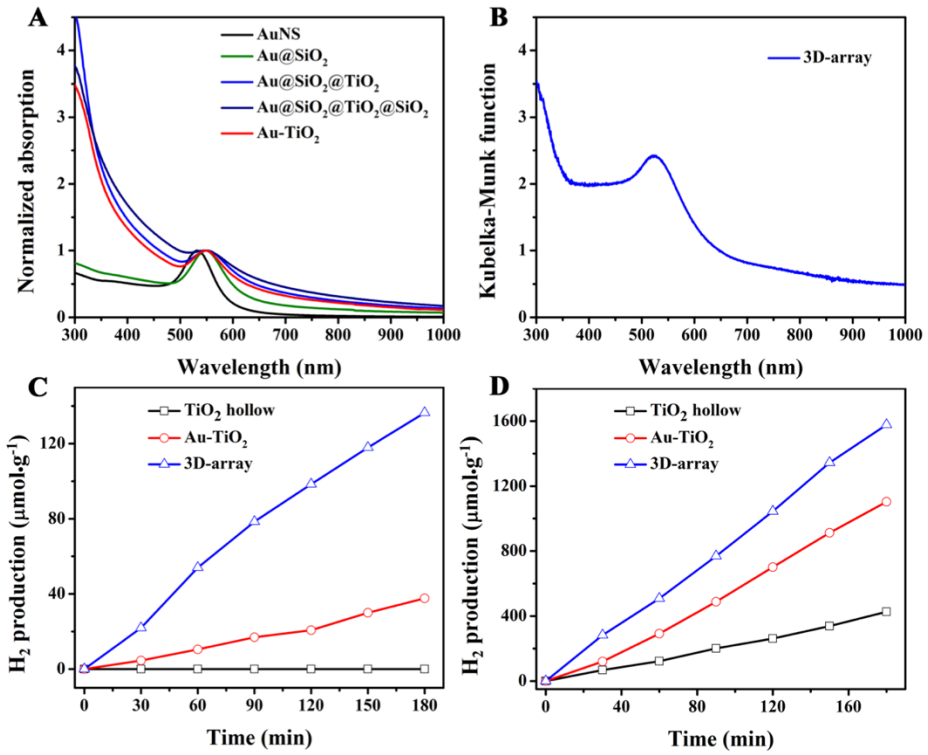

Figure 3 (A) UV-Vis absorption spectra of the samples during the synthesis. (B) UV-Vis absorption spectrum of 3D-order assembled Au-TiO_2 nanospheres. (C and D) Comparison of the photocatalytic production of H_2 from aqueous methanol mixture obtained for TiO_2 hollow nanosphere, Au-TiO_2 yolk-shell nanosphere and 3D-order assembled array under (C) visible light irradiation and (D) simulated daylight.

In addition, we also measured the stability of photocatalysts by repeating photocatalytic H_2 production experiments and assessment of the morphology after photocatalytic reaction (Figure 4). From Figure 4A we can see that there is no significant decay in the photocatalytic activity after three cycles and the SEM images

exhibited that the structure still kept three-dimensional array structure even though some yolk-shells were broken. These results suggest that the 3D-array has a good stability in photocatalytic H_2 production.

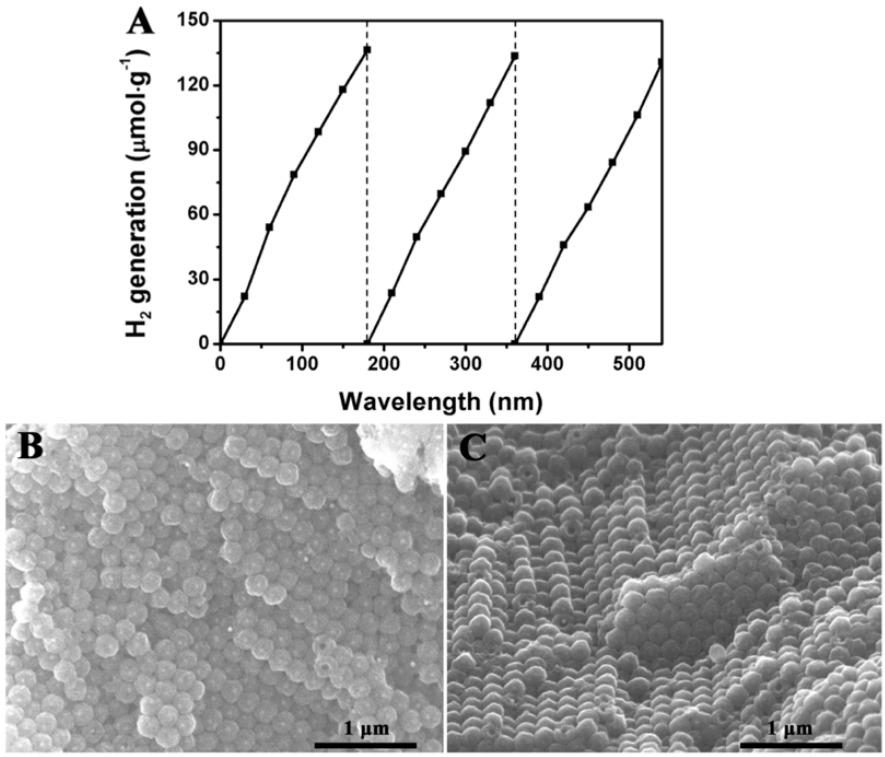

Figure 4 Recyclability of 3D-array as photocatalysts in H_2 production under visible light irradiation (A). SEM images of 3D-array after photocatalysis reaction (B-C).

It has been proposed that the photocatalytic activity of Au-TiO_2 under visible light irradiation relates to the hot electron transfer at the interface between AuNS and TiO_2.[13,14] To clarify the photocatalysis mechanism, single-particle photoluminescence (PL) spectroscopic measurement was carried out under 488 nm laser irradiation. Typical single-particle PL images of individual AuNS, Au-TiO_2 and Au-TiO_2 decorating Pt (Au-TiO_2-Pt) on cover glasses are shown in Figures 5A, B and C, respectively. Because there is no absorption under 488 nm for pure TiO_2, the observed PL emission comes from the recombination of electron-hole pairs in AuNS under laser irradiation. From the images, we can clearly find that the PL intensity gradually decays after forming Au-TiO_2 and Au-TiO_2-Pt. The corresponding detailed PL spectra of individual AuNS, Au-TiO_2 and Au-TiO_2-Pt were collected by switching the detection to a spectrometer equipped with an electron-multiplying charge-coupled device

(EMCCD) camera (Figure 5D). For AuNS, only one PL peak could be observed at 550 nm, while Au-TiO_2 showed PL shifted to the longer wavelength, indicating the interaction between plasmonic AuNS and TiO_2 shell. Such interaction was also consistently appeared in UV-vis absorption spectra in which the SPR peak shifted to longer wavelength for Au-TiO_2 compared with AuNS. The PL intensity of AuNS was quenched to 70 % by TiO_2 shell, suggesting that the hot electrons generated by AuNS partially transferred to the conduction band of TiO_2 shell. And the further quenching of PL intensity after decorating Pt nanoparticles exhibits that the injected electrons on the TiO_2 conduction band moved to Pt, which further retards the recombination of electrons and holes.

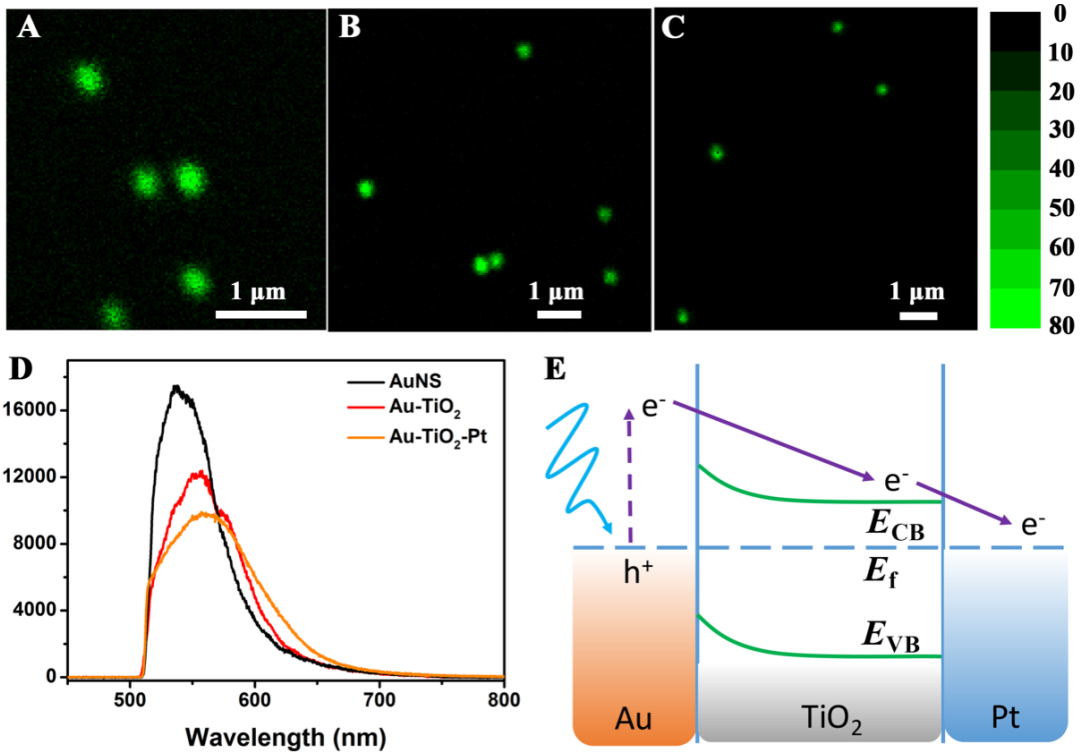

Figure 5 PL images of individual (a) Au nanosphere, (b) Au-TiO_2 yolk-shell nanosphere. (C) Correlated PL spectra of the corresponding Au and Au-TiO_2. (D) Schematic illustration of hot electron generated in Au and transfer to TiO_2.

We also randomly selected other six AuNS, six Au-TiO_2, and six Au-TiO_2-Pt from the cover glasses and measured their PL spectra under same conditions. It was confirmed that Au-TiO_2-Pt (Figure 6) showed undoubtedly the lower intensity compared with pure AuNS (Figure 7) and Au-TiO_2 (Figure 8) and the PL intensity of AuNS becomes weak after forming Au-TiO_2, which further support the fact that TiO_2

and Pt would retard the recombination of electron-hole pairs in AuNS. Additionally, it was confirmed that the PL intensities have small variations for each AuNS, Au-TiO_2 and Au-TiO_2-Pt, which is due to the monodispersed size and shape of nanoparticles.[15] Based on the single-particle PL images and spectra, charge migration route can be clear illustrated that the hot electrons are first generated in AuNS under 488-nm laser irradiation, then partially inject into the conduction band of TiO_2, and finally transfer to Pt nanoparticles. Because Pt is an excellent co-catalyst, H_2 evolution reaction would take place on the surface of it. (Figure 5E).

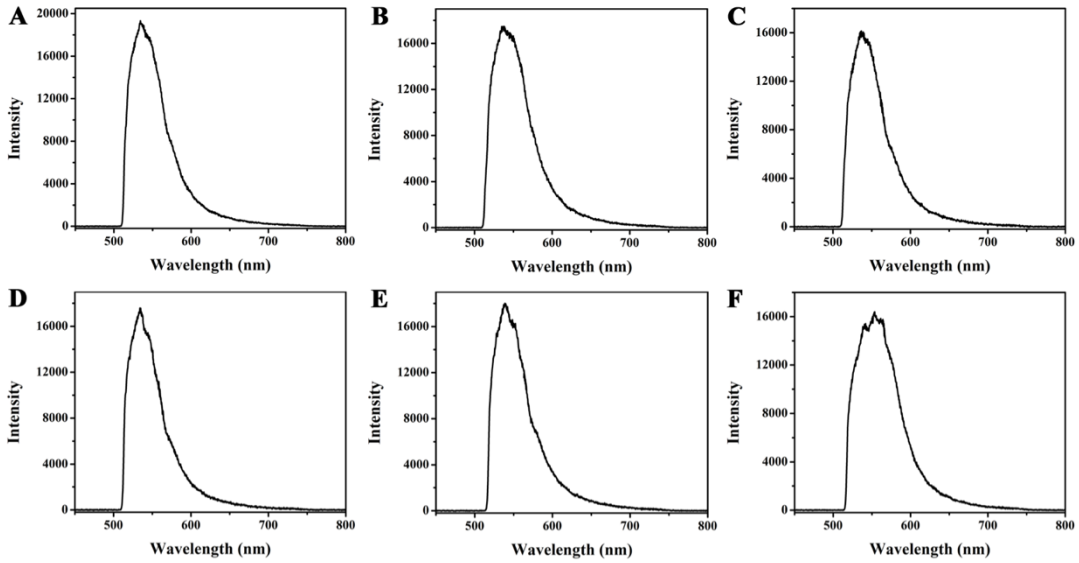

Figure 6 PL spectra (A-F) of six representative single naked Au nanospheres random selected from the cover glass.

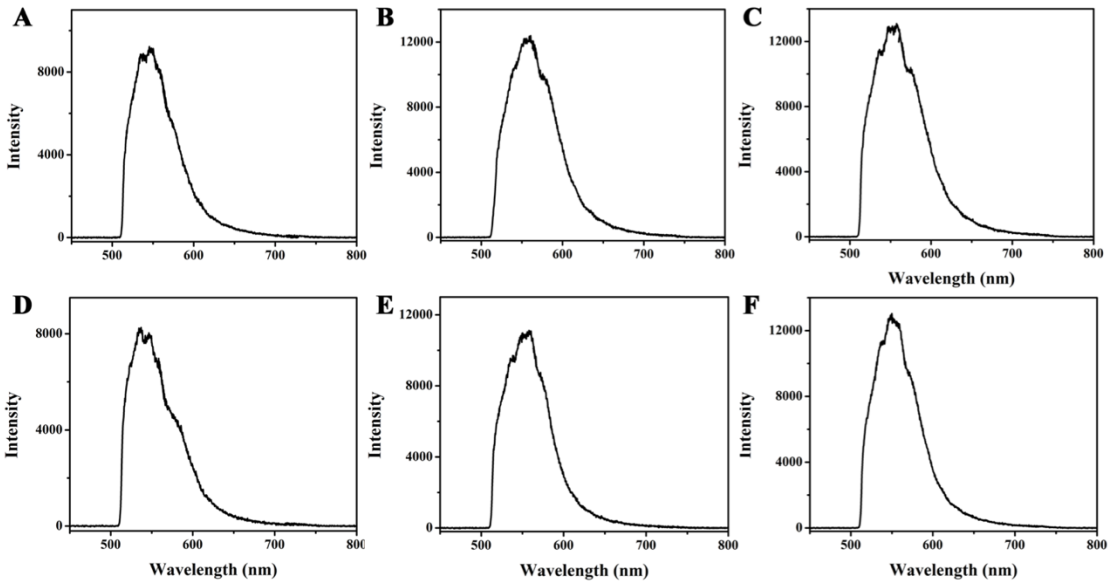

Figure 7 PL spectra (A-F) of six representative single Au-TiO_2 yolk-shell nanospheres random selected from the cover glass.

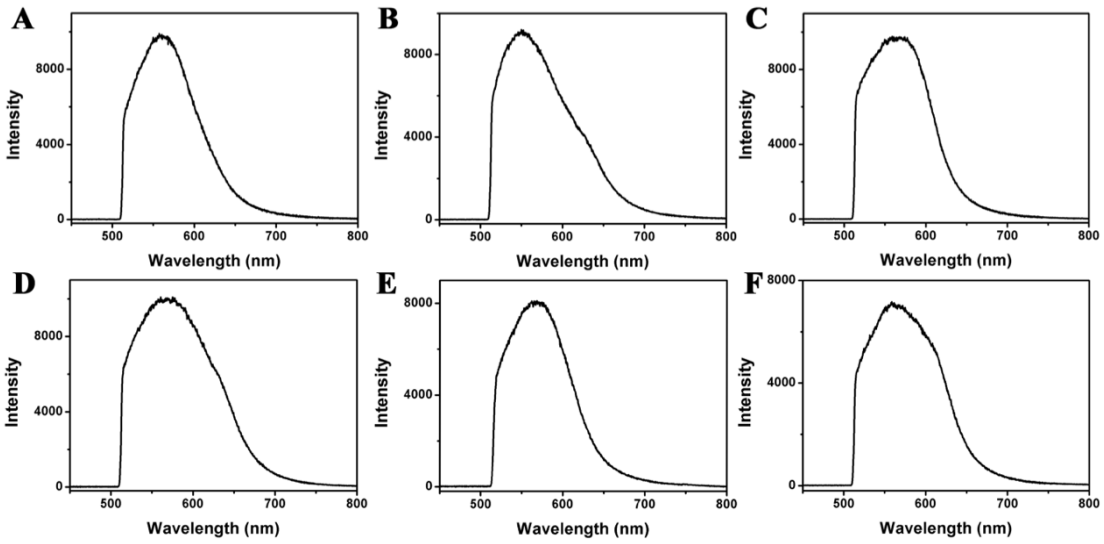

Figure 8 PL spectra (A-F) of six representative single Au-TiO_2-Pt yolk-shell nanospheres random selected from the cover glass.

Apart from the hot electrons generation, SPR-mediated local electromagnetic field of AuNS can increase the amount of electron-hole pairs in semiconductors to enhance the photocatalytic activity, because the photon absorption is proportional to the electric field squared ($|E|^2$).[16] Even though there is no spectral overlap between the amplified electric field and the absorption edge of TiO_2, it is known that there are defect states within the band gap of TiO_2.[17] The low density of these defect states inhibits the visible light absorption and thus prohibits the photocatalytic activity of TiO_2 under the visible light irradiation. However, introduction of AuNS leads to substantially improvement of electric field in the visible region and therefore increases the role of defect states in photocatalytic reactions.[18] To acquire the exact extent of electromagnetic field amplification and its possible contribution to the photocatalytic activity, FDTD simulations were carried out to analyze the electromagnetic field enhancement at the interfacial between AuNS and TiO_2 at the wavelength of SPR peak position (541 nm). According to the simulation results (Figure 9), the electromagnetic intensity of AuNS encapsulated in TiO_2 shell are enhanced greatly in the visible region assigned to their SPR absorption peak. The electromagnetic fields of 3D-array, however, display almost the same or even less intensity compared with Au-TiO_2, indicating that the assembling does not have extraordinary influence on electric-field intensity. Therefore, we can conclude that the SPR enhanced defect states are not responsible for increasing the

photocatalytic activity of H_2 generation using 3D-array.

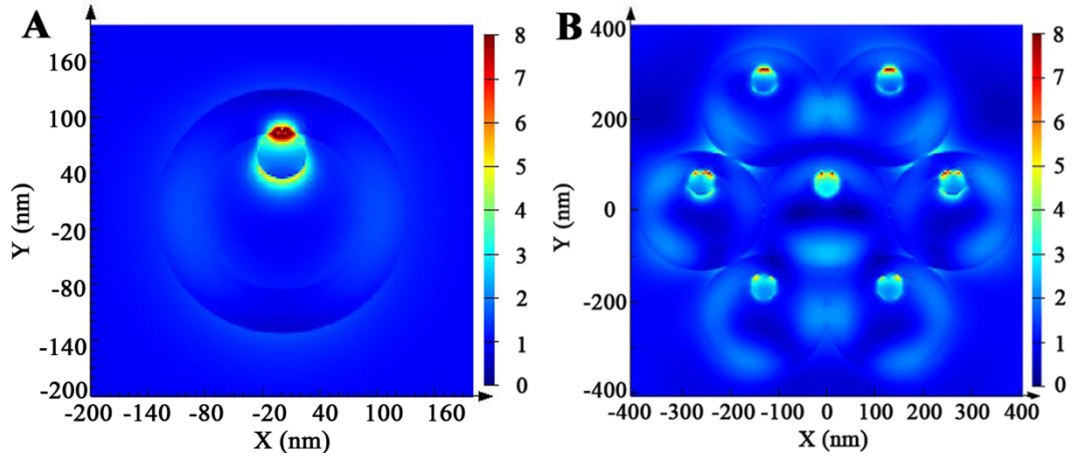

Figure 9 Electromagnetic field of monomer Au-TiO_2 yolk-shell nanosphere (A) and 3D-order assembled Au-TiO_2 yolk-shell nanosphere (B). The color scale bar shows the relative increase in field enhancement $|E|/|E_0|$.

3D-array just comes from the orderly assemble of single Au-TiO_2 yolk-shell and the amount of photocatalysts used for H_2 generation is also the same. For Au-TiO_2 yolk-shell and 3D-array photocatalysts, they can both disperse in the water homogeneously without any changing of their structure during the photocatalytic reaction. In this case, the exposure area of the photocatalysts is almost the same during whole reaction. Based on above discussions, we suppose that the improvement of photocatalytic activity of 3D-array under visible light irradiation is ascribed to its uniform 3D structure, which results in enhanced multi-scattering effect in-between Au-TiO_2. Au-TiO_2 as the photocatalyst for H_2 generation with the concentration of 1.15×10^{11} nanospheres mL^{-1} gives an average interparticle spacing of 2.3 μm. Because the intensity of scattered light in the zone of Au-TiO_2 is reciprocal to the distance from nanosphere to the point being investigated,[18,19] thus, the multi-scattering effect from other particles is much weaker in Au-TiO_2 compared with 3D-array due to the long interparticle distance. Previous research exhibited that the light absorption can be increased by decreasing the interparticle distance.[20] The nearly close packed Au-TiO_2 gives rise to enhanced multi-scattering and then these scattered light can transfer to the neighboring Au-TiO_2, which causes longer optical paths length of incident light in 3D-array. Therefore, the scattering light greatly increases the chance of AuNS to absorb light. It is believed that the shells do not only scatter the incident light of different wavelengths in the visible region, but

also multi-reflect the incident light.[21] In this case, the multi-reflection inside the nanoparticles could also increase the light path length due to the unique yolk-shell structure. In the photocatalytic H_2 generation under visible light irradiation, if more photons are absorbed by photocatalyst, more electrons are generated and used for H_2 generation leading to a higher efficiency (Scheme 2A). Since 3D-array exhibits an enhanced multi-scattering effect, more photons are scattered and reflected by TiO_2 shell and then absorbed by AuNS. Thus, the light utilization efficiency of 3D-array is greatly enhanced. To further confirm that the 3D-array structure has a higher light utilization efficiency, we measured the apparent quantum efficiency (AQE) of Au-TiO_2 and 3D-array under 540-nm irradiation. For 3D-array, the AQE was determined to be 0.43%, almost three-folds of that of Au-TiO_2 (0.16%), indicating that the 540-nm photons can be absorbed and utilized more efficiently by 3D-array. When comparing with previous reported Au/TiO_2 photocatalyst for H_2 evolution under the same conditions, a higher photocatalytic activity was found for our 3D-array than the reported Au/TiO_2 photocatalysts.[22,23]

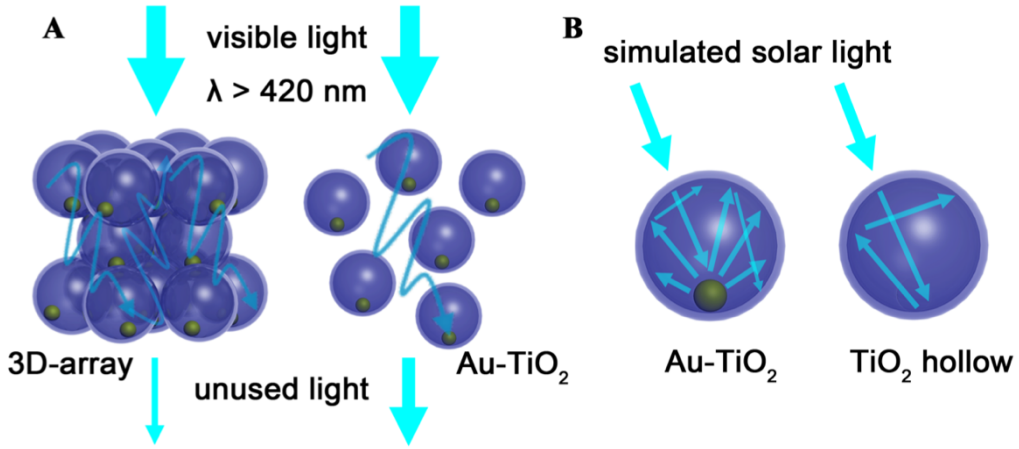

Scheme 2 Schematic diagram of the mechanism for enhanced photocatalytic ability.

Compared with the amount of conduction band electrons through the injection of hot electrons generated by AuNS under visible light irradiation, conduction band electrons generated by band gap excitation of TiO_2 under UV light irradiation are much larger. Therefore, when these photocatalysts were irradiated under simulated solar light, H_2 evolution is dramatically enhanced. The amount of H_2 generated by 3D-array was 1.4 folds higher than that of Au-TiO_2, resulting from the 3D-array structure with the multi-

scattering of incident light. This increasing light scattering in 3D-array is due to the nanoporous structure, which consists of ordered voids both inside and outside TiO_2 shell.[24] Compared with TiO_2 hollow, Au-TiO_2 exhibited significantly promoted photocatalytic activity (3~4 folds higher). We suppose this is due to two main factors. The first is the multi-scattering effect of AuNS. It has been reported that the radiation effects of Au nanoparticles become more and more important with the increasing of particle size.[25] In our system, the diameter of AuNS is about 51 nm, and the resonance photon scattering has a significant influence,[25,26] leading to an increase of the light path (Scheme 2B). Secondly, enhanced local electromagnetic field from SPR effect of AuNS increases in TiO_2 hollow, leading to the photocatalytic activity of Au-TiO_2. Plasmonic metal nanostructures enable light to be concentrated into nanoscale 'hotspots', enhancing its electric field. Since the photo absorption rate is proportional to the electric field squared ($|E|^2$),[16] such promoted SPR can assist in generating more electron-hole pairs in the TiO_2 shell, which is responsible for the enhancement of photocatalytic activity.[16]

4. Conclusion

In conclusion, uniform Au-TiO_2 and 3D-assembled Au-TiO_2 nanosphere array were fabricated, and the introducing of AuNS extended the light absorption from ultraviolet to visible light range. The results of H_2 generation experiment show that the 3D-assembled array has a higher photocatalytic activity, which is attributed to the increased light path caused by unique structure with enhanced multi-scattering effect. Since the generation of multi-scattering greatly depends on the shape of particles and distance between particles, it can be optionally employed as an efficient method to fabricate structures to enhance the light absorption. The findings made here would help us further understanding the relationship between multi-scattering and the photocatalytic performance and rationally design semiconductor photocatalysts with different morphology.

5. References

(1) Tong, H.; Ouyang, S. X.; Bi, Y. P.; Umezawa, N.; Oshikiri, M.; Ye, J. H. *Adv. Mater.* **2012**, 24, 229.

(2) Xie, J. F.; Zhang, J. J.; Li, S.; Grote, F.; Zhang, X. D.; Zhang, H.; Wang, R. X.; Lei, Y.; Pan, B. C.; Xie, Y. *J. Am. Chem. Soc.* **2013**, 135, 17881.

(3) Lukowski, M. A.; Daniel, A. S.; Meng, F.; Forticaux, A.; Li, L. S.; Jin, S. *J. Am. Chem. Soc.* **2013**, 135, 10274.

(4) Liu, S. W.; Yu, J. G.; Jaroniec, M. *J. Am. Chem. Soc.* **2010**, 132, 11914.

(5) Fujishima, A.; Honda, K. *Nature* **1972**, 238, 37.

(6) Zhang, J. M.; Jin, X.; Morales-Guzman, P. I.; Yu, X.; Liu, H.; Zhang, H.; Razzari, L.; Claverie, J. P. *ACS Nano* **2016**, 10, 4496.

(7) Xu, H.; Chen, X. Q.; Ouyang, S. X.; Kako, T.; Ye, J. H. *J. Phys. Chem. C* **2012**, 116, 3833.

(8) Yang, Q.; Li, M. Z.; Liu, J.; Shen, W. Z.; Ye, C. Q.; Shi, X. D.; Jiang, L.; Song, Y. L. *J. Mater. Chem. A* **2013**, 1, 541-547.

(9) Wang, C. L.; Liao, J. Y.; Zhao, Y. B.; Manthiram, A. *Chem. Commun.* **2015**, 51, 2848.

(10) Dadgostar, S.; Tajabadi, F.; Taghavinia, N. *ACS Appl. Mater. Interfaces* **2012**, 4 (6), 2964.

(11) Zhang, L.; Blom, D. A.; Wang, H. *Chem. Mater.* **2011**, 23, 4587.

(12) Tian, L. M.; Chen, E. Z.; Gandra, N.; Abbas, A.; Singamaneni, S. *Langmuir* **2012**, 28, 17435.

(13) DuChene, J. S.; Sweeny, B. C.; Johnston-Peck, A. C.; Su, D.; Stach, E. A.; Wei, W. D. *Angew. Chem. Int. Ed.* **2014**, 53, 7887.

(14) Mahmoud, M. A.; Qian, W.; El-Sayed, M. A. *Nano Lett.* **2011**, 11, 3285-3289.

(15) Zheng, Z. K.; Tachikawa, T.; Majima, T. *Chem. Commun*. **2015**, 51, 14373.

(16) Hou, W. B.; Cromin, S. B. *Adv. Funct. Mater.* **2013**, 23, 1612.

(17) Pu, Y.; Wang, G.; Chang, K.; Ling, Y.; Lin, Y.; Fitzmorris, B.; Liu, C.; Lu, X.; Tong, Y.; Zhang, J.; Hsu, Y.; Li, Y. *Nano Lett.* **2013**, 13, 3817.

(18) Joshi, P.; Zhang, L.; Davoux, D.; Zhu, Z.; Galipeau, D.; Fong, H.; Qiao, Q. *Energy Environ. Sci.* **2011**, 3, 1507.

(19) Van, H. *John Wiley & Sons*, New York, **1957**, 85.

(20) Xuan, Y.; Duan, H.; Li, Q. *RSC Adv.* **2014**, 4, 16206.

(21) Qian, J.; Liu, P.; Xiao, Y.; Jiang, Y.; Cao, Y.; Ai, X.; Yang, H. *Adv. Mater.* **2009**, 21, 3663.

(22) Tanaka, A.; Sakaguchi, S.; Hashimoto, K.; Kominami, H. *ACS Catal.* **2013**, 3, 79.

(23) Zhang, Z. Y.; Li, A. L.; Cao, S. W.; Bosman, M.; Li, S. Z.; Xue, C. *Nanoscale*,

2014, 6, 5217.
(24) Chen, J. I. L.; Freymann, G.; Choi, S. Y.; Kitaev, V.; Ozin, G. A. *Adv. Mater*. **2006**, 18, 1915.
(25) Noguez, C. *J. Phys. Chem. C* **2007**, 111, 3806.
(26) Tu, W.; Zhou, Y.; Li, H.; Li, P.; Zou, Z. *Nanoscale* **2015**, 7, 14232.

Chapter 2. In Situ Synthesis of Hollow-N-TiO_2/g-C_3N_4 Heterostructure: Noble-Metal-Free Visible-Light-Driven Photocatalysis Induced by Efficient Charge Separation

1. Introduction

H_2 evolution from water by utilizing solar energy has been a hot research topic because of its promising potential to overcome global energy crisis and environmental pollution since the discovery of photocatalytic water splitting on an electrode by Fujishima and Honda in 1972.[1]Titanium dioxide (TiO_2) with low cost, non-toxicity and long-term stability has been widely studied for photocatalysis and energy storage.[2,3] However, broader application of pure TiO_2 is still limited due to its relative wide band gap (3.2 eV) and fast recombination of photogenerated electrons and holes.[4-6] Therefore, designing and preparing novel TiO_2-based photocatalysts with visible light activity and improving the separation efficiency of photogenerated electron-hole pairs turn into a worldwide striving direction.[7-10]

Hosting TiO_2 with guest semiconductors to form heterostructures is the hottest research topic in the past decade and is continuing to be a pivotal one to improve the photocatalytic property of as-prepared photocatalysts.[11-13] Particularly, much attentions have been focused on a heterostructure (TiO_2/g-C_3N_4) of TiO_2 and graphitic carbon nitride (g-C_3N_4), because g-C_3N_4 is a graphite-like organic semiconductor, which has visible light absorption (bandgap 2.7 eV) and high reduction ability. In fact, g-C_3N_4 is considered to be a promising candidate for water splitting and environment purification under visible light irradiation,[14-16] due to its peculiar thermal stability, appropriate electronic structure and low cost for preparation. From the relation of energy state levels, TiO_2/g-C_3N_4 can form typical type Ⅱ heterostructure. Although TiO_2/g-C_3N_4 have been prepared by some groups and utilized for photocatalytic and electrodes,[17-19] electrons transfer kinetics and electron lifetimes from g-C_3N_4 to TiO_2 under visible light irradiation and the relation to photocatalytic activity are rarely studied.[20,21] Moreover, preparation of N-TiO_2/g-C_3N_4 heterostructures through *in situ* N doping from TiO_2 and

g-C_3N_4 to have effective surface contact has not been reported.

Transient absorption spectroscopy has been recently employed to investigate the dynamics of photogenerated holes and electrons in semiconductors,[22,23] and used here to explore the lifetime of electrons and electron transfer dynamics in N-TiO_2/g-C_3N_4. It has been reported that mesoporous anatase TiO_2 hollow nanosphere exhibits excellent photocatalytic performances under UV light irradiations due to their unique properties, such as low effective density, high specific surface area and good permeation.[24] Further functionalization of TiO_2 shells with g-C_3N_4 by taking advantage of TiO_2 mesopore structure would lead to effective contact between TiO_2 and g-C_3N_4 in the heterostructure and thus enhance its photocatalytic activity.

Herein, the authors report a facile approach to introduce g-C_3N_4 into mesoporous anatase TiO_2 hollow nanospheres through an impregnated calcination method. By simply changing the amount of g-C_3N_4 precursor, cyanamide (CY), the final products were varied from N-TiO_2 to N-TiO_2/g-C_3N_4. A variety of measurements were used to characterize *in situ* synthesized photocatalysts and a possible formation mechanism was proposed. As expected, N-TiO_2/g-C_3N_4 exhibited excellent photocatalytic activity in H_2 production under visible light irradiation without any noble metal co-catalyst. Based on the electrochemical spectroscopy and time-resolved diffuse reflectance spectroscopy, charge separation and electron injection dynamics from photoexcited g-C_3N_4 to N-TiO_2 in N-TiO_2/g-C_3N_4 is discussed and the effect of the amount of g-C_3N_4 on photocatalytic activity is clarified. This is a detail research on the lifetime of electrons and electron transfer dynamics for g-C_3N_4. We believe that our strategy provides a stepping stone for designing novel heterostructure photocatalysts and meanwhile gives deep insight analysis of charge transfer dynamics.

2. Experimental Section

Materials. Ammonium hydroxide (28-30%), tetraethylortosilicate (TEOS, 98%), tetrabutyl titanate (TBOT 99%), polyvinylpyrrolidone (PVP, $M_w \sim 40000$), 2-propanol (99%), cyanamide (CY), absolute ethanol and Milli-Q water were used.

Preparation of TiO_2 hollow nanospheres. As a typical in-situ synthesis, TEOS (4.5 mL) was mixed with deionized water (24.75 mL), ethanol (61.75 mL) and an aqueous solution of ammonia (1.5 mL). After stirring for 4 h, the silica particles (SiO_2 nanospheres) were separated by centrifugation, washed two times with ethanol.

SiO_2 nanospheres were dispersed in a mixture of ethanol (25 mL) and acetonitrile (7 mL) under stirring. After adding ammonia aqueous solution (200 μL), TBOT (300 μL) in a mixture of ethanol (3 mL) and acetonitrile (1 mL) was injected into the mixture quickly. After stirring for 3 h, the mixture was centrifuged and washed with water. Above SiO_2@TiO_2 particles were dispersed into water containing 20 mg PVP overnight to allow for the adsorption of PVP onto TiO_2 surface, then separated from solution by centrifugation, and re-dispersed in 10 mL ethanol. The solution of SiO_2@TiO_2 was sequentially mixed with ethanol (13 mL), water (4.3 mL), TEOS (300 μL) and aqueous ammonia (620 μL). After stirring for 4 h, the resulting particles were centrifuged, washed with water and dried under 80 ºC in an oven.

The multi-layered particles were calcined in air at 800 ºC for 2 h to remove all organic compounds and crystallize the amorphous TiO_2. Then the calcined samples were treated by 10 mL 0.6 M NaOH solution at 70 ºC for 2 h. After etching, TiO_2 hollow nanospheres were centrifuged several times using water and ethanol, and then dispersed into ethanol.

Preparation of N-TiO_2/g-C_3N_4 (N-TCN-x, x= 200, 500, 700, and 1000). TiO_2 hollow nanospheres solution (10mg in 600 μL ethanol) was mixed with different amounts of ethanol solution containing CY (1 g mL^{-1}). When the amounts of CY solution were 200, 500, 700 and 1000 μL, as-prepared mixtures were obtained to be dried under stirring in 55 °C water bath. After drying, these samples were heated to 550 °C for 2 h in a glass bottle with a ramp rate of 3 °C min^{-1}, and N-TiO_2/g-C_3N_4 (N-TCN-x, x= 200, 500, 700, and 1000) were obtained. For the in-situ synthesis of pure g-C_3N_4, 1 g of CY was put in a glass bottle and heated to 550 °C with a ramp rate of 3 °C/min.

Photocatalytic H_2 evolution. 3 mg sample were dispersed in 5 mL aqueous solution containing 20 vol% methanol for H_2 evolution. Prior to the irradiation, the suspension of the catalyst was dispersed by using an ultrasonic bath, and then bubbled with argon through the reactor for 30 min to completely remove the dissolved oxygen and ensure

the reactor was in an anaerobic condition. The samples were irradiated at different wavelengths using a Xenon lamp for H_2 generation (Asahi Spectra, HAL-320; 350 mW cm^{-2}). The reaction temperature was kept at about 293 K. The visible light was filtered with nominal 420 nm cutoff filter, while a simulated daylight irradiation was conducted without any filter. The volume of H_2 was measured by using Shimadzu GC-8A gas chromatograph equipped with an MS-5A column and a thermal conductivity detector.

Photoelectrochemical measurements. Electrochemical and photoelectrochemical measurements were performed in a three-electrode quartz cells. A platinum wire was used as the counter electrode, and a Ag/AgCl electrode was used as the reference electrode. N-TiO_2/g-C_3N_4 (N-TCN-x, x= 200, 500, 700, and 1000) film on a glassy carbon electrode was served as the working electrode. 0.1 M Na_2SO_4 aqueous solution was used as the electrolyte. The Xenon lamp (350 mW cm^{-2}) was utilized as the light source in the photoelectrochemical measurements.

Time-resolved diffuse reflectance transient absorption measurements. The femtosecond diffuse reflectance transient absorption spectra were measured by the pump and probe method using a regeneratively amplified titanium sapphire laser (Spectra-Physics, Spitfire Pro F, 1 kHz) pumped by a Nd:YLF laser (Spectra-Physics, Empower 15). The seed pulse was generated by a titanium sapphire laser (Spectra-Physics, Mai Tai VFSJW; fwhm 80 fs). The fourth harmonic generation (420 nm) of the optical parametric amplifier (Spectra-Physics, OPA-800CF-1) was used as the excitation pulse. A white light continuum pulse, which was generated by focusing the residual of the fundamental light on a sapphire crystal after the computer controlled optical delay, was divided into two parts and used as the probe and the reference lights, of which the latter was used to compensate the laser fluctuation. Both probe and reference lights were directed to the sample powder coated on the glass substrate, and the reflected lights were detected by a linear InGaAs array detector equipped with the polychromator (Solar, MS3504). The pump pulse was chopped by the mechanical chopper synchronized to one-half of the laser repetition rate, resulting in a pair of spectra with and without the pump, from which the absorption change (%Abs) induced by the pump pulse was estimated. All measurements were carried out at room

temperature.

Characterization of materials. The samples were characterized using X-ray diffraction (XRD, Rigaku Rint-2500, CuKα source), SEM (JEOL JSM-6330FT), and HRTEM (JEOL JEM 3000F, operated at 300kV). The steady-state UV-visible absorption and diffuse reflectance spectra were measured by UV-visible-NIR spectrophotometers (Shimadzu, UV-3100, and Jasco, V-570, respectively) at room temperature. The XPS measurements were performed with the PHI X-tool 8ULVAC-PHI).

3. Results and Discussion

In order to confirm the existence of g-C_3N_4 in N-TiO_2/g-C_3N_4 (N-TCN-x, x= 200, 500, 700, and 1000) after calcination process, FT-IR spectra were measured (Figure 1). FT-IR spectrum of pure g-C_3N_4 exhibited the feature-distinctive stretch modes of aromatic CN heterocycles at 1200-1700 cm^{-1} together with the breathing mode of bending vibration of heptazine ring at 808 cm^{-1}, which was consistent with the reported studies.[25,26] For pure TiO_2, the broad absorption band around 1000 cm^{-1} was assigned to Ti-O stretching mode.[18] When the volume of CY ethanol solution was 200 μL (1 g mL^{-1}), no peak of g-C_3N_4 could be observed in FT-IR spectrum of N-TCN-200. If we increased the amount of CY (500 μL), characteristic peaks of N-TiO_2 and g-C_3N_4 were appeared for N-TCN-500, suggesting that both N-TiO_2 and g-C_3N_4 were involved. The broad absorption band around 1000 cm^{-1} disappeared when the amount of CY was increased to 700 and 1000 μL and only feature peaks of g-C_3N_4 were observed in N-TCN-700 and N-TCN-1000.

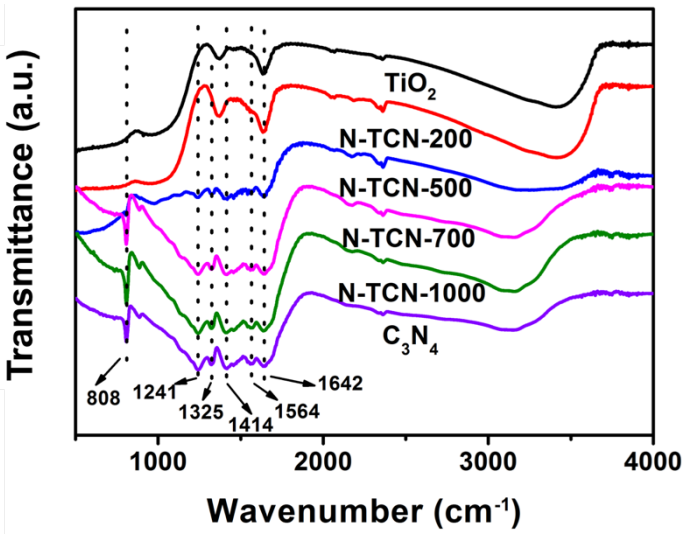

Figure 1 FT-IR spectra of TiO_2, N-TiO_2/g-C_3N_4 (N-TCN-x, x = 200, 500, 700, and 1000), and g-C_3N_4.

The morphology and microstructure of TiO_2 hollow spheres with and without g-C_3N_4 were characterized for comparison. Figure 2 displays the typical SEM and TEM images of pure TiO_2, N-TCN-200, and N-TCN-700. Pure TiO_2 sample is composed of a large number of hierarchical nanospheres with diameters about 100 nm. The hollow structure can be observed clearly from the cavity inside of the smooth shell according to TEM image (Figure 2D). HRTEM image of one single TiO_2 exhibits that the shell is composed of small TiO_2 grains with size about 3~5 nm. In addition, a large number of mesopores with a 3D interconnected framework built by nanosized TiO_2 building block particles is exhibited on the hollow spheres. After calcination with 200 μL CY ethanol solution under 550 °C for 2 h, the products still keep their hollow structure, while the morphology changes a lot, and no g-C_3N_4 is found in the products. Then we continue to increase the amount of CY to 500 and 700 μL, g-C_3N_4 starts to appear in N-TCN-x (x = 500 and 700) (Figure 3A and D, Figure 2C and F, respectively). This result is consistent with that of FT-IR measurement. It is clearly found that TiO_2 hollow structures and wrinkled two dimensional structures (g-C_3N_4) are coupled together tightly (Figure 2F) and part of mesopores are filled with g-C_3N_4 (inset image of Figure 3D). The formation of g-C_3N_4 both outside and inside of the shell indicates that the intimate interfacial contact between N-TiO_2 spheres and g-C_3N_4 nanosheets is readily obtained by such a simple impregnated calcination approach. While further adding TiO_2

sample to 1000 μL CY ethanol solution, large amount of g-C_3N_4 are generated outside of the shell and mainly fully cover TiO_2 spheres, as shown in Figure 3B and E. The structure of g-C_3N_4 in N-TCN-1000 resembles pure g-C_3N_4 (Figure 3C and F), which is composed of large amount of layers and shown as bulk.

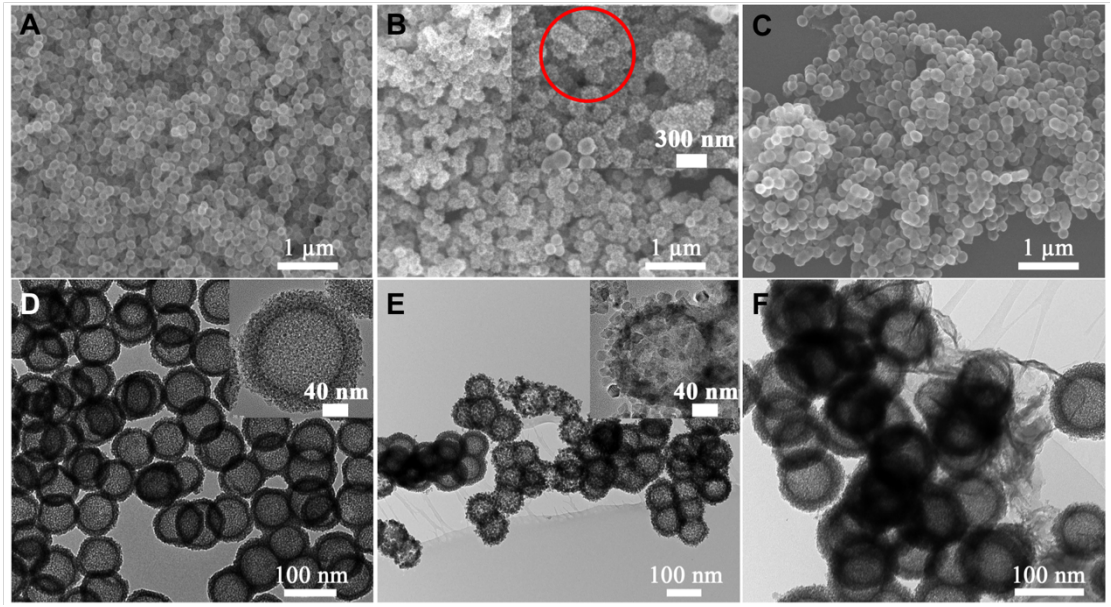

Figure 2 SEM and TEM images of pure TiO_2 hollow nanosphere (A and D), inset is HRTEM image; N-TCN-200 (B and E), insets are enlarged SEM and TEM images; N-TCN-700 (C and F).

In addition to the gradual formation of g-C_3N_4, morphology change of TiO_2 sphere is another interesting point. By comparing the morphologies before and after calcination with 200 μL CY solution, we observe that the shell surface of some hollow nanospheres turn to be rough, indicating that small TiO_2 grains change significantly (clearly shown in red circle in Figure 2B inset image). HRTEM image displays obviously that the size of TiO_2 particle changes from about 3 nm to 20 nm (Figure 2E inset image). For the N-TCN-500 sample, even though there are still some roughed TiO_2 spheres, the quantity decreases a lot, as shown in Figure 3A and D. The rough hollow spheres are totally disappeared in N-TCN-700 (Figure 2C and F). We suppose that this morphology changing in N-TCN-200 and N-TCN-500 is due to the re-growth of TiO_2 particles under high temperature (550 °C). In order to support this, pure TiO_2 hollow nanospheres are calcined under the same condition and nearly all the surface of spheres become rough (Figure 4). Therefore, we suspect that the formation of g-C_3N_4

during calcination process has a confinement effect on the re-growth of TiO_2 particles. If the amount of CY is small (200 μL), g-C_3N_4 could not be generated, thus TiO_2 particles re-grow into large size and the morphology become rough. While increasing the amount prohibits the re-growth of particles.

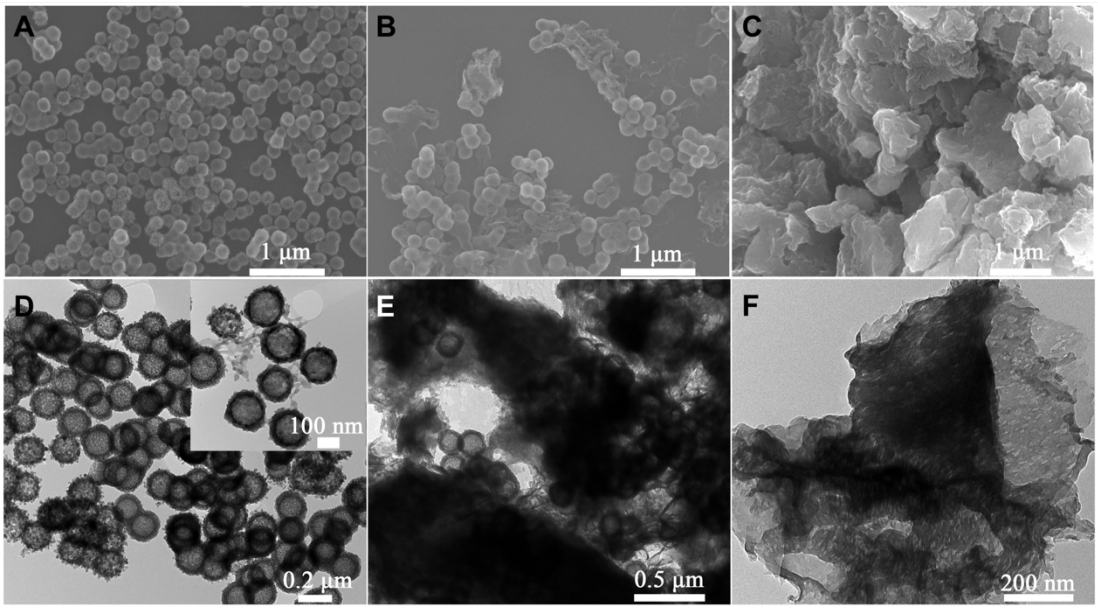

Figure 3 SEM and TEM images of N-TCN-500 (A and D), N-TCN-1000 (B and E) and pure C_3N_4 (C and F).

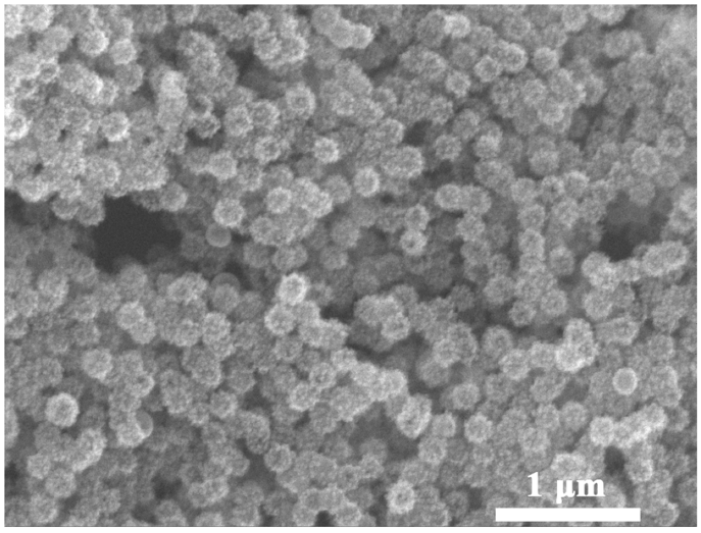

Figure 4 SEM image of TiO_2 after calcination under 550 ºC for 2h.

Crystallographic and quantitative analyses are conducted by XRD and TGA, respectively. The XRD pattern of pure TiO_2 in Figure 5A is assigned to be anatase TiO_2 (PDF 21-1272). According to Scherrer's equation, a particle size is calculated to be 3 nm, therefore, the widths of peaks are greatly broadened, and the intensity decreases

considerably. The distinct diffraction peak at 27.4° in g-C_3N_4, corresponding to the interlayer stacking of aromatic segments, is indexed to (002) peak for graphitic materials.[26] Similar to the results of FT-IR, SEM and TEM, no g-C_3N_4 is detectable for N-TCN-200. The width of peaks become narrow and intensity enhances, which also confirm the re-growth of TiO_2 particles into larger size. The diffraction peaks of g-C_3N_4 started to appear when the volume of CY ethanol solution increases to 500 μL. Due to further increasing of CY, only a very weak shoulder peak of TiO_2 at 25.2º is detected in N-TCN-700 and almost no TiO_2 peak is observed in N-TCN-1000. In the XRD spectra, no other characteristic peak is found, indicating the high purity of N-TCN-x. The actual weight ratio of g-C_3N_4 in N-TCN-x is measured by TGA (Figure 5B). Decomposition of g-C_3N_4 is completed at 600 °C, while TiO_2 remains stable above 600 °C. Thus, it is possible to determine the weight ratio of g-C_3N_4 in N-TCN-x by observing their residual mass after the temperature has risen to 600 °C. Following the methodology, a gradual change in weight percentage of g-C_3N_4 is observed, from 87.8% in N-TCN-1000 to 69.8% in N-TCN-700 and 42.9% in N-TCN-500. Again, no decomposition is observed for N-TCN-200, which is consistent with above discussion. The detailed data are summarized in Table 1.

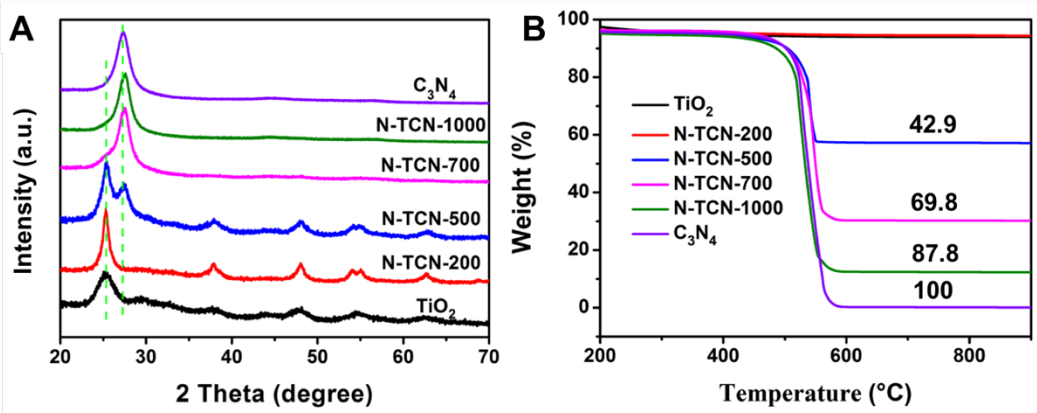

Figure 5 XRD patterns (A) and TGA traces (B) of TiO_2, N-TCN-x, and g-C_3N_4.

Table 1 TGA, BET surface area, BJH pore size and volume of various photocatalysts.

Photocatalysts	g-C_3N_4 (wt%) (TG)	Surface area (m^2 g^{-1})	Pore size (nm)	Pore volume (cm^3 g^{-1})
TiO_2	0	239	2.18	0.3910
N-TCN-200	0	66.5	2.08	0.2043
N-TCN-500	42.9	63.3	2.08	0.1227
N-TCN-700	69.8	39.9	2.08	0.0576
N-TCN-1000	87.8	19.2	1.75	0.0453
g-C_3N_4	100	4.32	1.34	0.0147

In order to analyze N-TCN-x and why there is no g-C_3N_4 in N-TCN-200, XPS measurement is performed. Figure 6 shows XPS spectra of Ti 2p, O 1s, C 1s and N 1s of N-TCN-200 and N-TCN-700. The C 1s high-resolution spectrum displays two peaks centering at 284.8, and 288.2 eV for N-TCN-700 (Figure 6A) to be assigned to sp^2 C-C bonds and sp^2-bonded carbon for N-containing aromatic rings (N-C=N), respectively.[27] While no C signal is detected for N-TCN-200. The N 1s spectrum of N-TCN-700 is deconvoluted into four different Gaussian-Lorentzian peaks centered at the binding energies of 398.3, 398.9, 400.4 and 404.5 eV (Figure 6B). The peaks of 398.3, 398.9 and 400.4 eV are assigned to sp^2-hybridized aromatic N atoms bonded to C atoms (C=N-C), tertiary nitrogen N-$(C)_3$ group linking structural motif (C_6N_7) and N atoms bonded to three C atoms in the aromatic cycles, respectively.[28] The peak centered at 404.5 eV is also observed by other group,[29] although the assignment is not fully understood. On the contrary, only one weak peak located at 400 eV is observed for N-TCN-200, to be assigned to N atoms doped in TiO_2.[26] The shift of Ti 2p peaks in N-TCN-700 is observed probably ascribing to increasing amount of N doping (Figure 6C). In additional, elemental mapping of N-TCN-200 further supports that N element is distributed over TiO_2 hollow nanosphere homogeneously with other elements, Ti and O, which is another strong evidence for N doping (Figure 7). The peaks observed at 529.9 eV is assigned to the contribution of Ti-O in TiO_2, while another peak is to the hydroxyl group of chemisorbed water (Figure 6D).[30,31]

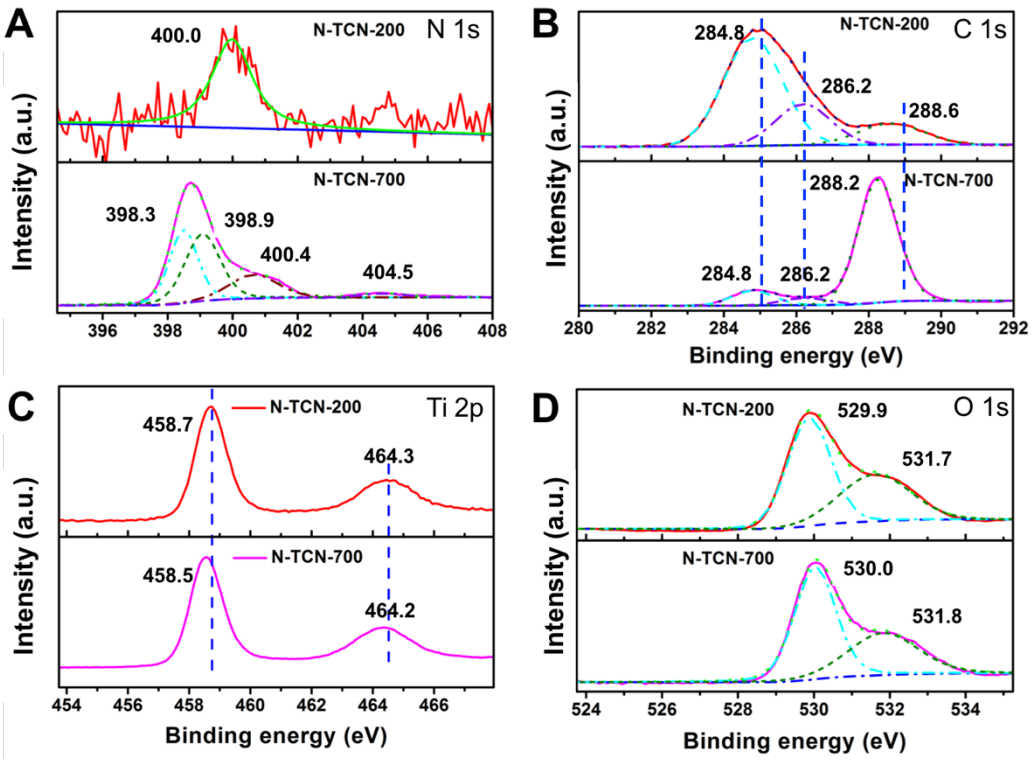

Figure 6 XPS spectra of C 1s (A), N 1s (B), Ti 2p (C) and O 1s (D) of N-TCN-200 and N-TCN-700.

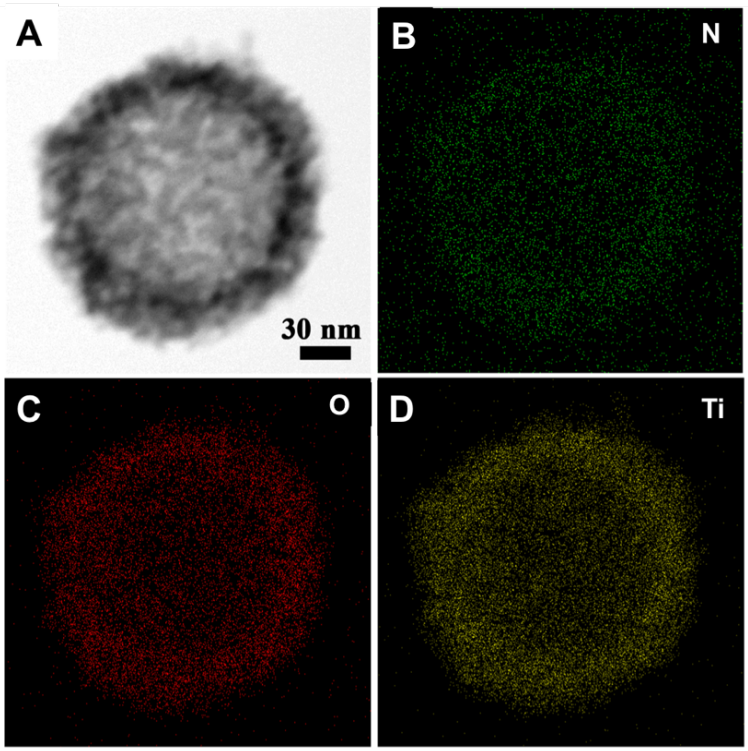

Figure 7 TEM image (A) and elemental mappings of N (B), O (C), and Ti (D) of N-TCN-200.

The data obtained after deconvolution of these peaks reveal that the atomic ratios of

C/N and O/Ti are approximately 0.66:1 and 2:1, respectively (Table 2). The C/N ratios for N-TCN-500 (-700 and -1000) and g-C_3N_4 are lower than 0.75 for the ideal crystal g-C_3N_4. These results are in agreement with the FT-IR and XPS analyses, implying that the amino groups originated from the incomplete condensation of the as-prepared g-C_3N_4.[32]

Table 2 Values of C/N and O/Ti ratios in the all photocatalysts.

Sample	**TiO_2**	**N-TCN-200**	**N-TCN-500**	**N-TCN-700**	**N-TCN-1000**	**g-C_3N_4**
C/N ratio	-	-	0.69	0.67	0.66	0.66
O/Ti ratio	1.91	2.19	2.12	1.91	2.29	-

According to the results and discussions, we suggest a possible formation mechanism for N-TCN-x (Scheme 1). Due to the good permeation property, CY ethanol solution easily penetrates into the cavity of TiO_2 hollow nanosphere through the mesopores. After evaporation of ethanol under 60 ºC in a water bath, a portion of melted CY still leaves in the voids. Then during the calcination process, a part of CY decomposes and acts as N precursor for the N doping into TiO_2 shell, while the rest polymerize to generate g-C_3N_4. When the amount of CY is not large enough, all CY decompose to form N doping TiO_2 shell as N-TCN-200. While if the amount of CY is enough, both N doping and g-C_3N_4 formation take place simultaneously and g-C_3N_4 is gradually formed from inner void to the outside of TiO_2 hollow spheres, such as N-TCN-500, N-TCN-700 and N-TCN-1000. On the other hand, due to the formation of g-C_3N_4 outside of TiO_2 small grains (3 nm), the recrystallization of these small grains to large particles (20 nm) is greatly restrained. This is the first time that we control gradual change from N doping TiO_2 hollow nanosphere to N-TCN-x, by just varying the amount of CY.

Scheme 1. Illustration of formation mechanism for N-TCN-x.

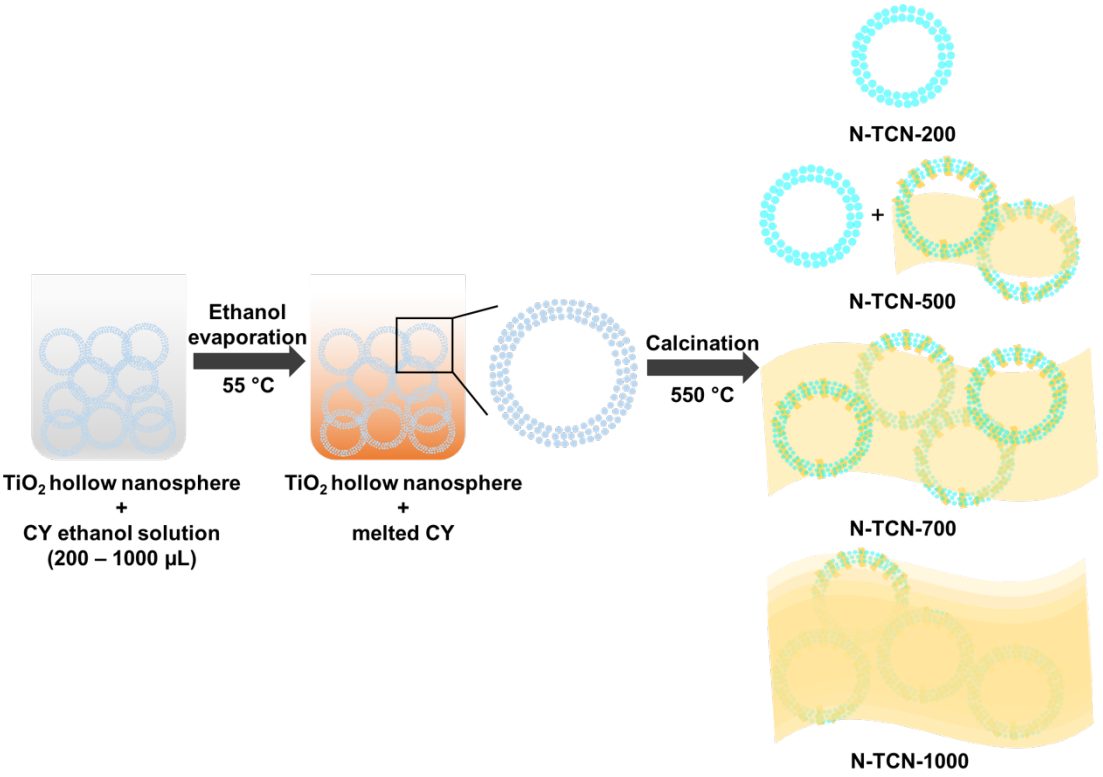

The textural property of N-TCN-x was characterized by nitrogen gas porosimetry measurement as shown in Figure 8. The isotherms are of typical type IV pattern with distinct H_3 hysteresis loops in the range of 0.4-1.0 P/P_0, indicating the presence of slit-like pores according to the IUPAC classification. Surface areas of N-TCN-x measured by multi-point Brunauer-Emmett-Teller (BET) method from the adsorption branch are all lower than that of TiO_2 hollow spheres. Their corresponding pore size distribution profiles as determined using the Barrett-Joyner-Halenda (BJH) method from the desorption branch of isotherms are shown in the inset in Figure 8, which indicate the mesoporous nature of synthesized TiO_2 hollow spheres and N-TCN-x. The BET surface area, BJH pore size and volume are summarized in Table 1. The sharp decrease of BET comparing pure TiO_2 with N-TCN-200 is related to the re-growth of TiO_2 particle to large size. The further decrease of BET is resulted from the formation of g-C_3N_4 in the void of TiO_2 hollow sphere.

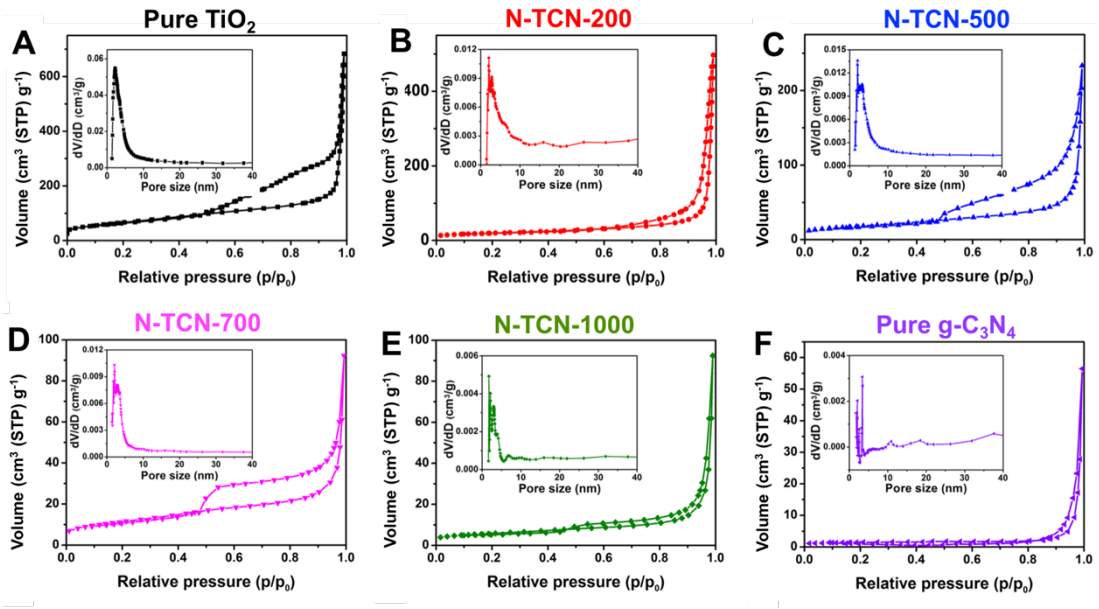

Figure 8 N_2 adsorption-desorption isotherms and pore size distribution curves (inset) of TiO_2, N-TCN-x, and g-C_3N_4. (A) Pure TiO_2, (B) N-TCN-200, (C) N-TCN-500, (D) N-TCN-700, (E) N-TCN-1000 and (F) pure g-C_3N_4.

Optical absorption and energy band features of the photocatalysts are important in determining their photocatalytic efficiency. Light absorption properties were characterized by UV-vis diffuse reflectance spectroscopy (DRS). Figure 9A depicts the DRS spectra of pure TiO_2, g-C_3N_4 and N-TCN-x. TiO_2 absorbs only ultraviolet light with a wavelength shorter than 400 nm, while g-C_3N_4 absorbs light with a wavelength up to 500 nm. However, a little absorption of pure TiO_2 is observed even above 800 nm, which attributes to multi-scattering effect due to the mesoporous structure of TiO_2 hollow. After hybridization of TiO_2 with g-C_3N_4, the absorption edge of TiO_2/g-C_3N_4 is found to shift towards visible region, and the absorption in the visible light region (400-650 nm) increases gradually with increasing the amount of CY. This absorption shift is attributed to the strong interactions between N-TiO_2 and g-C_3N_4,[11] as a result of interdispersion of two semiconductors and g-C_3N_4 serves as a visible light sensitizer to drive a reaction on the surface of TiO_2 hollow spheres. It is suggested that the extension of absorption to visible region enhances the formation of electron-hole pairs in photocatalysts and improves their photocatalytic performance.[34,35] Interestingly, N-TCN-200 is also able to absorb visible light up to 460 nm due to the doping level generated by N atom. Inset digital image of N-TCN-x clearly exhibits the gradual color

change from white to yellow.

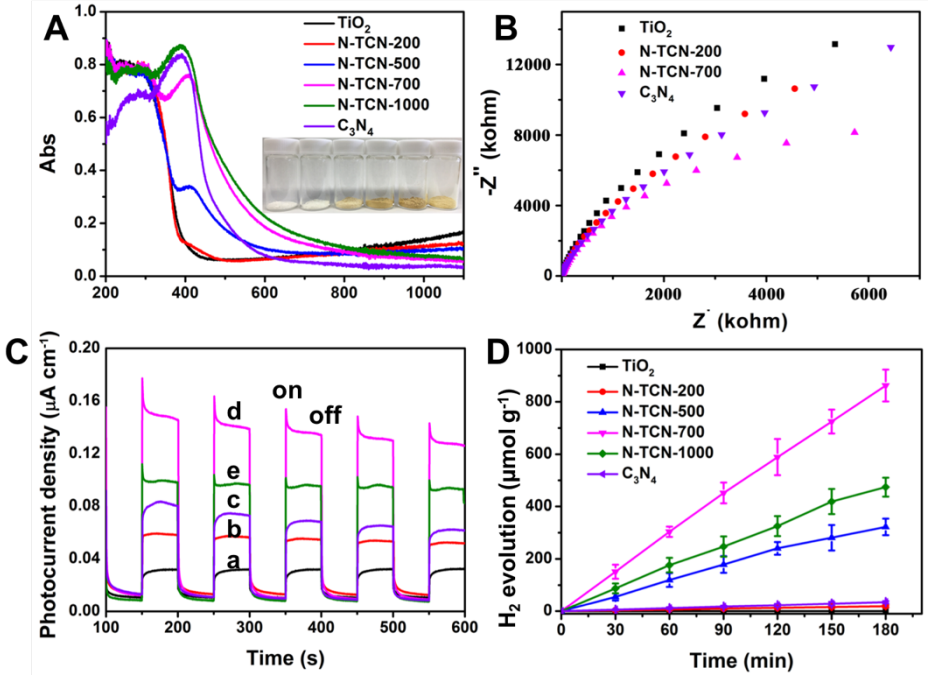

Figure 9 Diffuse-reflectance spectroscopy of TiO_2, N-TCN-x, and g-C_3N_4, inset is the digital image showing gradual change in color due to the absorption change (A). Electrochemical impedance spectroscopy (EIS) Nyquist plots under visible light irradiation (B) and transient photocurrent density curves (C) for TiO_2 (a), N-TCN-200 (b), g-C_3N_4 (c), N-TCN-700 (d) and N-TCN-1000 (e) in 0.5 M Na_2SO_4 solution. H_2 evolution from water splitting using various photocatalysts under visible light irradiation (D).

In order to clarify the fast interfacial charge transfer between g-C_3N_4 and N-TiO_2, electrochemical impedance spectroscopy (EIS) and transient photocurrent (*I-t*) responses of N-TCN-x photocatalyst film electrodes were recorded. Figure 9B exhibits EIS curves of TiO_2, N-TCN-200, N-TCN-700 and g-C_3N_4 film electrodes. Smaller frequency semicircle of the arc in an EIS Nyquist plot indicates smaller resistance at the interface and smaller charge transfer resistance on the electrode surface.[36] The results present the sequence of the frequency semicircles is: TiO_2 > N-TCN-200 > g-C_3N_4 > N-TCN-700, which suggests the fastest separation rate of charge carrier pairs over N-TCN-700 photoanode. For the transient photocurrent measurement, the higher photocurrent intensity often corresponds to better photocatalytic activity. The *I-t* curves shown in Figure 9C exhibit similar order for EIS. As we know, the photocurrent is formed mainly by the diffusion of photogenerated electrons to the back contact and

meanwhile the photogenerated holes are taken by hole acceptor in the electrolyte.[37] In this case, the enhanced photocurrent responses of N-TCN-700 reveal better charge separation and efficient electron transfer within N-TCN-x compared with those of N-TCN-200 and g-C_3N_4.

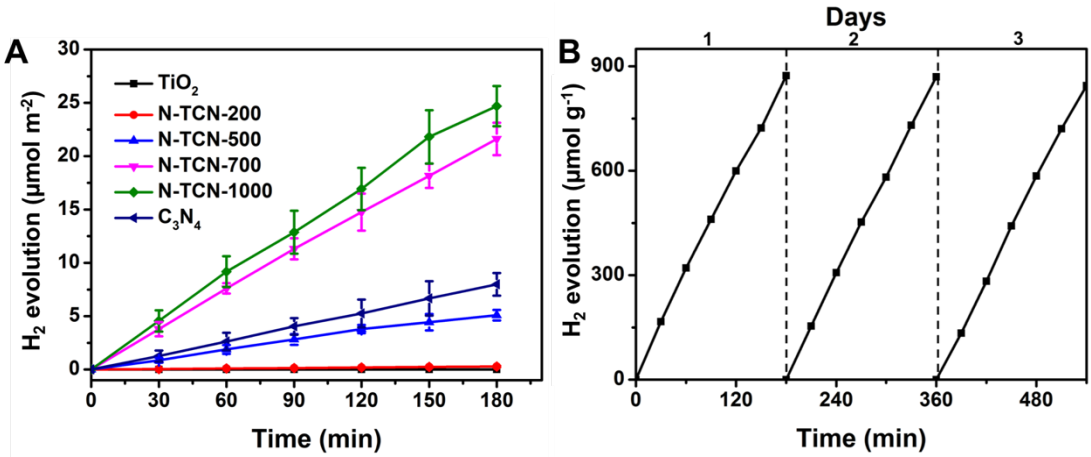

Figure 10 Plots of H_2 evolution volume normalized by the surface areas of various photocatalysts vs. irradiation time (A). Stability test of N-TCN-700 photocatalyst (B).

H_2 evolution experiment is carried out to investigate the accurate photocatalytic activity of the samples under visible light irradiation (≥420 nm) without any co-catalyst. Controllable experiments suggest that no appreciable H_2 is produced in the absence of either photocatalyst or light irradiation. Figure 9D shows the H_2 generation under light irradiation up to 3h. No H_2 was produced when pure TiO_2 hollow is served as photocatalyst because they do not absorb visible light. Only very a little amount of H_2 is generated for pure g-C_3N_4, which is probably due to the rapid recombination of electron-hole pairs. When N-TCN-500 is used as a photocatalyst, a large increase of H_2 evolution is observed. The photocatalytic activity of N-TCN-x enhances with increasing g-C_3N_4 content from N-TCN-500 to N-TCN-700. N-TCN-700 photocatalyst has the highest H_2-production activity (296.4 μmol g^{-1} h^{-1}), which is 25.8 times higher than that of pure g-C_3N_4. The corresponding apparent quantum efficiency (AQE) is 1.2% at 420 nm. Further increasing the amount of CY (N-TCN-1000) give rise to slightly depressed activity but it is still superior to pure g-C_3N_4. Because both heterostructure and amount of g-C_3N_4, together with the surface area, influence on the visible light photocatalytic activity for g-C_3N_4-/N-TiO_2 composites, we compared the H_2 production normalized by the surface areas of various photocatalysts, as shown in Figure 10A. It

is found that N-TCN-700 and N-TCN-1000 have the higher activity than pure g-C_3N_4, N-TCN-500 with a small content of g-C_3N_4, and N-TCN-200 with N doping. This means that both heterostructure and amount of g-C_3N_4 play significant roles on enhancing the photocatalytic activity for various photocatalysts. The recyclability of N-TCN-700 is measured by three cycles and there is no decrease, indicating the good stability of sample (Figure 10B).

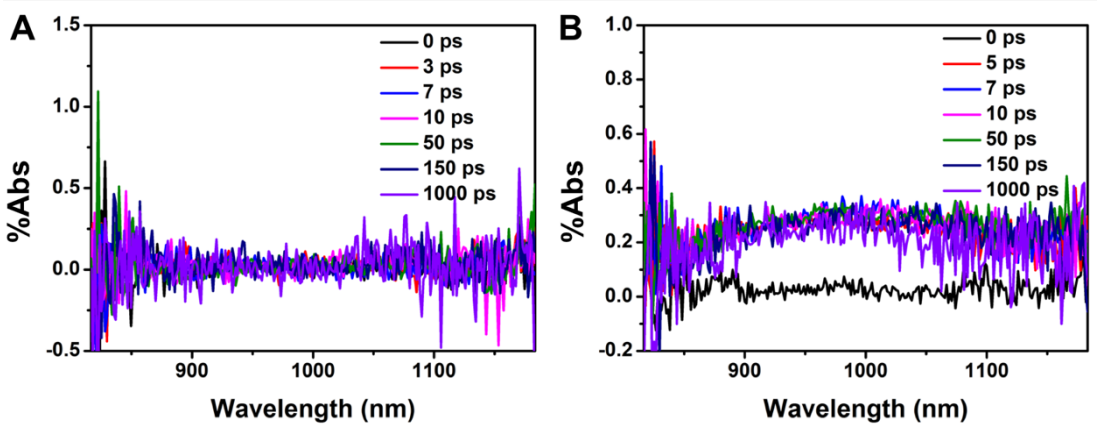

Figure 11 Time-resolved diffuse reflectance spectra of pure TiO_2 (A), and N-TCN-200 (B).

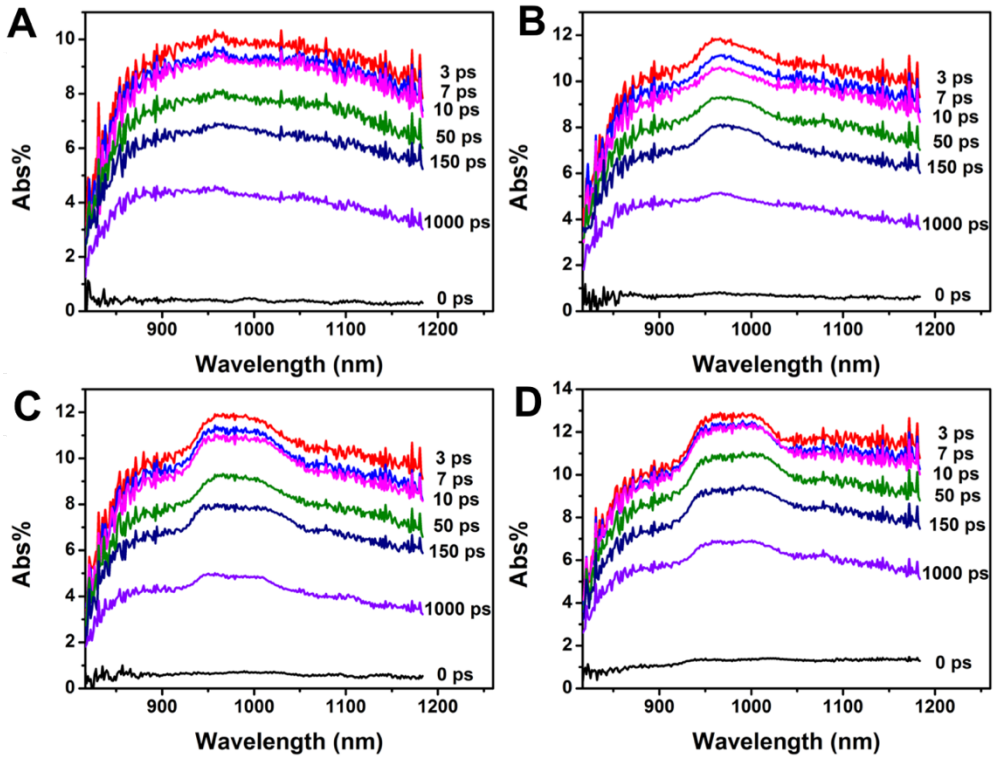

Figure 12 Time-resolved diffuse reflectance spectra of N-TCN-500 (A), N-TCN-700 (B), N-TCN-1000 (C) and g-C_3N_4 (D).

Based on the results described above, we suggest that important factors for N-TCN-x with higher photocatalytic activity lie in the co-operation effect of N element doping into TiO_2 and the construction of intimate heterostructure between N-TiO_2 and g-C_3N_4 (N-TCN-x). The time-resolved diffuse reflectance (TDR) spectroscopy, a powerful analytical tool for investigating ultrafast processes in photocatalysis under various conditions,[38,39] is employed in order to confirm this suggestion, probing the initial charge lifetimes and charge transfer processes after the band gap excitation. We have recently systematically studied the charge transfer dynamics in N-TiO_2 mesocrystals.[40] Upon visible light irradiation of N-TiO_2 (N-TCN-200), electrons are excited from N 2p in the isolated localized electronic state to the CB of TiO_2, while the generated holes are localized at N 2p state.[41] In fact, transient absorption assigned to electrons and holes is observed (Figure 11B). Additionally, due to the large band gap of pure TiO_2, no charge was generated from visible light irradiation as shown in Figure 11A. Because the charge carriers in the localized energy states transport freely, N doping enables the efficient visible-light-driven photocatalytic activity of N-TCN-200.[41,42] Difference absorption spectra between N-TCN-x and pure g-C_3N_4 are recorded at different time delays after the excitation of the samples with 420-nm pump pulse as shown in Figure 12. The spectra of N-TCN-x exhibit a broad absorption band in 950-1050 nm region as same as pure g-C_3N_4, assigning to the trapped and free (or shallowly trapped) electrons in semiconductors.[39,43,44] By comparing the signal intensity of N-TCN-200 and pure g-C_3N_4, we can conclude that it is mainly photoexcited electrons generated in g-C_3N_4 that account for the photocatalysis reaction. All transient absorption spectra intensity reaches highest within 3 ps after laser flash, and then gradually decays as shown in Figure 12. Compared with pure g-C_3N_4 in the period of 3-10 ps, the absorption of N-TCN-x decays more rapidly, and N-TCN-700 exhibits the fastest decay rate. Even though the transient absorption signal is detected in N-TCN-200, the intensities of N-TCN-x are much higher than that of N-TCN-200 (N-TiO_2), indicating that most electrons are generated by g-C_3N_4 rather than N-TiO_2.

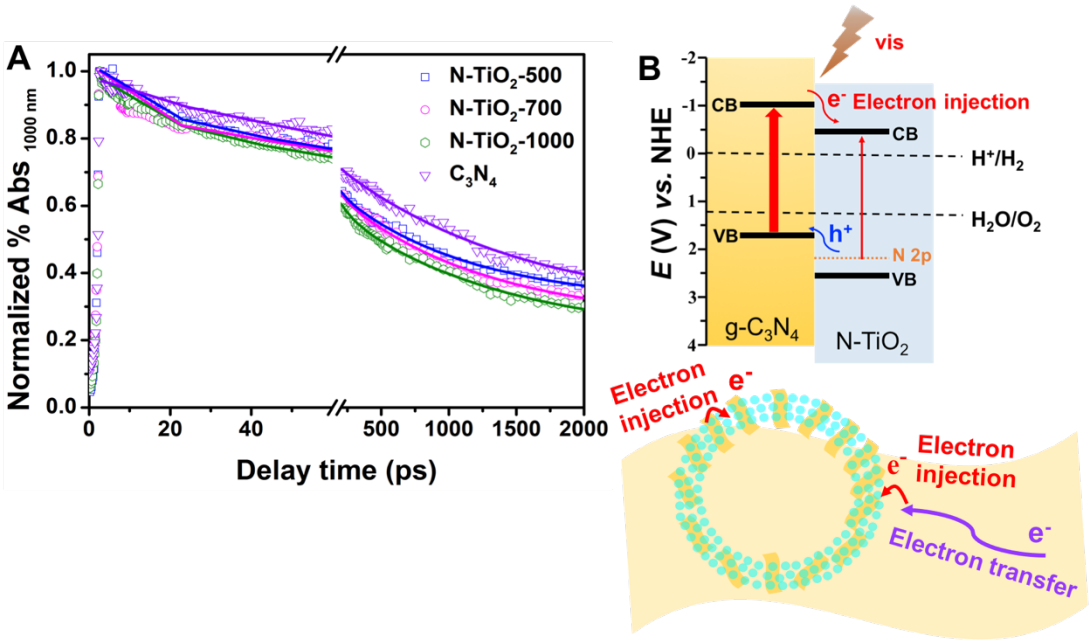

Figure 13 Normalized transient absorption trace from N-TCN-500, N-TCN-700, N-TCN-1000 and g-C_3N_4 after 420 nm laser irradiation (A). Energy diagram and schematic illustration of electron transfer in g-C_3N_4 and electron injection from g-C_3N_4 to N-TiO_2 during irradiation of N-TCN-x under visible light (B).

To clarify the decay kinetics, the absorption-time profiles were recorded at 1000 nm for N-TCN-x and pure g-C_3N_4 as shown in Figure 13A, which were fitted by a multi-exponential function. The smallest number of individual decay lifetimes, τ_i, which resulted in the minimum χ^2, was used for each fit.[45] The decay signal of pure g-C_3N_4 was fitted by a biexponential decay function with time constants of 48 ps (30%) and 1384 (70%) (Table 3). After hybridization g-C_3N_4 with N-TiO_2, the decays of N-TCN-x were fitted by a triexponential function and the lifetimes of electrons were found to decrease, indicating that a new electron decay pathway opens as N-TiO_2 traps the electrons, with a fast decay time of 4-13 ps. The calculated fitting parameters are summarized in Table 3. The lifetimes of electrons are tentatively explained using diffusion coefficient of electrons in g-C_3N_4. The mean lifetime required for electron diffusion from neighboring g-C_3N_4 to N-TiO_2 nanoparticles is within several picoseconds, which is reasonably consistent with the first lifetime (τ_1 = 4-13 ps).[46] The electrons injections from g-C_3N_4 into CB of N-TiO_2 with the distance over tens and hundreds nanometers are expected to occur in several tens and thousands picoseconds time scale, respectively, which were observed as the second and third lifetimes (τ_2 = 77-

106 and τ_3 = 979-1201 ps, respectively) of electrons in N-TCN-x. Such multi components of the lifetimes are reasonably explained by large scale layered structure of g-C_3N_4.

Consequently, we conclude that the band bending at the interface of type II heterojunction due to the difference of potential energies between N-TiO_2 and g-C_3N_4 induces a built-in field (Figure 13B), which promotes photogenerated electrons migrating to CB of N-TiO_2.[47] The large interfacial area of N-TCN-x results in sufficient interface for efficient charge transfer and photocatalytic reaction. It is also noteworthy that the component with τ_1 = 4.2 ps exists at 24% ratio among whole electrons for N-TCN-700 (Figure 11A), showing shorter τ_1 and larger ratio than those of N-TCN-500 and N-TCN-1000. This phenomenon indicates a better contact between N-TiO_2 and g-C_3N_4 in N-TCN-700 than in other N-TCN-x, leading to a faster and more efficient electron transfer. The differences of τ_2 of these three N-TCN-x correspond to the fact that the electron mobility decreases with decreasing the number of g-C_3N_4 layers, similarly for graphene.[48] SEM and TEM images show that the number of g-C_3N_4 layers for N-TCN-1000 is much larger than that for N-TCN-500 and N-TCN-700, suggesting a decrease of the electron mobility for N-TCN-500 and N-TCN-700. Therefore, N-TCN-1000 exhibited the longest τ_2. Considering the values of TGA and BET together with the transient absorption analysis, N-TCN-700 is found to possess the highest photocatalytic activity among N-TCN-x.

Table 3 Kinetic parameters of transient absorption decays

Sample	**N-TCN-500**	**N-TCN-700**	**N-TCN-1000**	**g-C_3N_4**
τ_1 (ps)	9.2 ± 1.2 (19%)	4.2 ± 0.5 (24%)	12.9 ± 1.3 (19%)	48.0 ± 2.4 (30%)
τ_2 (ps)	77 ± 8 (28%)	78 ± 7 (25%)	106 ± 11 (28%)	1384 ± 116 (70%)
τ_3 (ps)	979 ± 83 (53%)	1098 ± 103 (51%)	1201 ± 137 (53%)	-
χ^{2a}	1.1×10^{-4}	1.2×10^{-4}	7.0×10^{-5}	1.2×10^{-4}

[a]The χ^2 term is used to estimate the reliability of the fitting model and the experimental data; the fit is good if χ^2 is minimized.

4. Conclusion

In summary, a facile one-pot impregnated method was explored here to synthesize products gradually varying from N-TiO_2 to N-TCN-x by mixing and calcining TiO_2 hollow nanospheres with cyanamide. Due to the mesoporous structure of TiO_2, g-C_3N_4 is formed both inside and outside of nanospheres. In addition, formation of g-C_3N_4 outside of TiO_2 small grains (3 nm) restrains their recrystallization to large particles (20 nm). Among series of N-TCN-x, N-TCN-700 exhibited the best activity with H_2 evolution of 388 μmol g^{-1} h^{-1} under visible light irradiation ($\lambda \geqslant 420$ nm) without any co-catalyst. Electrochemical and spectroscopic measurements were performed to clarify the type II band alignment for favorable charge transfer between g-C_3N_4 and N-TiO_2. Charge carrier lifetimes of N-TCN-x were measured by femtosecond time-resolved diffused reflectance spectroscopy to indicate that photogenerated electrons in CB of g-C_3N_4 transfers to that of N-TiO_2 within several to tens picoseconds, leading to efficient charge separation and photocatalytic activity. We believe that the design and synthesis of well-contact multicomponent heterostructures as photoresponsible materials have great potentials for clean energy applications.

5. References

(1) Fujishima, A.; Honda, K. *Nature*, **1972**, 238, 37-38.

(2) Tu, W.; Zhou, Y.; Liu, Q.; Tian, Z.; Gao, J.; Chen, X.; Zhang, H.; Liu, J.; Zou, Z. *Adv. Funct. Mater.* **2012,** 22, (6), 1215.

(3) Luo, J.; Xia, X.; Luo, Y.; Guan, C.; Liu, J.; Qi, X.; Ng, C. F.; Yu, T.; Zhang, H.; Fan, J. *Adv. Energy Mater.* **2013,** 3, (6), 737.

(4) Pan, J. H.; Han, G.; Zhou, R.; Zhao, X. *Chem. Commun.* **2011,** 47, (24), 6942.

(5) Jiang, Z.; Lv, X.; Jiang, D.; Xie, J.; Mao, D. *J. Mater. Chem. A* **2013**, 1, 14963.

(6) Zhao, W.; Ma, W.; Chen, C.; Zhao, J.; Shuai, Z. *J. Am. Chem. Soc.* **2004,** 126, (15), 4782.

(7) Zhang, P.; Tachikawa, T.; Fujitsuka, M.; Majima, T. *ChemSusChem* **2016**, 9, 617.

(8) Chen, X.; Burda, C. *J. Am. Chem. Soc.* **2008**, 130, 5018-5019.

(9) Shi, X.; Ji, Y.; Hou, S.; Liu, W.; Zhang, H.; Wen, T.; Yan, J.; Song, M.; Hu, Z.; Wu, X. *Langmuir* **2015**, 31, 1537-1546.

(10) Gu, Q.; Long, J.; Zhuang, H.; Zhang, C.; Zhou, Y.; Wang, X. *Phys. Chem. Chem. Phys.* **2014**, 16, 12521-12534.
(11) Wang, M.; Hu, Y.; Han, J.; Guo, R.; Xiong, H.; Yin, Y. *J. Mater. Chem. A* **2015**, 3, 20727.
(12) Cheng, C.; Amini, A.; Zhu, C.; Xu, Z.; Song, H.; Wang, N. *Sci. Rep.* **2014**, 4, 4181.
(13) Lian, Z.; Xu, P.; Wang, W.; Zhang, D.; Xiao, S.; Li, X.; Li, G. *ACS Appl. Mater. Interfaces* **2015**, 7, 4533.
(14) Yang, S.; Gong, Y.; Zhang, J.; Zhan, L.; Ma, L.; Fang, Z.; Vajtai, R.; Wang, X.; Ajayan, P. M. *Adv. Mater.* **2013**, 25, 2452.
(15) Han, Q.; Wang, B.; Zhao, Y.; Hu, C.; Qu, L. *Angew. Chem. Int. Ed.* **2015**, 54, 11433.
(16) Wang, X.; Maeda, K.; Thomas, A.; Takanabe, K.; Xin, G.; Carlsson, J. M.; Domen, K.; Antonietti, M. *Nat. Mater.* **2009**, 8, 76.
(17) Albero, J.; Barea, E. M.; Xu, J.; Mora-Seró, I.; Garcia, H.; Shalom, M. *Adv. Mater. Interfaces* **2017**, 4. 1600265.
(18) Zhou, S.; Liu, Y.; Li, J.; Wang, Y.; Jiang, G.; Zhao, Z.; Wang, D.; Duan, A.; Liu, J.; Wei, Y. *Appl. Catal. B: Environ.* **2014**, 158–159, 20-29.
(19) Jiang, Z.; Zhu, C.; Wan, W.; Qian, K.; Xie, J. *J. Mater. Chem. A* **2016**, 4, 1806-1818.
(20) Shalom, M.; Gimenez, S.; Schipper, F.; Herraiz-Cardona, I.; Bisquert, J.; Antonietti, M. *Angew. Chem.* **2014**, 126, 3728-3732.
(21) Xu, J.; Herraiz-Cardona, I.; Yang, X.; Antonietti, M.; Shalom, M. *Adv. Optical Mater.* **2015**, 3, 1052-1058.
(22) Pesci, F. M.; Cowan, A. J.; Alexander, B. D.; Durrant, J. R.; Klug, D. R. *J. Phys. Chem. Lett.* **2011**, 2, 1900.
(23) Ma, Y.; Pendlebury, S. R.; Reynal, A.; Le Formal, F.; Durrant, J. R. *Chem. Sci.* **2014**, 5, 2964.
(24) Joo, J. B.; Zhang, Q.; Dahl, M.; Lee, I.; Goebl, J.; Zaera, F.; Yin, Y. *Energy Environ. Sci.* **2012**, 5, 6321.
(25) Zheng, D.; Huang, C.; Wang, X. *Nanoscale* **2015**, 7, 465.
(26) Sun, J.; Zhang, J.; Zhang, M.; Antonietti, M.; Fu, X.; Wang, X. *Nat. Commun.* **2012**, 1139.
(27) Sun, J.; Fu, Y.; He, G.; Sun, X.; Wang, X. *Appl. Catal. B: Environ.* **2015**, 165, 661.
(28) Li, K.; Zeng, Z.; Yan, L.; Luo, S.; Luo, X.; Huo, M.; Guo, Y. *Appl. Catal. B: Environ.* **2015**, 165, 428.
(29) Zhang, G.; Zhang, J.; Zhang, M.; Wang, X. *J. Mater. Chem.* **2012**, 22, 8083.
(30) Yu, J. C.; Ho, W.; Yu, J.; Hark, S. K.; Iu, K. *Langmuir*, **2003**, 19, 3889.
(31) Chai, B.; Peng, T.; Mao, J.; Li, K.; Zan, L. *Phys. Chem. Chem. Phys.*, **2012**, 14,

16745
(32) Yan, S. C.; Li, Z. S.; Zou, Z. G. *Langmuir*, **2009**, 25, 10397.
(33) Soni, S. S.; Henderson, M. J.; Bardeau, J. F.; Gibaud, A. *Adv. Mater.* **2008**, 20, 1493.
(34) Lin, J.; Shen, J.; Wang, R.; Cui, J.; Zhou, W.; Hu, P.; Liu, D.; Liu, H.; Wang, J.; Boughton, R. I. *J. Mater. Chem.* **2011**, 21, 5106.
(35) Shifu, C.; Sujuan, Z.; Wei, L.; Wei, Z. *J. Hazard. Mater.* **2008**, 155, 320.
(36) Tong, J.; Zhang, L.; Li, F.; Li, M.; Cao, S. *Phys. Chem. Chem. Phys.* **2015**, 17, 23532.
(37) Yuan, L.; Yang, M.-Q.; Xu, Y.-J. *J. Mater. Chem. A* **2014**, 2, 14401.
(38) Furube, A.; Asahi, T.; Masuhara, H.; Yamashita, H.; Anpo, M. *J. Phys. Chem. B* **1999**, 103, 3120.
(39) Tachikawa, T.; Fujitsuka, M.; Majima, T. *J. Phys. Chem. C* **2007**, 111, 5259.
(40) Zhang, P.; Fujitsuka, M.; Majima, T. *Appl. Catal. B: Environ.* **2016**, 185, 181.
(41) Cai, X.; Zhang, J.; Fujitsuka, M.; Majima, T. *Appl. Catal. B: Environ.* **2017**, 202, 191.
(42) Umezawa, N.; Ye, J. *Phys. Chem. Chem. Phys.* **2012**, 14, 5924.
(43) Ravensbergen, J.; Abdi, F. F.; van Santen, J. H.; Frese, R. N.; Dam, B.; van de Krol, R.; Kennis, J. T. *J. Phys. Chem. C* **2014**, 118, 27793.
(44) Bian, Z.; Tachikawa, T.; Zhang, P.; Fujitsuka, M.; Majima, T. *J. Am. Chem. Soc.* **2014**, 136, 458.
(45) Milleville, C. C.; Pelcher, K. E.; Sfeir, M. Y.; Banerjee, S.; Watson, D. F. *J. Phys. Chem. C* **2016**, 120, 5221.
(46) Zhang, P.; Tachikawa, T.; Fujitsuka, M.; Majima, T. *Chem. Commun.* **2015**, 51, 7187.
(47) Resasco, J.; Zhang, H.; Kornienko, N.; Becknell, N.; Lee, H.; Guo, J.; Briseno, L.; Yang, P. *ACS Cent. Sci.* **2016**, 2, 80.
(48) Xu, J.; Zhang, L.; Shi, R.; Zhu, Y. *J. Mater. Chem. A* **2013**, 1, 14766.

Chapter 3. Efficient Charge Separation and Increased Active Sites for Semiconductor/MoS_2 Hybrids with Enhanced Photocatalytic Activity

Up to now, the photocatalytic reactions research using semiconductors have been studied and a lot of achievements have been developed, however, there are still some main key points waiting to be resolved such as the low photocatalytic efficiency. For this, two aspects have to be considered. The one is the fast recombination of photoexcited electron-hole pairs at surface or in volume during their migration process, and another is that most semiconductor photocatalysts cannot offer active sites for catalytic reactions at the surface. In order to resolve these problems, loading co-catalyst is the commonly used method. Traditionally, metal, in particular, noble metal such as Pt and ruthenium are widely used to decorate the surface of semiconductors as co-catlysts. This is due to the fact that noble metals usually have larger work function, which can easily trap the photoexcited elections to retard their recombination with holes. In addition, calculation results show that it is a necessary, but not sufficient, criterion for a material to be a good catalyst that the adsorbed H is close to that of the reactant or product (i.e., $\Delta G_{\mathrm{H}}^{\circ} \cong 0$). Therefore, Pt is chosen to be the best candidate. Nevertheless, noble metals are rare and too expensive for large-scale applications and their stability is also a big challenge. Therefore, exploring and identifying cheaper and recyclable alternatives to noble metal co-catalysts will greatly enhance the development of photocatalysis.

Among these alternatives, MoS_2 is regarded as a promising one, which belong to the class of transition metal dichalcogenides with the layered structures. The S-Mo-S sandwich-like structure is considered as a monolayer of MoS_2, which is stacked by weak van der Waals interactions. Density functional theory (DFT) calculations found that the computational free energy of atomic hydrogen bonding to the MoS_2 edge was close to that of the Pt, and both of them approached to zero. Additionally, the sulfur atom bounded to hydrogen is 2-fold coordinated to Mo atoms. However, there is rarely reports on the investigations of structure and shape influences on the photocatalytic

hydrogen evolution performance of MoS_2 co-catalyst and the detailed electron transfer kinetics between semiconductors and MoS_2, which are the main points in this chapter.

Part 3-1. Faster Electron Injection and More Active Sites for Efficient Photocatalytic H_2 Evolution in g-C_3N_4/MoS_2 Hybrid

1. Introduction

Increased environmental crisis and energy drought have promoted the development of new technologies to harvest energy from solar light.[1] Therefore, a large amount of efforts has been devoted to nanostructured semiconductors as building blocks for next-generation energy conversion devices, such as photocatalysts.[2-4] Unfortunately, it is still difficult to develop a high-efficiency material for photocatalysis only by using a single semiconductor due to the fast recombination of electron-hole pairs along their migration process and therefore, retardation of recombination process becomes impendent. Incorporating co-catalysts is one of widely used strategies because they could not only provide active sites, but also separate electron-hole pairs rapidly before these charges relaxing to their lower energy states.[5-7] In addition, the development of materials for enhancing photocatalytic activity also provides new information on photophysical properties that improve efficiency, thereby guiding improvements in materials synthesis and processing.

Recently, many reports indicated that two-dimensional MoS_2 nanosheets could work as an effective co-catalyst for water splitting hydrogen generation and even become a promising alternative to noble-metal co-catalysts.[8-10] Similar to graphene, current researches were mostly confined to a few or monolayered MoS_2, because their bandgap is expanded due to the quantum confinement effect and increased number of unsaturated sulfur atoms useful for adsorption of protons.[11-14] However, the activity of MoS_2 with nanodot structure is rarely studied.[15] In addition, even though the electron transfer between semiconductors and MoS_2 with monolayer (or several layer) structure has been explored,[10,16] a systematic study on the shape, structure, and deposition route of the MoS_2 co-catalyst is still required to characterize the photoinduced electron

injection kinetics and detailed mechanisms for photocatalytic hydrogen evolution.

For the semiconductor/co-catalyst hybrids, single-particle photoluminescence spectroscopy (SPS) and femtosecond time-resolved transient absorption (fs-TAS) play significant roles in understanding fundamental photophysical processes and how charge transfer dictates photoactivities. SPS is often used to measure the structural, photochemical characters and radiative recombinations owing to its high sensitivity, non-destructive character, and spatial resolution.[17-19] Importantly, this measurement allows us to monitor the properties of individual nanostructure. fs-TAS enables direct observation of the dynamics of charge carrier and non-radiative recombination process in picosecond time scale.[20,21] In addition, it also helps us to explore the fundamental reasons for the photocatalytic activity.[20,21] Therefore, such SPS and fs-TAS are used as complementary measurements for probing and observing both radiative and non-radiative recombination processes.[22-24]

In the present study, MoS_2 nanodots have been successfully loaded on the surface of g-C_3N_4 via an adsorption-*in situ* photodeposition method. It was found that the photocatalytic activity of g-C_3N_4 could be greatly enhanced after loading MoS_2 nanodots, even in the comparison with that of monolayer MoS_2 modified g-C_3N_4. Based on the results of SPS and fs-TAS measurements, electron transfer dynamics, injection rate, and injection efficiency of these two g-C_3N_4/MoS_2 hybrids were explored. Proper explanations were proposed to account for the improved photocatalytic hydrogen evolution activity of various photocatalytic materials. To the best of our knowledge, this is the first detailed report on the differences in the catalytic activity of monolayer and nanodot MoS_2, and would be a stepping stone for designing proper co-catalyst structure and deposition method for high activity.

2. Experimental Section

Preparation of g-C_3N_4. The g-C_3N_4 was prepared by a two-step calcination method. First, 5 g melamine powder was put into an alumina crucible with a cover and heated to 773 K at a heating rate of 2 K min^{-1} and kept for 2 h, then to 793 K and kept for another 2 h. The resulted product was collected and grounded into powder. Secondly,

the as-prepared g-C_3N_4 was further calcined under 793 K in an open system for 6 h at a heating rate of 2 K min^{-1}. The light yellow powder was the final g-C_3N_4 we used in this paper.

Preparation of g-C_3N_4/MoS_2. The g-C_3N_4/MoS_2-nanodot composites were synthesized by a one-step photodeposition method according to previous work with minor modification. $(NH_4)_2MoS_4$ was used as MoS_2 precursor. Typically, 20 mg g-C_3N_4 was dissolved into (8000-*V*) μL DI water and 2000 μL lactic acid mixture. Then *V* μL, 1 mg/mL $(NH_4)_2MoS_4$ water solution was added into the mixture. The solution was irradiated under 365 nm light with the deaerating with N_2 for 1 h. The products were centrifuged and washed by water and ethanol three times and dried under 60 °C. The volume of $(NH_4)_2MoS_4$ solution varied from 300, 500, 1000, to 1500 μL. The resultants were named as MC-*X* (*X* = 0.96%, 1.6%, 3.2%, and 4.8%), where *X* referred to the weight percent of the loaded MoS_2.

The g-C_3N_4/MoS_2-monolayer composites were synthesized by a two-step mixing method. Monolayer MoS_2 was achieved by ultrasonic bulk MoS_2 for 4 h and centrifugation. Then different volumes of MoS_2 solution (1.6 mg/mL) were added into 0.5 mL g-C_3N_4 ethanol suspension (10 mg/mL). The volume of MoS_2 solution increased from 50, 100, 200, to 300 μL. The mixture was heated under 60 °C with stirring. The products named as Mix-*Y* (*Y* = 1.6%, 3.2%, 6.4%, and 9.6%) were collected after drying and *Y* referred to the weight percent of the loaded MoS_2.

Photocatalytic H_2 evolution. 3 mg sample were dispersed in 5 mL aqueous solution containing 20 vol% lactic acid for H_2 evolution. Prior to the irradiation, the suspension of the catalyst was dispersed by using an ultrasonic bath, and then bubbled with argon through the reactor for 30 min to completely remove the dissolved oxygen and ensure the reactor was in an anaerobic condition. The samples were irradiated at different wavelengths using a Xenon lamp for H_2 generation (Asahi Spectra, HAL-320; 350 mW cm^{-2}). The reaction temperature was kept at about 293 K. The visible light was filtered with a nominal 400 nm cutoff filter. The volume of H_2 was measured by using a Shimadzu GC-8A gas chromatograph equipped with an MS-5A column and a thermal conductivity detector. The catalytic stability was evaluated by isolating, washing and

reusing the catalyst in a cycling experiment. The apparent quantum efficiency (AQE) was calculated using the following equation,[25]

$$\text{AQE}\ (\%) = \frac{\text{Number of evolved } H_2 \text{ molecules} \times 2}{\text{Number of incident photons}} \times 100\%.$$

Photoelectrochemical measurements. Electrochemical and photoelectrochemical measurements were performed in three-electrode quartz cells. A platinum wire was used as the counter electrode, and a Ag/AgCl electrode was used as the reference electrode. For loading sample film electrodes on glassy carbon, 4 mg of sample was added into solution containing H_2O and CH_3CH_2OH with volume ratio of 1:1. Then 50 μL Nafion was added into the solution. After ultrasonication for 10 min, 3 μL solution was took out and drop on the surface of glassy carbon. The electrode was used for photoelectrochemical measurements after drying. 0.1 M Na_2SO_4 aqueous solution was used as the electrolyte. Electrochemical impedance spectroscopy (EIS) was carried out under visible light irradiation. The Xenon lamp (550 mW cm^{-2}) was utilized as the light source in the photoelectrochemical measurements and the visible light was filtered with nominal 400 nm cutoff filter.

Single-particle PL measurements by confocal microscopy. Sample preparation for single-particle photoluminescence (PL) experiments: The cover glasses were purchased from DAICO MFG CO., Ltd. and cleaned by sonication in a 20% detergent solution (As One, Cleanace) for 7 h, followed by repeated washing with warm water 5 times. The well-dispersed aqueous suspensions of samples (g-C_3N_4, MC-3.2%, and Mix-6.4%) were spin-coated on the cleaned cover glass. The cover glass was annealed at 60 ºC for 1 h to immobilize the particles on the surface.

Single-particle PL images and emission spectra of samples were recorded by using an objective scanning confocal microscope system (PicoQuant, MicroTime 200) coupled with an Olympus, UplanSApochromat, 100×, 1.4 NA) and a circular-polarized 405 nm pulse wave laser controlled by a PDL-800B driver (PicoQuant). Typical excitation powers for the PL measurements were 120nW/cm^{-1} at the sample. The emission from the sample was collected by the same objective and detected by a single photon avalanche photodiode (Micro Photon Devices, PDM 50 CT) through a dichroic

beam splitter (Chroma, 405rdc) and a long pass filter (Chroma, HQ430CP). All the experimental data were obtained at room temperature.

Time-resolved diffuse reflectance transient absorption measurements. The femtosecond diffuse reflectance transient absorption spectra were measured by the pump and probe method using a regeneratively amplified titanium sapphire laser (Spectra-Physics, Spitfire Pro F, 1kHz) pumped by a Nd:YLF laser (Spectra-Physics, Empower 15). The seed pulse was generated by a titanium sapphire laser (Spectra-Physics, Mai Tai VFSJW; fwhm 80 fs). Second harmonic oscillation of the output (400 nm, 4 μJ $pulse^{-1}$) was used as the excitation pulse. A white light continuum pulse, which was generated by focusing the residual of the fundamental light on a sapphire crystal after the computer controlled optical delay, was divided into two parts and used as the probe and the reference lights, of which the latter was used to compensate the laser fluctuation. Both probe and reference lights were directed to the sample powder coated on the glass substrate, and the reflected lights were detected by a linear InGaAs array detector equipped with the polychromator (Solar, MS3504). All measurements were carried out at room temperature.

Characterization of materials. The samples were characterized using X-ray diffraction (XRD, Rigaku Rint-2500, CuKαsource), and HRTEM (JEOL JEM 3000F, operated at 300kV). The steady-state UV-visible absorption and diffuse reflectance spectra were measured by UV-visible-NIR spectrophotometers (Shimadzu UV-3100 and Jasco V-570, respectively) at room temperature. The XPS measurements were performed with the PHI X-tool 8ULVAC-PHI.

3. Results and Discussion

As illustrated in Figure 1A, g-C_3N_4/MoS_2-nanodot hybrid was fabricated by single step *in situ* photodeposition. Based on the volume of $(NH_4)_2MoS_4$ solution, g-C_3N_4/MoS_2-nanodot samples were named as MC-*X*. While synthesizing g-C_3N_4/MoS_2-monolayer involved two steps, that is, ultrasonic assisted exfoliation of bulk MoS_2 into monolayer MoS_2 and then assembling with g-C_3N_4 through sonication, stirring and drying without any surface functionalization or adhesion agents. The samples were labeled as Mix-*Y*

on the basis of the volume of monolayer MoS_2 solution added in the mixture.

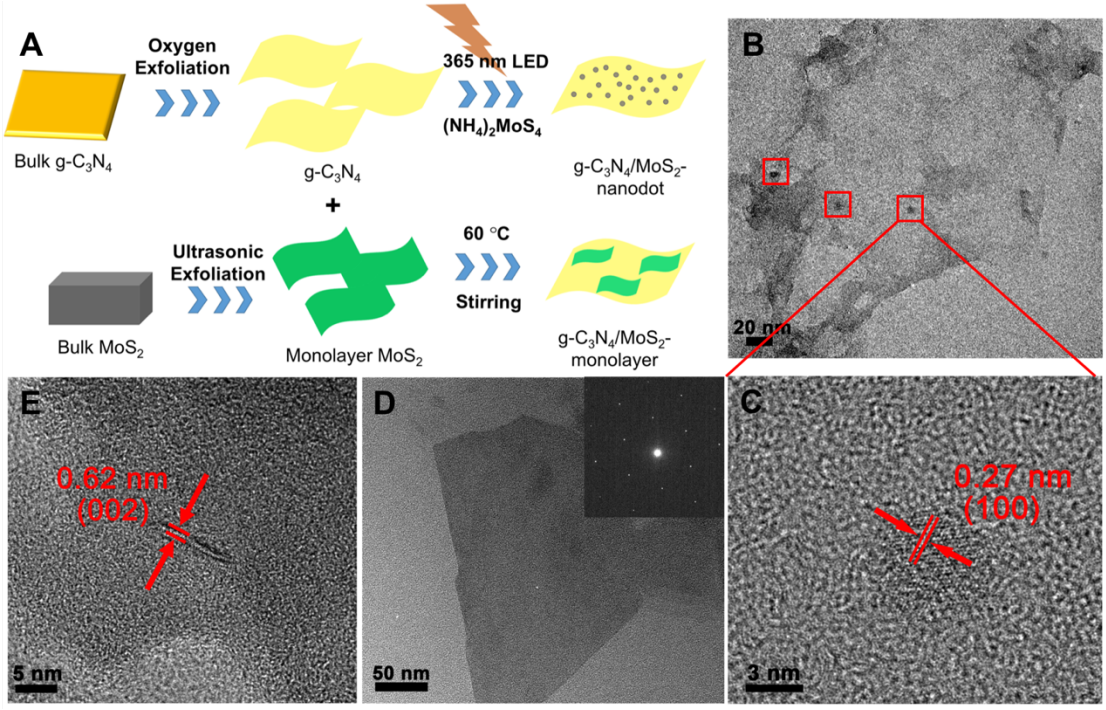

Figure 1 (A) Schematic illustration of synthesizing g-C_3N_4/MoS_2-nanodot and g-C_3N_4/MoS_2-monolayer hybrids. (B) TEM image of MC-3.2%. (C) HRTEM image of MoS_2 nanodot. (D) TEM image of exfoliated MoS_2, the inset shows the SAED pattern of MoS_2 monolayer plane. (E) TEM image of Mix-6.4% composite.

Morphology and microstructure of the as-prepared samples were characterized by transmission electron microscopy (TEM). After photodeposition of MoS_2 nanodots, the morphology and structure of g-C_3N_4 show no change (Figures 1B). In addition, MoS_2 nanodots smaller than 10 nm deposited on the surface of g-C_3N_4 are observed clearly. High resolution TEM (HRTEM) image of individual MoS_2 nanodot is given in Figure 1C, showing a typical lattice fringes with a spacing of 0.27 nm which can be assigned to the (100) planes of MoS_2.[26] Figure 1D shows that the ultrasonic exfoliated MoS_2 moieties are nearly transparent sheets and the SAED pattern also indicates hexagonal symmetry of the atomic arrangement. According to atomic force microscopy (AFM) resutls, the size and thickness of MoS_2 layer are found to be 100 ~ 200 nm and ~ 0.80 nm, respectively, corresponding to the monolayer structure (Figure 2). HRTEM image of Mix-6.4% is shown in Figure 1E and a typical layer MoS_2 with an interlayer distance of 0.62 nm, corresponding to the (002) planes of MoS_2, could be observed, indicating that MoS_2 still kept monolayer after combining with g-C_3N_4.

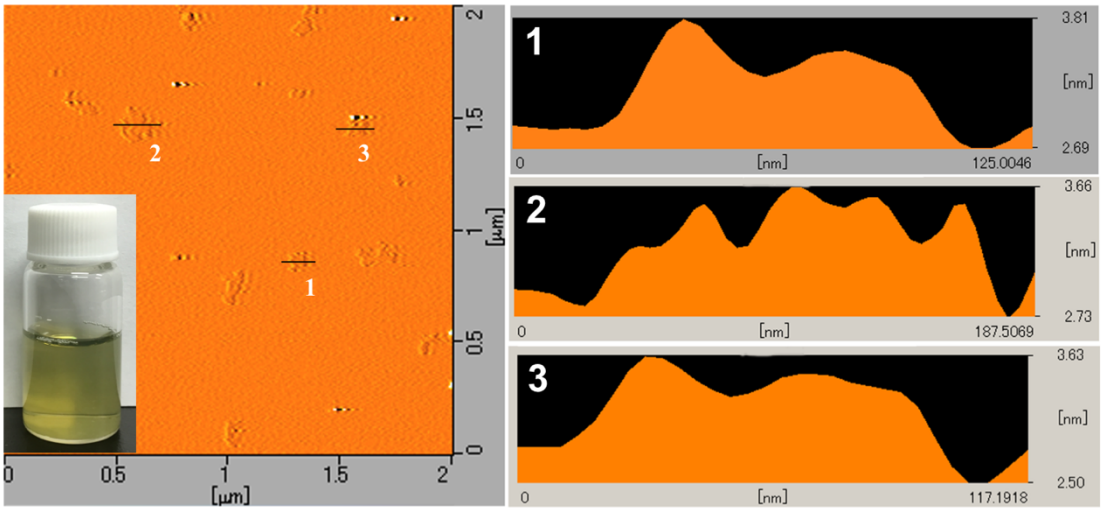

Figure 2 AFM image of MoS_2. The inset image is photograph of exfoliated MoS_2 solution.

In addition, elemental mapping analysis of MC-3.2% in Figure 3 clear demonstrates that MoS_2 nanodots are decorated on the surface of g-C_3N_4 homogeneously.

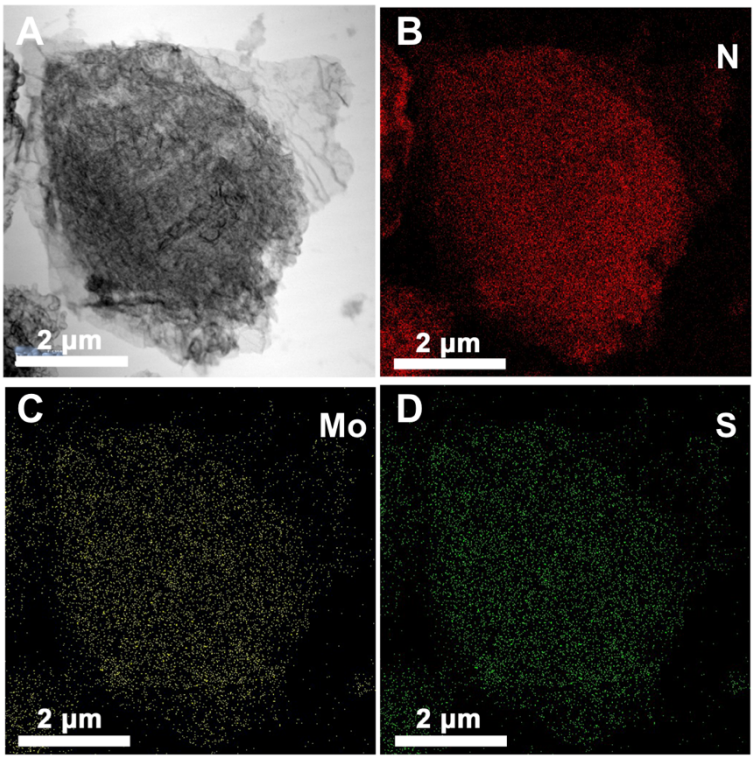

Figure 3 TEM image (A) and elemental mapping of N (B), Mo (C), and S (D) of MC-3.2%.

Texture properties of samples were characterized by FT-IR and XRD as shown in Figure 4. As expected, g-C_3N_4, MC-3.2%, and Mix-6.4% samples displayed similar FT-IR spectra due to low content of MoS_2, which also indicated that the structure of g-

C_3N_4 was not changed after modifying with MoS_2. Typical vibration bands in the range from 1000 to 2000 cm^{-1} are assigned to the C=N and C-N stretching vibration modes, and the sharp peak at 808 cm^{-1} is ascribed to the breathing vibration of triazine units.[27] Similar to the results of FT-IR, XRD patterns also only exhibited the characteristic peaks of g-C_3N_4, and MoS_2 peaks could not be observed. The peak located at 27.4° corresponds to the (002) stacking layered structure while the 12.9° peak is attributed to the (100) in-plane repeated units.[28] Interestingly, it is found that the characteristic peak at 27.4° in the XRD pattern slightly shifted to a larger value in MC-3.2%, while there was no shift in Mix-6.4%, indicating a stronger interaction between g-C_3N_4 and MoS_2 in MC-3.2% than that in Mix-6.4%.[29]

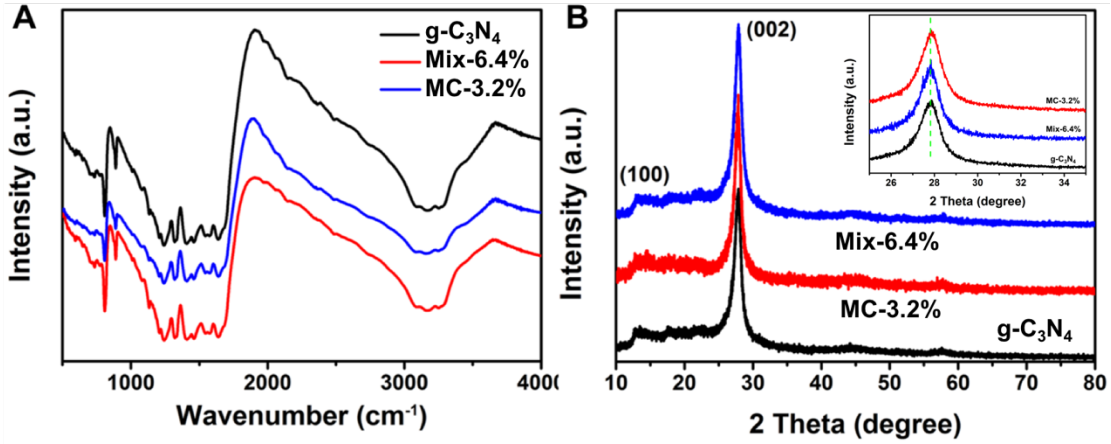

Figure 4 FT-IR spectra and XRD patterns of g-C_3N_4, MC-1000, and Mix-200.

X-ray photoelectron spectroscopy (XPS) measurement was carried out to further confirm the photodeposition of MoS_2 on g-C_3N_4 surface. Figure 5A displays the high-resolution XPS spectrum of C 1s, which exhibits two peaks at 284.8 and 288.2 eV in MC-1000 and can be assigned to C-C and N-C=N of g-C_3N_4, respectively.[27] In the N 1s XPS spectrum (Figure 5B), peaks at 398.3, 398.9, and 400.4 eV in MC-1000 are assigned to C=N-C, N-$(C)_3$, and C-N-H, respectively.[27] The peak centered at 404.4 eV is also observed by other group, however, the assignment is not fully understood.[30] Comparing to pristine g-C_3N_4, the peak positions of C 1s and N 1s in MC-3.2% sample are shifted to higher binding energy by approximately 0.6 eV, indicating an obvious interaction between photodeposited MoS_2 nanodots and g-C_3N_4.[31,32] However, the peak positions of these two elements in Mix-200 show no shift. The Mo 3d XPS spectrum

of MC-1000 gives two peaks centered at 229.4 and 232.6 eV (Figure 5C), which could be the Mo $3d_{5/2}$ and Mo $3d_{3/2}$, respectively, demonstrating that Mo is in the +4 valence state.[33-35] This result again confirms that Mo^{6+} in $(NH_4)_2MoS_4$ is successfully reduced to Mo^{4+} during the photoirradiation reduction process. The characteristic peaks of S 2s, $2p_{1/2}$, and $2p_{3/2}$ orbitals for S^{2-} are observed at 226.7, 162.9, and 161.9 eV in MC-3.2%, respectively (Figure 5D).[33-35] By comparing with pure MoS_2, it is also illustrated that the peak positions of molybdenum and sulfur in MC-3.2% exhibit a distinct shift while those in Mix-6.4% almost show no change. It has been reported that there are several kinds of S-bonding configurations existing in the molybdenum sulfide materials, including one kind of saturated basal-plane S atom and unsaturated terminal S atom.[36,37] In Figure 5D, two peaks located at 161.9 and 162.9 eV correspond to saturated basal-plane S atom and unsaturated terminal S atom, respectively.[38] According to the XPS fitting results, the atomic ratio between unsaturated S atom and saturated S atom in Mix-6.4% and MC-3.2% is 1:3.5 and 2.4:1, respectively. Considering that the weight ratio of MoS_2 in Mix-6.4% and MC-3.2%, this increased ratio of terminal S atom and basal S atom from MoS_2 monolayer to nanodot indicates more unsaturated S atoms in MC-3.2%. By comparing with pure MoS_2, it is also illustrated that the peak positions of molybdenum in MC-3.2% exhibit an obvious shift, while those in Mix-6.4% have a slightly change. In addition, the atomic ratios of N:Mo in MC-3.2% and Mix-6.4% are calculated corresponding to 109:1 and 54:1, respectively. These results indicate that the amount of MoS_2 in Mix-6.4% is larger than that in MC-3.2%. Based on these XPS analysis, a stronger interaction between MoS_2 nanodot and g-C_3N_4 is realized at the interface and more active unsaturated S atoms appear in MoS_2 nanodot.

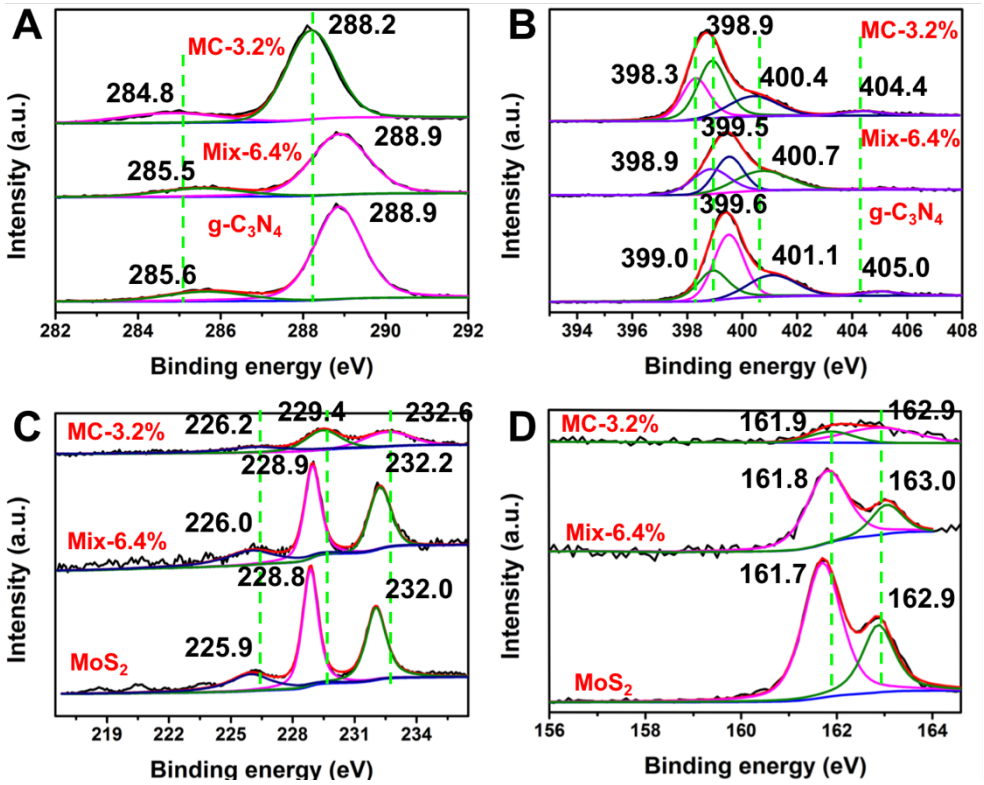

Figure 5 XPS spectra of C 1s (A), N 1s (B), Mo 3d (C), and S 2p (D) in MC-3.2%, Mix-6.4%, pure g-C_3N_4, and pure MoS_2.

Optical properties of pure g-C_3N_4, MC-*X*, and Mix-6.4% samples were examined by UV-vis absorbance spectra as shown in Figure 6A. Pure g-C_3N_4 displays an absorption edge around 420 nm corresponding to the intrinsic absorption of g-C_3N_4 (approximately 2.95 eV). Photodeposition of MoS_2 has great influence on the optical property of samples. With increasing amount of MoS_2, light absorption in the range of 450-800 nm is gradually enhanced, probably because of the increased background absorption due to black or grey colored MoS_2 nanodots.[39] In contrast, the absorption spectrum of Mix-6.4% shows significant difference compared with that of MC-*X*. In addition to the absorption edge of g-C_3N_4, a small absorption edge of MoS_2 appears at approximately 700 nm and two weak absorption peaks between 600 and 700 nm corresponding to octahedral phase MoS_2 can also be observed.[25] All the spectra demonstrate that the bandgap of g-C_3N_4 has no big change after hybridization with MoS_2.

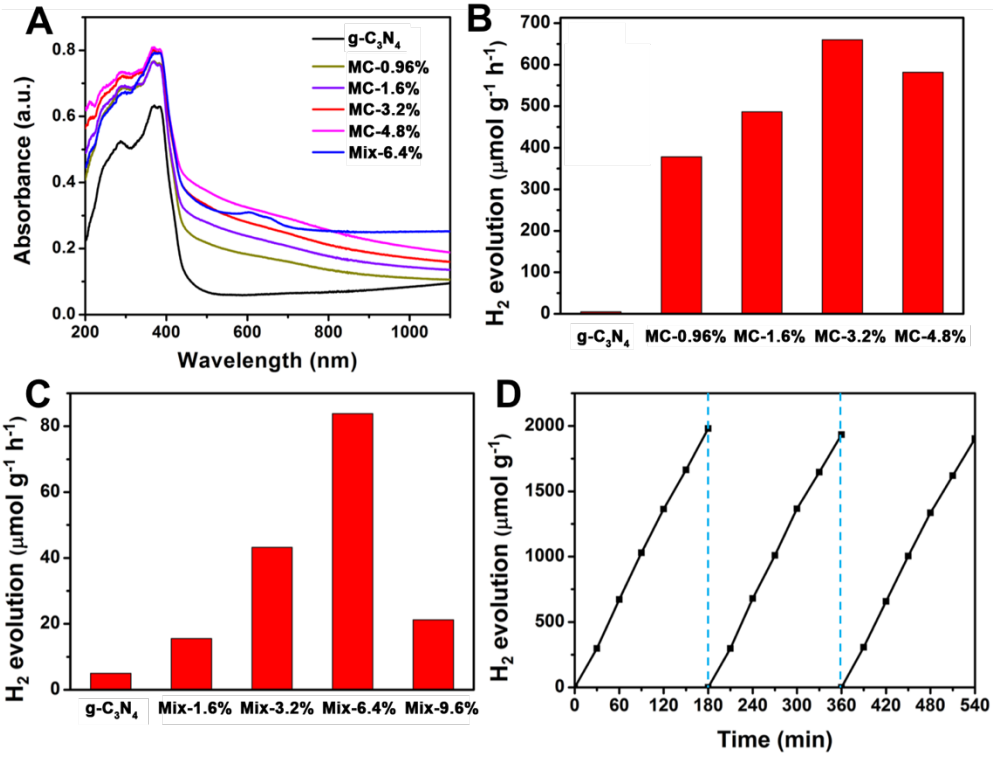

Figure 6 Diffuse-reflectance spectroscopy of g-C_3N_4, MC-*X*, and Mix-6.4% (A). Comparison of photocatalytic H_2 evolution activities of different MC-*X* samples (B) and Mix-*Y* (C). Stability test of MC-3.2% photocatalyst (D).

Photocatalytic hydrogen evolution activities of the samples were examined under visible light irradiation ($\lambda \geq 400$ nm) by using lactic acid as a sacrificial electron donor. Control experiments indicated that there is no appreciable H_2 production in the absence of photocatalysts or light irradiation. Figure 6B shows the average H_2 production rate of pure g-C_3N_4 and MC-*X* samples. For bare g-C_3N_4, the H_2 production rate is extremely low because of deep electron trapping by non-radiative process and these deeply trapped electrons cannot transfer to catalytic sites and are unable to participate in H_2 production. However, after photodeposition of MoS_2 nanodots, the evolution rate is greatly enhanced and the largest rate as high as 660 μmol g^{-1} h^{-1} is attained by using MC-3.2% as photocatalyst. On the contrary, even though monolayer MoS_2 is widely used as a co-catalyst to increase the performance of catalysts, the enhancement of H_2 production rate here is far less than the hybrid with MoS_2 nanodots (83.8 μmol g^{-1} h^{-1} for Mix-6.4% in Figure 6C). The average rate of MC-3.2% is 7.9 times higher than that of Mix-6.4%. In addition, the apparent quantum efficiency was estimated to be 5.67% and 0.64% for MC-3.2% and Mix-6.4% respectively, at $\lambda = 400 \pm 5$ nm. Based on the

same g-C_3N_4 basement, this much higher H_2 evolution production rate of MC-3.2% compared to Mix-6.4% may be partially due to the faster and more efficient electron transfer during the light irradiation. The H_2 production rate of MC-3.2% after 3 cycles shows negligible decrease (Figure 6D) and the elemental mapping of MC-3.2% after 3 cycles also indicats that MoS_2 nanodots are still anchored on the surface of g-C_3N_4 (Figure 7), which is resulted from the good stability of inherent structure for g-C_3N_4 and MoS_2 small particles.

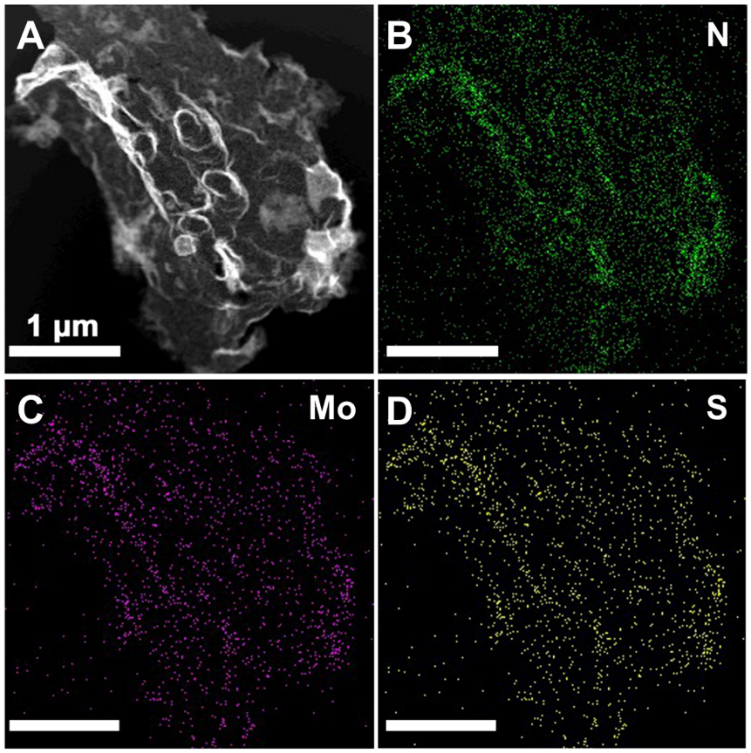

Figure 7 TEM image (A) and elemental mapping of N (B), Mo (C), and S (D) of MC-3.2% after three cycles.

The interfacial charge transfer properties between g-C_3N_4 and MoS_2 (nanodot or monolayer) were evaluated by a set of photoelectrochmical studies. Electrochemical impedance spectroscopy (EIS) is used to investigate the electrical conductivity of the samples. As illustrated in Figure 8A, the decrease of arc radius of MC-3.2% compared to that of g-C_3N_4 and Mix-6.4% suggests a smaller charge transfer resistance. Therefore, in MC-3.2%, the photoinduced electron-hole pairs can be separated more easily. This conclusion could also be confirmed by transient photocurrent (*I-t*) curves recorded for several on-off cycles of intermittent irradiation (Figure 8B), which shows a much

enhanced photocurrent of MC-3.2% over g-C_3N_4 and Mix-6.4%.

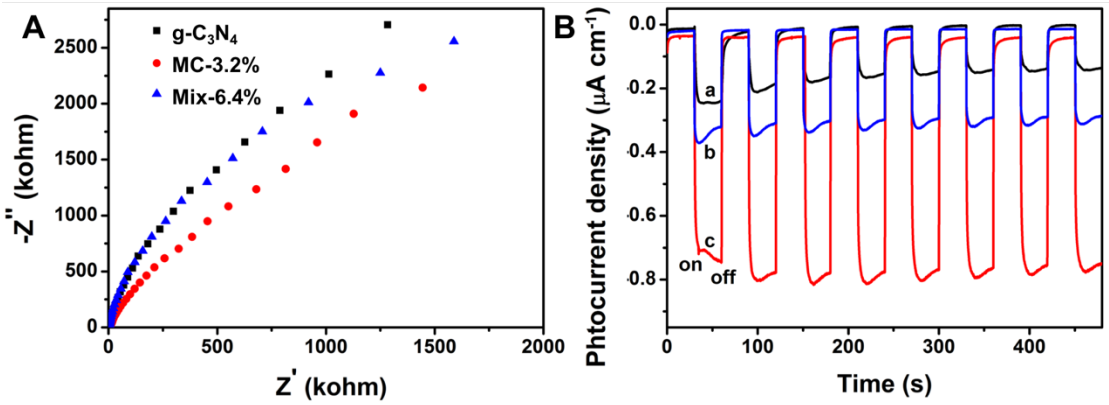

Figure 8 Electrochemical impedance spectroscopy (EIS) Nyquist plots under visible light irradiation ($\lambda \geq 400$ nm) (A) and transient photocurrent density curves (B) for g-C_3N_4 (a), Mix-6.4% (b), and MC-3.2% (c) in 0.1 M Na_2SO_4 solution.

Even though photoelectrochemistry results suggest that the electron transfer resistance is much smaller between g-C_3N_4 and MoS_2 nanodots, it is necessary to clarify the detailed mechanisms based on more straightforward proofs. Herein, we performed single-particle confocal fluorescence spectroscopy measurements to monitor the photoluminescence (PL) intensity of individual nanostructure. Firstly, all samples were spin coated on a cover glass. Single-particle PL measurements were carried out under 405-nm laser pulse irradiation, which excited the g-C_3N_4 (Figure 9A). Figures 9B and C show the typical PL images of MC-3.2% and Mix-6.4%, respectively. It is clear that the PL intensity of g-C_3N_4 decreases a lot after photodeposition of MoS_2 nanodots, while the PL intensity of Mix-6.4% shows little decrease. In order to evaluate the intensity of PL clearly, we randomly choose six points on each particle and measured their emission intensities as indicated by points 1-6 in Figures 9D-E. Pure g-C_3N_4, MC-3.2%, and Mix-6.4% showed an emission peak at approximately 460 nm, corresponding to the recombination of photogenerated electron-hole pairs. All PL spectra exhibit that the PL intensity of MC-3.2% is weaker than that of Mix-6.4%. The average PL intensities of MC-3.2% and Mix-6.4% were reduced to 19.9 % and 74.8% of pure g-C_3N_4, respectively, indicating that MoS_2 nanodots possess higher quenching efficiency. Generally, a stronger PL intensity represents a higher recombination rate of photogenerated electron and hole in semiconductors.[40]

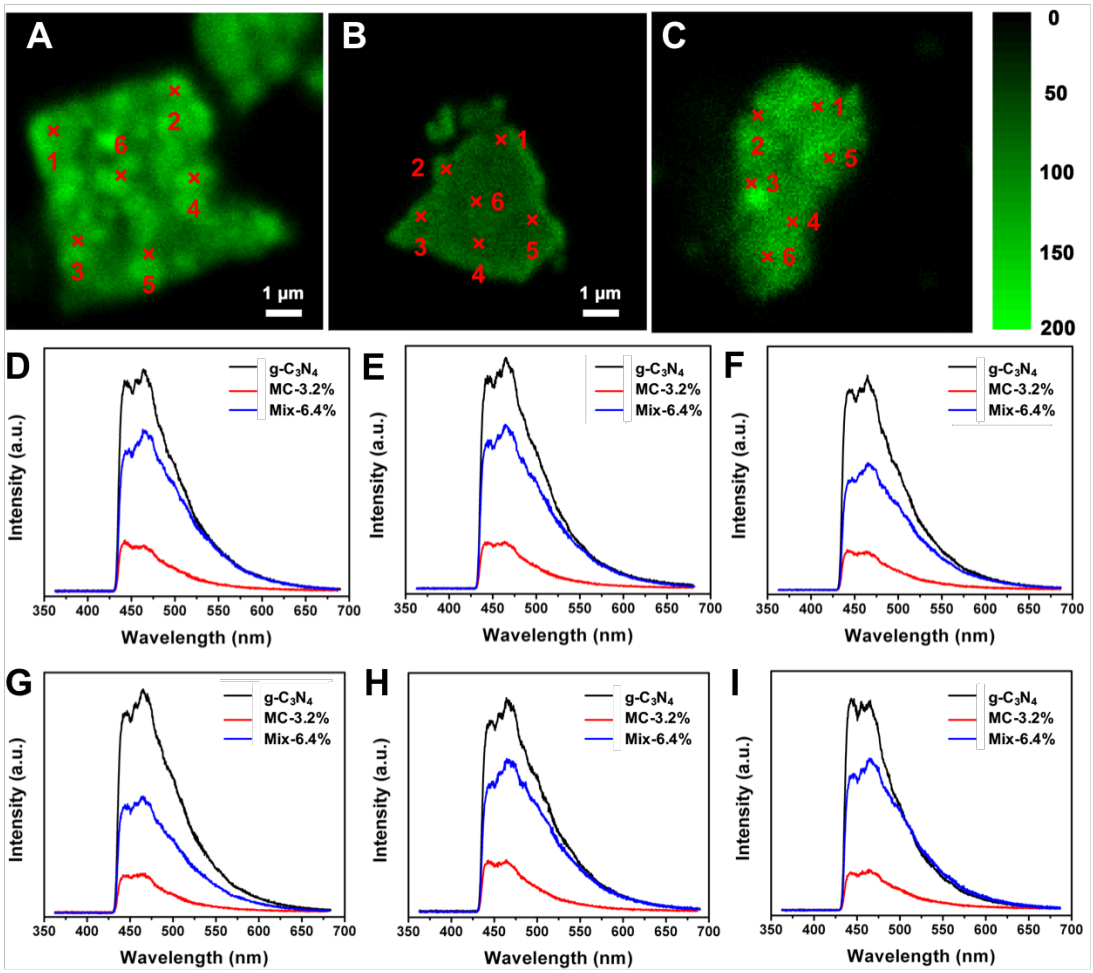

Figure 9 Single particle PL images of g-C_3N_4 (A), MC-3.2% (B), and Mix-6.4% (C). (D-I) Emission spectra observed at point 1 from A-C.

Apart from the emission spectra, time-resolved emission decay was also measured and fitted as shown in Figure 10. Theoretically, the short lifetime component is ascribed to surface-related nonradiative recombination processes (the trapping of electrons to defects), and the long lifetime component is attributed to the recombination of free excitons in g-C_3N_4. Therefore, we conclude that nonradiative recombination is the more dominant decay pathway in g-C_3N_4 and MoS_2 loading substantially suppressed the radiative charge recombination in g-C_3N_4 according to the fitting results. This kind of quenching phenomenon clear shows the effective trapping of photogenerated electrons by MoS_2 and indicates more efficient electron injection from g-C_3N_4 to MoS_2 nanodots. Therefore, MoS_2 loading substantially suppresses the radiative charge recombination in g-C_3N_4.

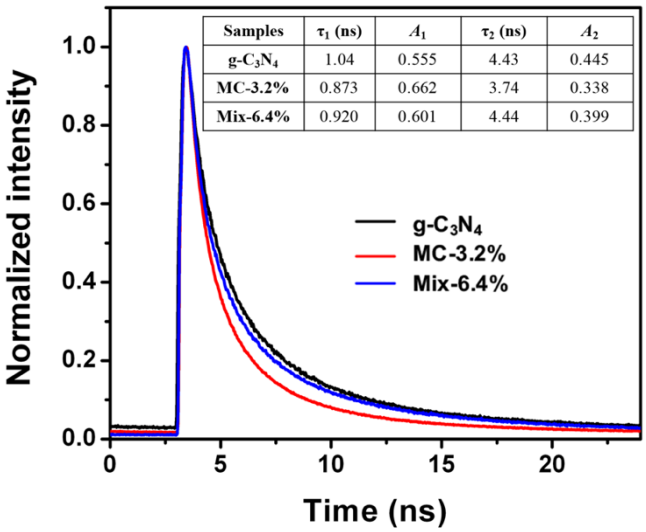

Figure 10 Typical emission decay profiles observed at g-C_3N_4, MC-3.2%, and Mix-6.4%, respectively. The fitted time constants and respective weighting factors are compiled in the inset table.

Based on the above results and analysis, we conclude that photogenerated electrons in g-C_3N_4 could transfer to MoS_2 nanodots easier, faster, and more efficient than to MoS_2 monolayer under visible light irradiation. However, the time scale of electron transfer dynamics, rate, and efficiency of carrier injection from g-C_3N_4 to MoS_2 are still unclear, which are significant and main influence factors of photocatalytic H_2 production activity. Therefore, time-resolved diffuse reflectance (TDR) spectroscopy was employed here to directly observe the kinetics of electron transfer and carrier populations after bandgap excitation. TDR spectra of all samples were recorded at different time delays after the excitation of samples by 400-nm laser pulse. The spectra of all samples revealed a positive absorption feature in the wavelength range from 800 to 1200 nm (Figure 11A-C), assigned to trapped and free (or shallowly trapped) photogenerated electrons in g-C_3N_4, respectively, according to the previous studies.[20,27] Transient absorption intensity of all samples reached highest immediately after laser flash (within ~ 2 ps) and then decayed gradually. At 60 ps after excitation, the absorbance intensity at 950 nm of the hybrids with MoS_2 nanodot and monolayer showed 36.6% and 29.5% decrease, respectively, which was significantly enhanced when compared with pure g-C_3N_4 (18.0%). This faster intensity decrease observed with MC-3.2% and Mix-6.4% indicats the accelerated electron decay kinetics.

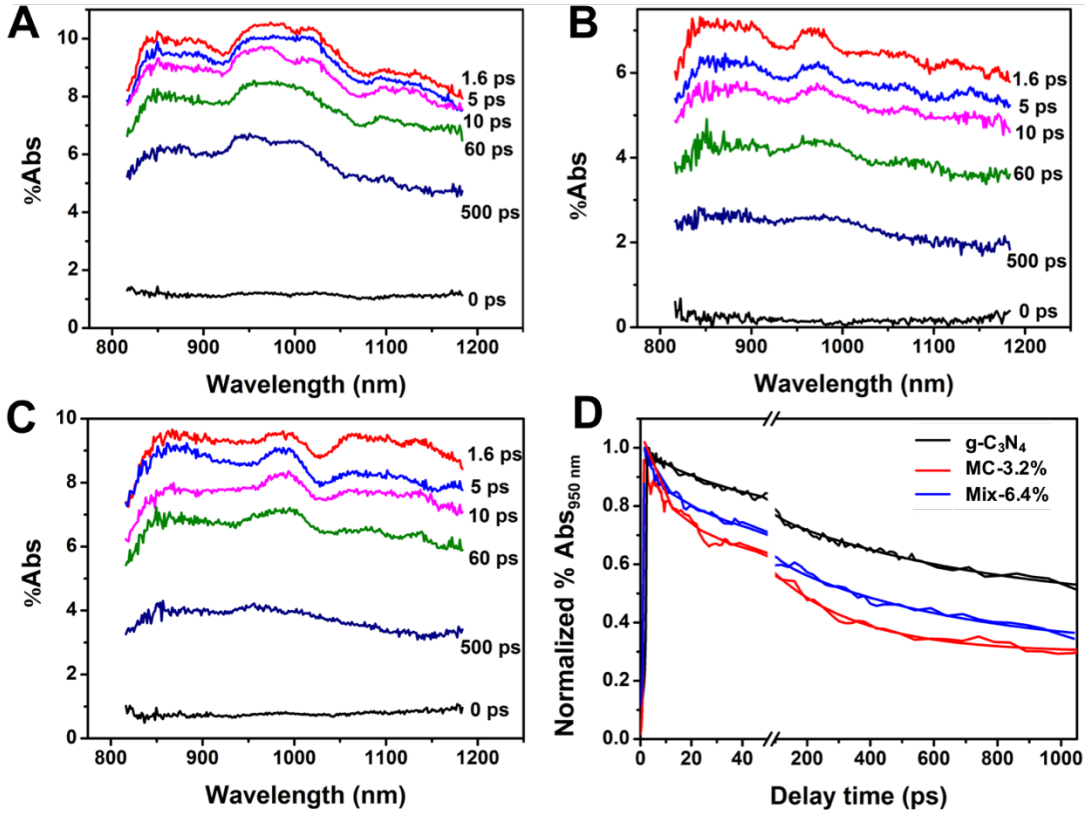

Figure 11 Time-resolved diffuse reflectance spectra of g-C_3N_4 (A), MC-3.2% (B), and Mix-6.4% (C). (D) Time profiles of normalized transient absorption at 950 nm for g-C_3N_4, MC-3.2%, and Mix-6.4% after 400-nm laser pulse irradiation.

Representative decay traces transient absorption at 950 nm are illustrated in Figure 11D and were fitted by a multiexponential function: $\Delta A = \Delta A_0 + \sum_i A_i e^{\left(-\frac{t}{\tau_i}\right)}$, where A and τ refer the amplitudes and lifetimes, respectively.[41] The smallest number of decay lifetimes, τ_i, which resulted in the minimum χ^2, was used for each fit.[42] Kinetic parameters for these three samples are listed in Table 1. For pure g-C_3N_4, a biexponential decay function was used and time constants were evaluated to be τ_1 = 36.5 ± 2.6 ps and τ_2 = 687 ± 86 ps, which corresponded to electron trapping at defect states and the charge carries recombination process, respectively.[20] In contrast, the decay curves of g-C_3N_4/MoS_2 hybrids were fitted by a triexponential function, suggesting that an additional electron decay process exists. This extra decay time was extremely short (τ_1=1.7 – 4.0 ps), attributing to the interfacial electron transfter between g-C_3N_4 and MoS_2.[43] The time constant of several tens picoseconds (τ_2 =28.8 - 40.5 ps) corresponds to the electrons injection from g-C_3N_4 into MoS_2 with a long distance or the trapped electrons at defect sites of g-C_3N_4.[10,27] The further long-lived component,

τ_3, is attributed to the slow recombination of electron-hole pairs.[44] The average lifetime, τ_{ave}, was also calculated according to the equation: $<\tau_{ave}> = \frac{\sum_i A_i \tau_i}{\sum_i A_i}$.[45] The average lifetimes of g-C_3N_4/MoS_2 hybrids were 122 ps (MC-3.2%) and 293 ps (Mix-6.4%) which was shorter than that of g-C_3N_4 (459 ps). In common, the shorter the average lifetime means more rapid the interfacial electron transfer.[44] Therefore, this calculated result clearly demonstrated that the electron is injected from g-C_3N_4 to MoS_2 nanodots within a shorter time scale.

Table 1 Exponential curve fitted parameters of transient absorption decay for g-C_3N_4, MC-3.2%, and Mix-6.4%.

Sample	A_1	A_2	A_3	τ_1 (ps)	τ_2 (ps)	τ_3 (ps)	τ_{ave} (ps)	k_{ET} (10^9 s^{-1})	η_{inj} (%)	χ^2
g-C_3N_4	0.454	0.351	-	36.5 ± 2.60	687 ± 86.2	-	459	-	-	0.994
MC-3.2%	0.307	0.196	0.395	1.70 ± 0.70	22.8 ± 5.90	273 ± 32.8	122	5.96	73.3	0.991
Mix-6.4%	0.144	0.241	0.360	4.00 ± 0.90	40.5 ± 6.50	578 ± 111	293	1.23	36.1	0.996

From the average lifetimes of g-C_3N_4, MC-3.2%, and Mix-6.4%, we determined the injection rate using the formula: $k_{\mathrm{ET}} = \frac{1}{\tau_{\mathrm{ave}(\mathrm{g-C_3N_4/MoS_2})}} - \frac{1}{\tau_{\mathrm{ave}(\mathrm{g-C_3N_4})}}$.[24] We found that the k_{ET} of Mix-6.4% is 1.23×10^9 s^{-1}, while 5.96×10^9 s^{-1} for MC-3.2%, which is 4.8 times faster. In addition, as a more important prameter for photocatalytic activity, the efficiency of electron injection (η_{inj}) into MoS_2 (nanodot or monolayer) was acquired as $\eta_{\mathrm{inj}} = 1 - \frac{\tau_{\mathrm{ave}(\mathrm{g-C_3N_4/MoS_2})}}{\tau_{\mathrm{ave}(\mathrm{g-C_3N_4})}}$.[24] Consistent with injection rate, MC-3.2% sample showed a higher injection efficiency (73.3%) than Mix-6.4% (36.1%). Considering that the loading amount of MoS_2 in MC-3.2% is much lower than that in Mix-6.4%, this result offered more straightforward and powerful evidence for the more efficient transportation of photogenerated electrons between g-C_3N_4 and MoS_2 nanodots. The efficient electrons injection greatly increased their opportunities to take part into the photocatalysis H_2 evolution reaction before electron-hole pairs recombination. All of photoelectrochemical, single-particle fluorescence, and

femtosecond time-resolved transient absorption results indicated a faster electrons injection rate and higher electrons injection efficiency in MC-3.2% arising from the stronger interaction between g-C_3N_4 and MoS_2 nanodots, which account for its significantly increased photocatalytic activity.

Apart from the electron injection from g-C_3N_4 to MoS_2, the amount of reactive sites in co-catalysts is another key point that influences photocatalytic H_2 evolution activity of semiconductors. In previous reports, the active sulfur atoms on the exposed edges of MoS_2 increase not only its electrocatalytic activity, but also photocatalytic activity.[46,47] These unsaturated active sulfur atoms could strongly bind with H^+ in solution, which are easily reduced to H_2 by electrons.[43] Because of the abundance of H^+ ions in lactic acid solution, unsaturated active sulfur atoms on the exposed edges of MoS_2 more easily capture H^+ ions, facilitating H_2 generation. Sulfur atoms on the basal plane with three-coordination, however, have no activity. In order to prove this, methanol and triethanolamine (TEOA) instead of lactic acid were also used as sacrificial reagents for H_2 production and the results are shown in Figure 12. It shows that H_2 production rate decreased a lot applying methanol and TEOA compared with lactic acid, indicating that adsorbing H^+ ions by unsaturated sulfur atoms plays a significant role when MoS_2 is served as co-catalyst. According to XPS results, the ratio of terminal S atom and basal S atom is increased from MoS_2 monolayer to nanodot, indicating more unsaturated S atoms as reaction sites.[31,47] Thereby, MoS_2 nanodot here exhibits a higher active for H_2 evolution as a co-catalyst because of the quantum-confinement effect.

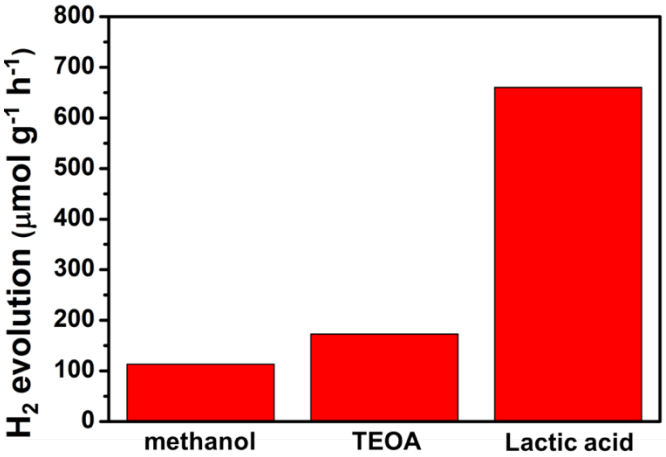

Figure 12 Comparison of photocatalytic H_2 evolution activities of MC-3.2% using different sacrificial reagents.

4. Conclusion

In summary, facile processes were developed to synthesize g-C_3N_4-based hybrid photocatalysts containing different structures of MoS_2 as co-catalyst, nanodot and monolayer. Photocatalytic H_2 evolution activity showed that the H_2 evolution rate of MC-3.2% is 660 μmol g^{-1} h^{-1} under visible light irradiation, which is 7.9 times higher than that of Mix-6.4% (83.8 μmol g^{-1} h^{-1}). Photoelectrochemistry and single-particle fluorescence spectra demonstrated that the recombination of photoexcited electron-hole pairs in MC-3.2% and Mix-6.4% samples was retarded due to the loading of MoS_2. Charge carrier dynamics of g-C_3N_4, MC-3.2%, and Mix-6.4% measured by femtosecond time-resolved diffused reflectance spectroscopy indicated that the electron injection rate was 5.96×10^9 s^{-1} in MC-3.2% compared to 1.23×10^9 s^{-1} in Mix-200 and the injection efficiencies were 73.3% and 36.1% in MC-3.2% and Mix-6.4%, respectively. These results indicated faster and more efficient electron transfer from g-C_3N_4 to MoS_2 nanodots, which might be attributed to the stronger interaction between them. In addition, the small size of MoS_2 nanodots contain more unsaturated active S atoms than MoS_2 monolayer, which could adsorb more H^+ ions. Therefore, this photodeposited g-C_3N_4/MoS_2-nanodot hybrid preformed great potential for photocatalytic H_2 production under visible light irradiation.

5. References

(1) Hou, Y. D.; Abrams, B. L.; Vesborg, P. C. K.; Bjorketun, M. E.; Herbst, K.; Bech, L.; Setti, A. M.; Damsgaard, C. D.; Pedersen, T.; Hansen, O.; Rossmeisl, J.; Dahl, S.; Norskov, J. K.; Chorkendorff, I. *Nat. Mater.* **2011**, 10, 434.

(2) Kongkanand, A.; Dominguez, R. M.; Kamat, P. V. *Nano Lett.* **2007**, 7, 676.

(3) Tang, J.; Kemp, K. W.; Hoogland, S.; Jeong, K. S.; Liu, H.; Levina, L.; Furukawa, M.; Wang, X.; Debnath, R.; Cha, D.; Chou, K. W.; Fischer, A.; Amassian, A.; Asbury, J. B.; Sargent, E. H. *Nat. Mater.* **2011**, 10, 765.

(4) Tong, H.; Ouyang, S. X.; Bi, Y. P.; Umezawa, N.; Oshikiri, M.; Ye, J. H. *Adv. Mater.* **2012**, 24, 229.

(5) Zhai, Q.; Xie, S.; Fan, W.; Zhang, Q.; Wang, Y.; Deng, W.; Wang, Y. *Angew. Chem. Int. Ed.* **2013**, 125, 5888.

(6) Iwase, A.; Yoshino, S.; Takayama, T.; Ng, Y. H.; Amal, R.; Kudo, A. *J. Am. Chem.*

Soc. **2016**, 238, 10260.
(7) Tian, N.; Zhang, Y.; Li, X.; Xiao, K.; Du, X.; Dong, F.; Waterhouse, G. I. N.; Zhang, T.; Huang, H. *Nano Energy* **2017**, 38, 72.
(8) Xiang, Q.; Yu, J.; Jaroniec, M. *J. Am. Chem. Soc.* **2012**, 134, 6575.
(9) Laursen, A. B.; Kegnas, S.; Dahl, S.; Chorkendorff, I. *Energy Environ. Sci.* **2012**, 5, 5577.
(10) Yin, X. L.; He, G. Y.; Sun, B.; Jiang, W. J.; Xue, D. J.; Xia, A. D.; Wan, L. J.; Hu, J. S. *Nano Energy* **2016**, 28, 319.
(11) Mak, K. F.; Lee, C.; Hone, J.; Shan, J.; Heinz, T. F. *Phys. Rev. Lett.* **2010**, 105, 36805.
(12) Eda, G.; Yamaguchi, H.; Voiry, D.; Fujita, T.; Chen, M. W.; Chhowalla, M. *Nano Lett.* **2011**, 11, 5111.
(13) Chia, X.; Eng, A. Y. S.; Ambrosi, A.; Tan, S. M.; Pumera, M. *Chem. Rev.* **2015**, 115, 11941.
(14) Liu, Q.; Fang, Q.; Chu, W.; Wan, Y.; Li, X.; Xu, W.; Habib, M.; Tao, S.; Zhou, Y.; Liu, D.; Xiang, T.; Khalil, A.; Wu, X.; Chhowalla, M.; Ajayan, P. M.; Song, L. *Chem. Mater.* **2017**, 29, 4738.
(15) Zhao, H.; Dong, Y.; Jiang, P.; Miao, H.; Wang, G.; Zhang, J. *J. Mater. Chem. A* **2015**, 3, 7375.
(16) Hong, X.; Kim, J.; Shi, S. F.; Zhang, Y.; Jin, C.; Sun, Y.; Tongay, S.; Wu, J.; Zhang, Y.; Wang, F. *Nat. Nanotechnol.* **2014**, 9, 682.
(17) Lou, Z.; Kim, S.; Zhang, P.; Shi, X.; Fujitsuka, M.; Majima, T. *ACS Nano* **2017**, 11, 968.
(18) Tachikawa, T.; Majima, T. *Chem. Soc. Rev.* **2010**, 39, 4802.
(19) Zheng, Z.; Majima, T. *Angew. Chem. Int. Ed.* **2016**, 55, 2879.
(20) Godin, R.; Wang, Y.; Zwijnenburg, M. A.; Tang, J. Durrant, J. R. *J. Am. Chem. Soc.* **2017**, 139, 5216.
(21) Kim, W. D.; Kim, J. H.; Lee, S.; Lee, S.; Woo, J. Y.; Lee, K.; Chae, W. S.; Jeong, S.; Bae, W. K.; McGuire, J. A.; Moon, J. H.; Jeong, M. S.; Lee, D. C. *Chem. Mater.* **2016**, 28, 962.
(22) Pesci, F. M.; Cowan, A. J.; Alexander, B. D.; Durrant, J. R. *J. Phys. Chem. Lett.* **2011**, 2, 1900.
(23) Ma, Y.; Pendlebury, S. R.; Reynal, A.; Formal, F. L.; Durrant, J. R. *Chem. Sci.* **2014**, 5, 2964.
(24) Abdellah, M.; Zidek, K.; Zheng, K.; Chabera, P.; Messing, M. E.; Pullerits, T. *J. Phys. Chem. Lett.* **2013**, 4, 1760.
(25) Chang, K.; Li, M.; Wang, T.; Ouyang, S. X.; Li, P.; Liu, L. Q.; Ye, J. H. *Adv. Energy Mater.* **2015**, 5, 1402279.
(26) Zeng, Z. Y.; Huang, Z. Y. Y, X.; Li, H.; He, Q. Y.; Lu, G.; Boey, F.; Zhang, H.

Angew. Chem. Int. Ed. **2011**, 50, 11093.
(27) Shi, X. W.; Fujitsuka, M.; Lou, Z. Z.; Zhang, P.; Majima, T. *J. Mater. Chem. A* **2017**, 5, 9671.
(28) Niu, P.; Zhang, L. L.; Liu, G.; Cheng, H. M. *Adv. Funct. Mater.* **2012**, 22, 4763.
(29) Li, C.; Wang, S.; Wang, T.; Wei, Y.; Zhang, P.; Gong, J. Small **2014**, *10*, 2783.
(30) Zhang, G.; Zhang, J.; Zhang, M.; Wang, X. *J. Mater. Chem.* **2012**, 22, 8083.
(31) Fu, X.; Zhang, L.; Liu, L.; Li, H.; Meng, S.; Ye, X.; Chen, S. *J. Mater. Chem. A* **2017**, 5, 15287.
(32) Zhou, W. J.; Yin, Z. Y.; Du, Y. P.; Huang, X.; Zeng, Z. Y.; Fan, Z. X.; Liu, H.; Wang, J. Y.; Zhang, H. *Small* **2013**, 9, 140.
(33) Li, Y. X.; Wang, H.; Peng, S. Q. *J. Phys. Chem. C* **2015**, 119, 27234.
(34) Meng, C. H.; Liu, Z. Y.; Zhang, T. R.; Zhai, J. *Green Chem.* **2015**, 17, 2764.
(35) Zhai, C. Y.; Zhu, M. S.; Bin, D.; Ren, F. F.; Wang, C. Q.; Yang, P.; Du, Y. K. *J. Power Sources* **2015**, 275, 483.
(36) Tang, M. L.; Grauer, D. C.; Lassalle-Kaiser, B.; Yachandra, V. K.; Amirav, L.; Long, J. R.; Yano, J.; Alivisatos, A. P. *Angew. Chem. Int. Ed.* **2011,** 123 (43), 10385.
(37) Chang, Y.-H.; Lin, C.-T.; Chen, T.-Y.; Hsu, C.-L.; Lee, Y.-H.; Zhang, W.; Wei, K.-H.; Li, L.-J. *Adv. Mater.* **2013,** 25 (5), 756.
(38) Yu, H.; Xiao, P.; Wang, P.; Yu, J. *Appl. Catal. B: Environ.* **2016,** 193, 217.
(39) Yang, M. Q.; Han, C.; Xu, Y. J. *J. Phys. Chem. C* **2015**, 119, 27234.
(40) Bian, Z.; Tachikawa, T.; Kim, W.; Choi, W.; Majima, T. *J. Phys. Chem. C* **2012**, 116, 25444.
(41) Grigioni, I.; Stamplecoskie, K. G.; Selli, E.; Kamat, P. V. *J. Phys. Chem. C* **2015**, 119, 20792.
(42) Milleville, C. C.; Pelcher, K. E.; Sfeir, M. Y.; Banerjee, S.; Watson, D. F. *J. Phys. Chem. C* **2016**, 120, 5221.
(43) Zhang, P.; Tachikawa, T.; Fujitsuka, M.; Majima, T. *Chem. Commun.* **2015**, 51, 7187.
(44) Zhukovskyi, M.; Tongying, P.; Yashan, H.; Wang, Y. X.; Kuno, M. *ACS Catal.* **2015**, 5, 6615.
(45) Ong, W. J.; Putri, L. K.; Tan, Y. C.; Tan, L. L.; Li, N.; Ng, Y. H.; Wen, X.; Chai, S. P. *Nano Res.* **2017**, 10, 1673.
(46) Yu, X. Y.; Hu, H.; Wang, Y.; Chen, H.; Lou, X. W. *Angew. Chem. Int. Ed.* **2015**, 54, 7395.
(47) Chang, K.; Mei, Z. W.; Wang, T.; Kang, Q.; Ouyang, S. X.; Ye, J. H. *ACS Nano* **2014**, 8, 7078.

Part 3-2. Electron Transfer Dynamics of Quaternary Sulfur Semiconductor/MoS_2 Layer-on-Layer for Efficient Visible-Light H_2 Evolution

1. Introduction

Due to the massive combustion of fossil fuel, the shortage of fossil resources and increased environment crisis begin to restrain further development of the society. Conversion of water to H_2 utilizing solar energy by photocatalysts is of great potential, which not only supplies green energy source for industrial but also shrinks the generation of contaminative gases thus attracting enormous research interests recently.[1,2] Since the visible light covers 42-43% of the solar light, most attentions are now focused on the synthesis of efficient visible-light driven photocatalysts.[3-7] In recent years, quaternary oxide (or sulfide) semiconductors have become promising candidates for photocatalysis reactions owing to their tunable band gap and considerable chemical stabilities.[8-10] However, this kind of quaternary sulfide semiconductors have been seldom used as solar-driven photocatalysts for H_2 evolution.

Similar to the ternary sulfide semiconductors, quaternary sulfide photocatalysts may also suffer the shortcomings for H_2 evolution, such as fast recombination of photogenerated electron-hole pairs and shortage of active sites.[11,12] Recently, two-dimensional MoS_2 nanosheet, composed of three stacked atom layers (S-Mo-S) held together by van der Waals forces, has been extensively studied and attracted much attentions toward H_2 evolution.[13-16] The calculation indicated that MoS_2 had a free energy close to zero when it was worked as the catalyst for H_2 evolution, which is almost the same as the case of Pt.[17] In addition, due to the unsaturated sulfur atoms on exposed edges could serve as active sites for photocatalysis reaction, MoS_2 is believed to be a promising and low-cost candidate co-catalyst instead of Pt.[17]

Femtosecond time-resolved transient absorption (fs-TAS) has been widely used to deeply investigate the migration and recombination dynamics of photogenerated charge carrier within picosecond time scale, and is employed here to help us explore the

fundamental reasons for the enhancement of photocatalytic activity.[18-20] It has been reported that the conduction band (CB) level of the quaternary sulfur semiconductors are tunable by changing the amount of new introducing element.[8] As is well known, the photoreduction ability of a semiconductor is closely related with its CB position, and a higher CB level provides a larger reduction diving force.[21] Further functionalization of the quaternary sulfur semiconductor with MoS_2 greatly enhances the charge separation efficiency and thus improves its photocatalytic activity.

Herein, we report a photocatalytic H_2 evolution by $ZnIn_2S_4$-based quaternary sulfur semiconductor, $Zn_{0.4}Ca_{0.6}In_2S_4$ (ZCIS) microspheres composed of cross-linked nanosheets, combined with MoS_2 by hydrothermal process. Layer structured MoS_2 were mostly deposited on the surface of ZCIS nanosheets to form a 2D-2D structure. As expected, the photocatalytic activity of ZCIS was greatly enhanced under visible light irradiation after loading MoS_2 compared with the bare one. According to the results of photoelectrochemical spectroscopy and fs-TAS, charge separation and electron injection dynamics, injection rate, and injection efficiency of the photocatalysts were explored. Proper mechanisms were proposed to account for the improved photocatalytic H_2 evolution activity of various photocatalytic materials. The present results may inspire the exploration of low-cost efficient photocatalysts for water splitting.

2. Experimental Section

***Preparation of* ZCIS and ZM-*X*.** ZCIS was prepared by a hydrothermal process according to previous work.[8] $ZnCl_2$ (27 mg), $Ca(NO_3)_2{\cdot}4H_2O$ (71 mg), $InCl_3{\cdot}4H_2O$ (293 mg), and thioacetamide (TAA 150 mg) were dissolved in 25 mL deionized water and 5 mL of glycol. After stirring for about 30 min at room temperature, the resulting heterogeneous solution was transferred into a 50 mL Teflon-lined stainless steel autoclave and maintained at 120 °C for 12 h in an oven. The products were collected by centrifugation and dried at 60 °C oven. For synthesis of ZM-*X* (*X* = 0.6, 1.8, 3.0, 4.2, and 6.0, representing the weight percentage of MoS_2), different amount of $(NH_4)_2MoS_4$ and 100 mg ZCIS were added to 12.5 mL DMF and then stirred for 30 min under room

temperature. Then the homogeneous solution was transferred to a 50 mL Teflon-lined autoclave and maintained at 200 °C for 10 h. The products were collected by centrifugation and dried. Pure MoS_2 was synthesized without adding ZCIS.

Photocatalytic H_2 evolution. 3 mg sample were dispersed in 5 mL aqueous solution containing 20 vol% lactic acid for H_2 evolution. Prior to the irradiation, the catalyst was dispersed using an ultrasonic bath, and then bubbled with argon through the reactor for 30 min to completely remove the dissolved oxygen and ensure the reactor was in an anaerobic condition. The samples were irradiated at different wavelengths using a Xenon lamp for H_2 evolution (Asahi Spectra, HAL-320; 300 mW cm^{-2}). The reaction temperature was kept at about 293 K. The visible light was filtered with a nominal 420 nm cutoff filter. The volume of H_2 was measured by using a Shimadzu GC-8A gas chromatograph equipped with an MS-5A column and a thermal conductivity detector. The catalytic stability was evaluated by isolating, washing and reusing the catalyst in a cycling experiment. The apparent quantum efficiency (AQE) was calculated using the following equation,[22]

$$\text{AQE}\ (\%) = \frac{\text{Number of evolved H}_2\text{ molecules} \times 2}{\text{Number of incident photons}} \times 100\%.$$

Photoelectrochemical measurements. Electrochemical and photoelectrochemical measurements were performed in a three-electrode quartz cell. A Platinum wire was used as the counter electrode, and an Ag/AgCl electrode was used as the reference electrodes. For loading sample on a glassy carbon electrode, 4 mg sample was added into solution containing H_2O and CH_3CH_2OH with volume ratio of 1:1. Then 50 μL Nafion was added into the solution. After ultrasonic for 10 min, 3 μL solution was took out and drop on the surface of glassy carbon. The electrode was used for photoelectrochemical measurements after drying. 0.1 M Na_2SO_4 aqueous solution was used as the electrolyte. Electrochemical impedance spectroscopy (EIS) was carried out under visible light irradiation. A Xenon lamp was utilized as the light source in the photoelectrochemical measurements with the intensity of 300 mW cm^{-2} and the visible light was filtered with nominal 420 nm cutoff filter. The potential (*vs.* Ag/AgCl) was converted to the reversible hydrogen electrode (RHE) according to the Nernst equation:

$E_{RHE} = E + 0.05916pH + E_0$,

where E_{RHE} is the potential *vs.* RHE, E_0= 0.1976 V at 25°C, and E is the measured potential *vs.* Ag/AgCl.

Time-resolved diffuse reflectance measurements. The femtosecond diffuse reflectance spectra were measured by the pump and probe method using a regeneratively amplified titanium sapphire laser (Spectra-Physics, Spitfire Pro F, 1kHz) pumped by a Nd:YLF laser (Spectra-Physics, Empower 15). The output of an optical parametric amplifier (420 nm, 4 μJ pulse^{-1}) was used as the excitation pulse. A white light continuum pulse, which was generated by focusing the residual of the fundamental light on a sapphire crystal, was directed to the sample powder coated on the glass substrate, and the reflected lights were detected by a linear InGaAs array detector equipped with the polychromator (Solar, MS3504). All measurements were carried out at room temperature.

Characterization of materials. The samples were characterized using X-ray diffraction (XRD, Rigaku Rint-2500, CuKα source), and HRTEM (JEOL JEM 3000F, operated at 300kV). The steady-state UV-visible absorption and diffuse reflectance spectra were measured by UV-visible-NIR spectrophotometers (Shimadzu UV-3100 and Jasco V-570) at room temperature. XPS measurements were performed with a PHI X-tool 8ULVAC-PHI.

3. Results and Discussion

Crystal structure of the synthesized samples was first examined by X-ray diffraction (XRD). The patterns shown in Figure 1 demonstrate that the main peaks located at 21.2, 27.3, 30.5, 47.0, 52.2, 55.4, and 75.9° are consistent with previous reports, indicating the successful synthesis of $Zn_{0.4}Ca_{0.6}In_2S_4$ (ZCIS).[8] No other characteristic peaks are found, evidencing the high purity of ZCIS. Because of small loading amount, the peaks of MoS_2 could not be observed in ZM-*X* samples.

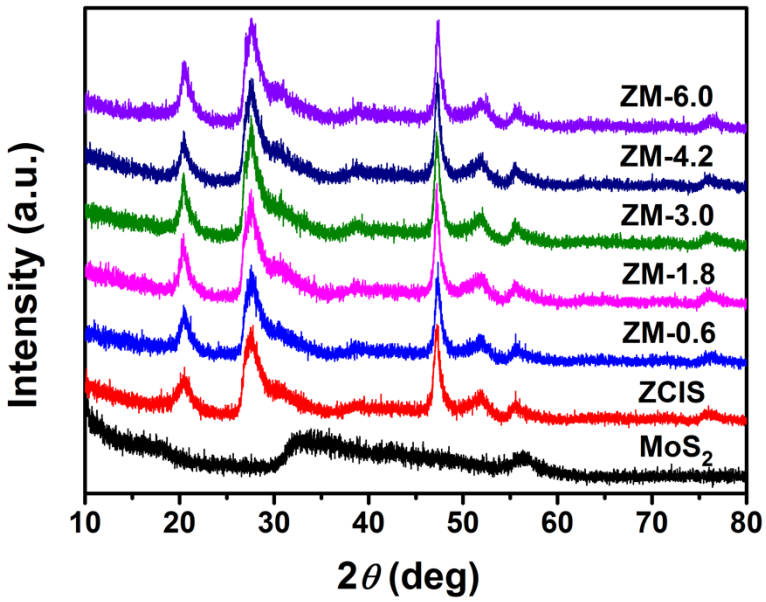

Figure 1 XRD patterns of MoS_2, ZCIS, and ZM-*X*.

In addition, HRTEM and elemental mapping were further used to prove the formation of ZCIS (Figure 2). As revealed by HRTEM images, ZCIS exhibits a flower-like microsphere morphology made up by cross-linked nanosheets and the lattice fringe with intervals of 0.330 nm is assigned to (110) plane. Elemental mapping suggests that Zn, Ca, In, and S elements have a highly homogeneous distribution throughout ZCIS microsphere.

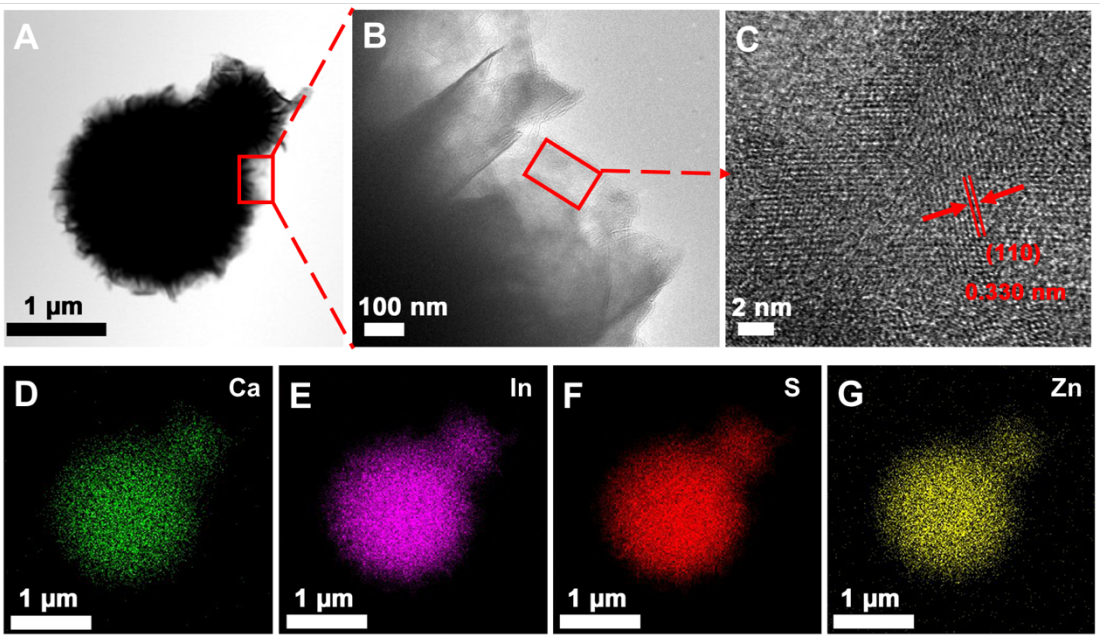

Figure 2 HRTEM images of ZCIS (A-C) and elemental mapping of Ca (D), In (E), S (F), and Zn (G) of ZCIS.

The morphology and structure of as-prepared samples were characterized by SEM and HRTEM. SEM image of ZCIS in Figure 3A shows the homogeneously distributed microsphere morphology with the size in the range of 4-8 μm. ZM-*X* samples still kept a microsphere morphology after hydrothermal treatment for synthesizing MoS_2 and size was similar to pure ZCIS after loading MoS_2. It is clearly shown that no MoS_2 could be observed due to the limited loading amount of MoS_2 (less than 3.0 wt%). MoS_2 aggregated nanoflowers start to appear, however, if further increasing the amount, as shown in the red circles in Figures 3E and F, which is similar to pure MoS_2 without adding ZCIS precursors.

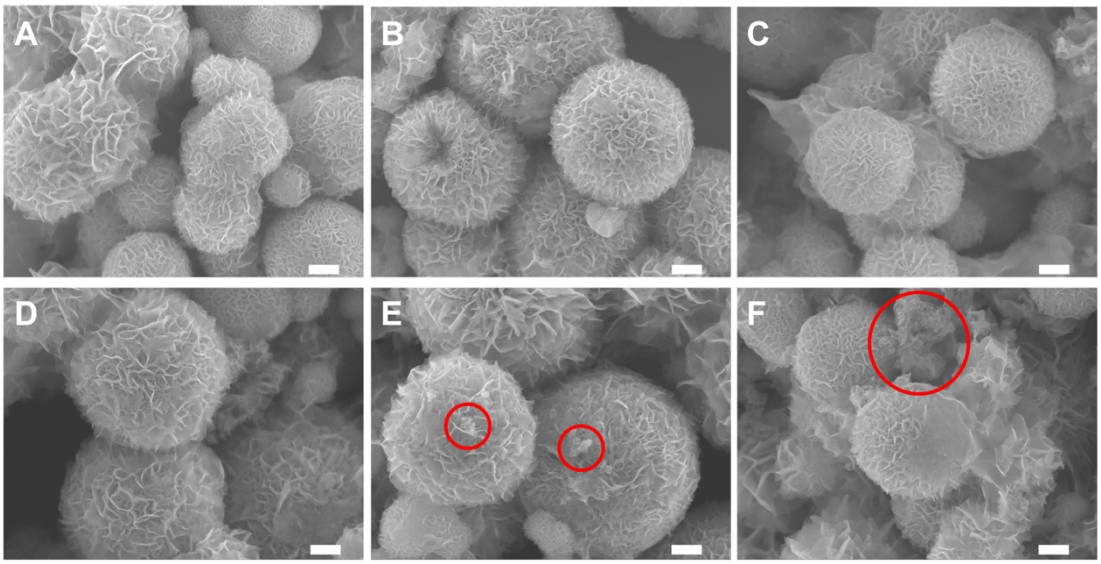

Figure 3 SEM image of pure ZCIS (A), ZM-0.6 (B), ZM-1.8 (C), ZM-3.0 (D), ZM-4.2 (E), and ZM-6.0 (F). The scale bar is 1 μm.

HRTEM image in Figure 4 presents detailed crystal information of ZM-3.0. The lattice fringes with a distance of 0.330 nm corresponds to the (110) plane of ZCIS, implying a preserved crystal structure after second hydrothermal process. Short-range lattice fringes with distance of 0.62 nm are also observed, which is consistent with the d-spacing of (002) planes of MoS_2.[13] Therefore, it is confirmed that ZCIS and MoS_2 closely contact with each other to form a 2D-2D interface which favors the transportation of photogenerated charges.

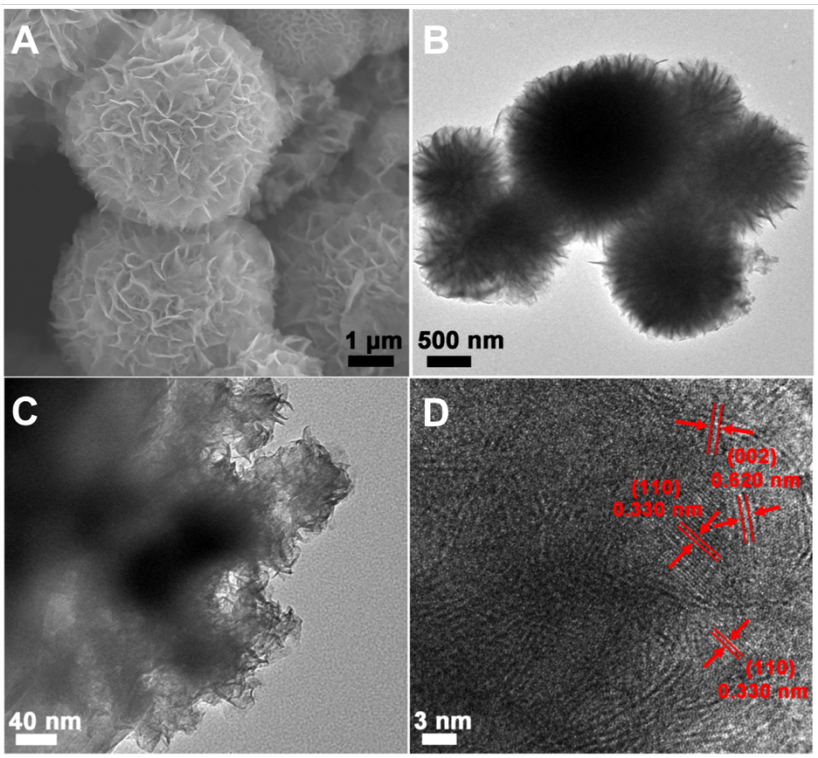

Figure 4 SEM image (A), TEM images (B-C), and HRTEM image (D) of ZM-3.0.

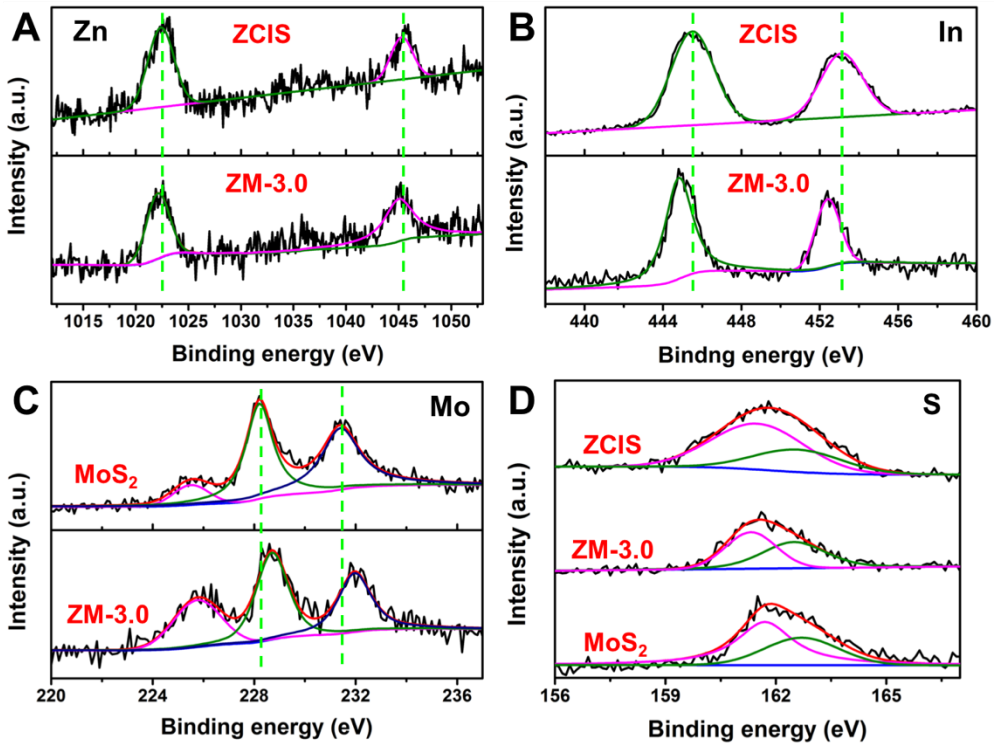

Figure 5 XPS spectra of Zn 2p (A), In 3d (B), Mo 3d (C), and S 2p (D) in ZCIS, ZM-3.0, and pure MoS_2.

XPS measurements were carried out in order to identify the compositions and surface chemical states of representative elements in ZCIS and ZM-*X*. Two peaks at 1045.3 and

1022.4 eV in Zn 2p high resolution XPS spectrum for ZCIS (Figure 5A) correspond to to Zn^{2+} $2p_{1/2}$ and $2p_{3/2}$, respectively. In the XPS spectrum for In 3d of ZCIS (Figure 5B), peaks at 453.1 and 445.5 eV are assigned to In $3d_{3/2}$ and In $3d_{5/2}$, respectively. Interestingly, the peak positions of Zn 2p and In 3d in ZM-3.0 sample shift to lower binding energies by approximately 0.3 and 0.7 eV compared with pure ZCIS, respectively. Mo 3d XPS spectrum of ZM-3.0 shows two peaks centered at 228.7 and 232.0 eV (Figure 5C), assigning to Mo $3d_{5/2}$ and Mo $3d_{3/2}$, respectively, indicating that Mo is in the +4 valence state. In contrast with the peak shift of Zn 2p and In 3d, the peak positions of Mo 3d in ZM-3.0 move to higher binding energy (about 0.5 eV). This peak shift toward lower binding energy, suggesting a strong interaction between MoS_2 and ZCIS, is ascribed to the increase of electron concentration with enhanced electron screening effect caused by the formation of ZCIS/MoS_2 junction. The binding energies of S^{2-} $2p_{1/2}$ and $2p_{3/2}$ orbitals for ZCIS are 162.6 and 161.5 eV, and those for MoS_2 are 162.7 and 161.7 eV, respectively, which are in accordance with previous reported results.[8,22]

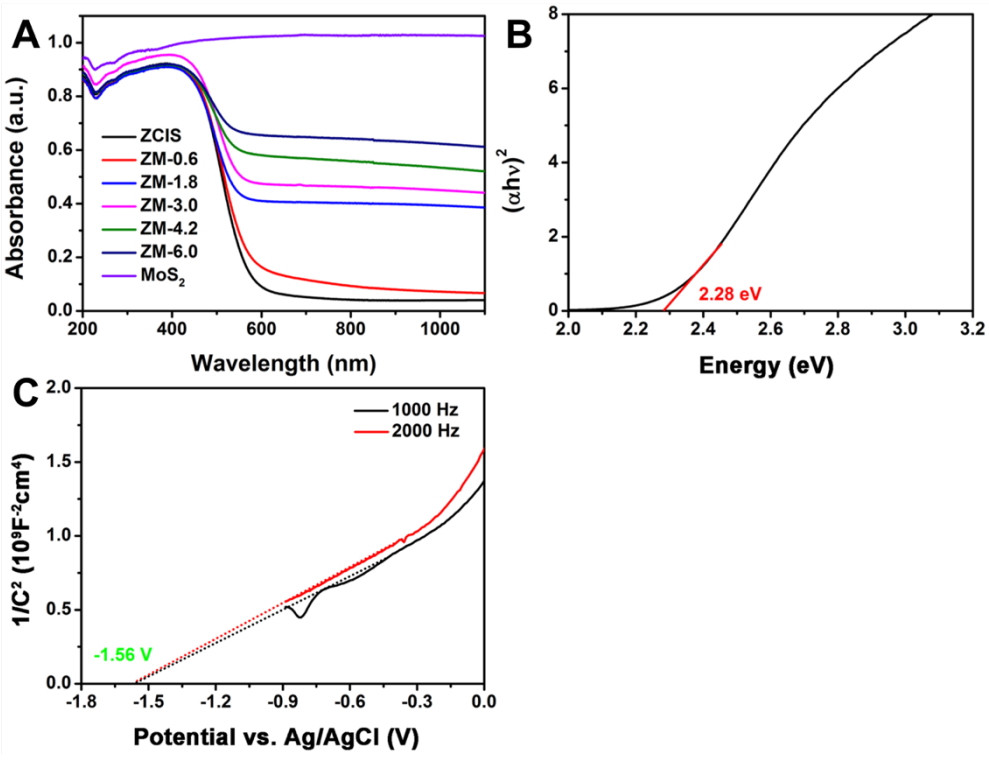

Figure 6 (A) Diffuse-reflectance spectroscopy of ZCIS, ZM-*X*, and MoS_2. (B) Optical band gap energy estimation of ZCIS. (C) Mott-Schottky (M-S) plots of ZCIS.

Optical absorption spectra of photocatalysts, playing a significant role for photocatalytic performance of semiconductors, were measured by diffuse reflection spectroscopy (DRS). DRS spectra for ZCIS and ZM-*X* depicted in Figure 6A exhibit photoresponse in visible region. The optical absorption in longer wavelength region has great change after combination with MoS_2, while MoS_2 affects little on the absorption edge of ZCIS. With increasing the loading amount of MoS_2, light absorption in the range of 600-1100 nm is gradually enhanced, probably due to the increased background absorption because of black colored MoS_2 nanosheets.[22,23] Particularly, all diffuse reflectance spectra show very steep change around 500-600 nm, indicating that the visible-light absorption is attributed to a band transition instead of the transition from impurity levels. The band gap energy of the sample was obtained according to the equation of $\alpha h\nu = A(\alpha h\nu - E_g)^n$, from solid solutions, where h, α, ν, A, and E_g represent Planck's constant, optical absorption coefficient, photon frequency, a constant, and photonic energy band gap, respectively.[24] The band gap of ZCIS is estimated to be 2.28 eV (Figure 6B). In addition, the band energy position of ZCIS was further determined. As shown in Figure 6C, the intersection point, corresponding to the flat-band potential E_{fb}, in the Mott-Schottky plots is independent of frequencies, and is calculated to be -1.56 V *vs.* Ag/AgCl, i.e., -1.36 V *vs.* normal hydrogen electrode (NHE). The positive slop of Mott-Schottky curve indicates that ZCIS is n-type semiconductors and its E_{fb} is about 0.1 V below the conduction band position (E_{CB}).[25] Therefore, the E_{CB} position of ZCIS is -1.46 V and its valence band position (E_{VB}) is determined to be 0.82 V.

Photocatalytic H_2 evolution performances of the as-prepared samples were examined under visible light irradiation ($\lambda \geq 420$ nm) with the lactic acid as sacrificial agent. Control experiments suggest that there is no appreciable H_2 generated in the absence of photocatalysts or light irradiation. Figure 7A shows the average H_2 evolution rate of ZCIS and ZM-*X* samples. Only a little amount of H_2 is formed from bare ZCIS (0.13 μmol h^{-1}), which is probably due to the fast recombination of photogenerated electron-hole pairs and lack of active sites for photocatalytic reaction. However, a large increase in H_2 evolution rate is observed after combining with MoS_2. The photocatalytic activity

of ZM-*X* is enhanced with the increasing amount of MoS_2 from 0.6 to 3.0 wt% and the ZM-3.0 sample exhibits the highest H_2 evolution rate (3.5 μmol h^{-1}), which is 27 times higher than that of ZCIS. Further increasing the amount of MoS_2 (ZM-4.2 and ZM-6.0) gives rise to slightly depressed activity but it is still superior to bare ZCIS. The apparent quantum efficiency (AQE) was also estimated to be 0.26% and 8.26% for ZCIS and ZM-3.0, respectively, under the wavelength of 420 ± 5 nm light irradiation.

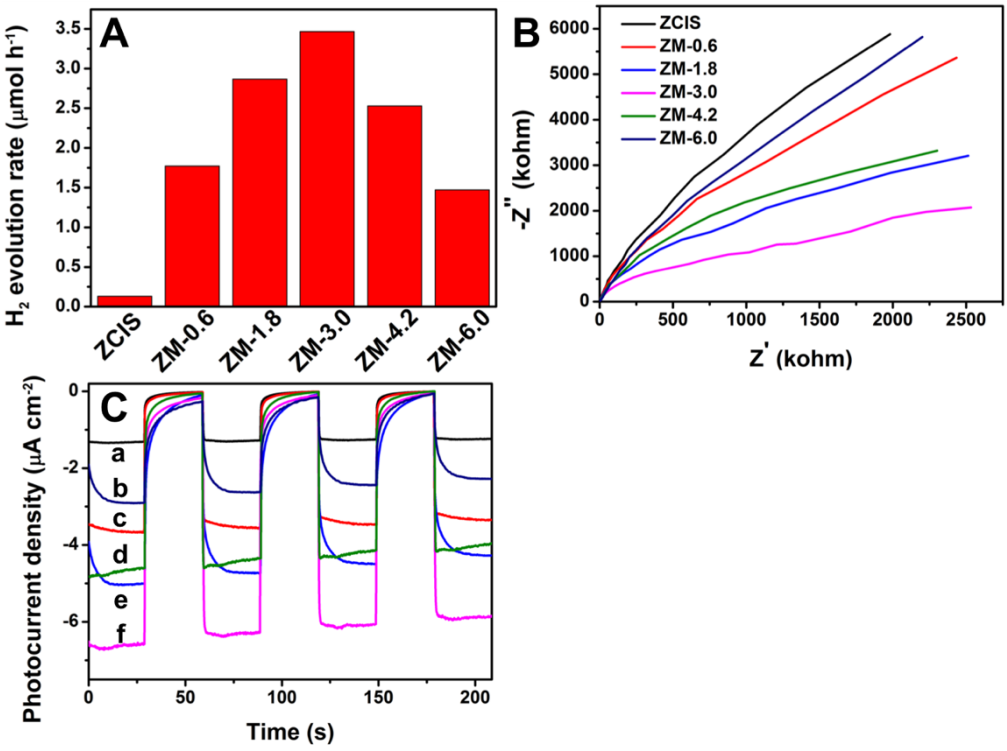

Figure 7 Comparison of photocatalytic H_2 evolution activities of ZCIS and ZM-*X* samples (A). Electrochemical impedance spectroscopy (EIS) Nyquist plots under visible light irradiation (B) and transient photocurrent density curves (C) for ZCIS (a), ZM-6.0 (b), ZM-0.6 (c), ZM-4.2 (d), ZM-1.8 (e), and ZM-3.0 (f) in 0.5 M Na_2SO_4 solution.

A series of photoelectrochemical studies were firstly measured in order to study the interfacial charge transfer properties between ZCIS and MoS_2. Electrochemical impedance spectroscopy (EIS) was used to investigate the electrical conductivity of the photocatalysts. In Figure 7B, ZM-3.0 presents a representative Nyquist plot with a much smaller arc radius than that of other samples, suggesting that the charge transfer resistance is remarkably decreased by introducing a certain amount of MoS_2.[26] Therefore, the photoinduced electron-hole pairs could separate more efficiently. This

conclusion is also supported by transient photocurrent (*I-t*) curves in Figure 7C, which shows a much enhanced photocurrent of ZM-3.0 over other samples. It is known that the photocurrent is mainly attributed to the diffusion of photogenerated electrons to the back contact and meanwhile the photogenerated holes are compenstated by hole acceptor in the electrolyte, the combination of ZCIS and MoS_2 is highly efficient in promoting charge transfer and separation, and thus leads to a better photocatalytic performance as ZM-3.0.[27]

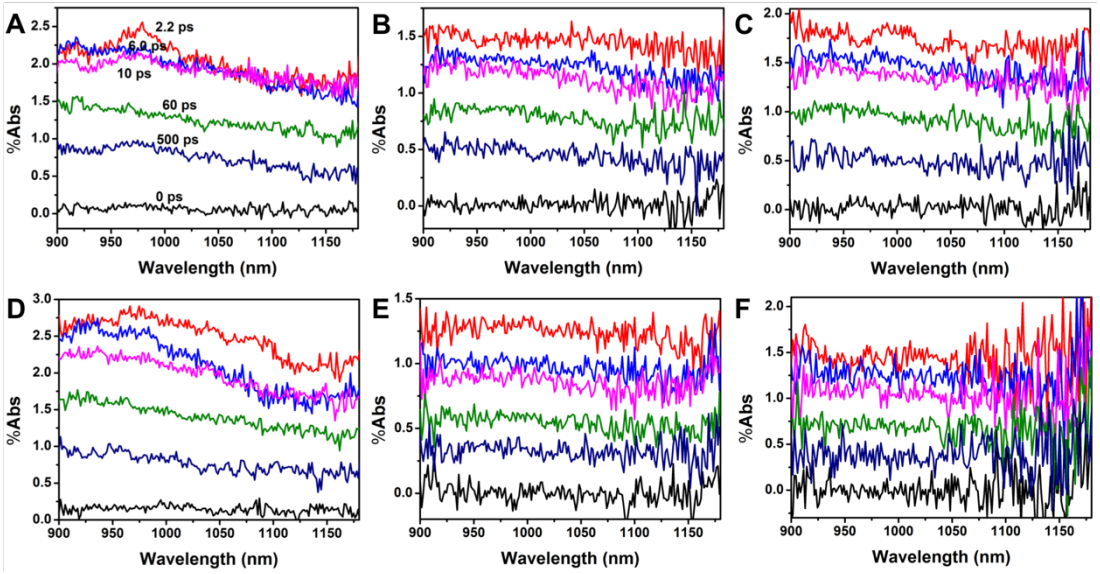

Figure 8 Time-resolved diffuse reflectance spectra of ZCIS (A), ZM-0.6 (B), ZM-1.8 (C), ZM-3.0 (D), ZM-4.2 (E), and ZM-6.0 (F).

Even though photoelectrochemistry results indicate that the electron transfer resistance is greatly reduced after introduction of MoS_2, it is still necessary to clarify the insight mechanisms and determine the time scale of electron transfer dynamics efficiency of carrier injection from ZCIS to MoS_2, which are significant and main factors for photocatalytic performance. Therefore, time-resolved diffuse reflectance (TDR) spectroscopy, a powerful analytical tool for studying ultrafast processes in photocatalysts under various conditions, was employed to directly observe the kinetics of electron migration after the bandgap excitation. TDR spectra of all photocatalysts were recorded at different time delays after the excitation of samples by 420-nm pulse laser. The spectra reveal a positive absorption feature in the wavelength range from 900 to 1180 nm (Figure 8), which are probably assigned to free and trapped (shallow and deep trapped) photogenerated electrons in ZCIS according to the previous studies.[28,29]

Transient absorption intensity of all samples reached highest immediately after laser flash (< 2 ps) and then gradually decayed. Compared with bare ZCIS, the absorption of ZM-*X* decayed much faster, and ZM-3.0 exhibited the fastest decay rate. At 10 ps after pulse laser excitation, the absorbance intensities at 975 nm of ZM-*X* (*X* = 0.6, 1.8, 3.0, 4.2, and 6.0) showed 22.2%, 26.5%, 29.7%, 27.0%, and 22.2% decrease, respectively, which were significantly enhanced compared with bare ZCIS (14.4%). And ZM-3.0 exhibited the fastest decreasing rate. This faster intensity decrease observed with ZM-*X* indicates the accelerated electron decay kinetics.

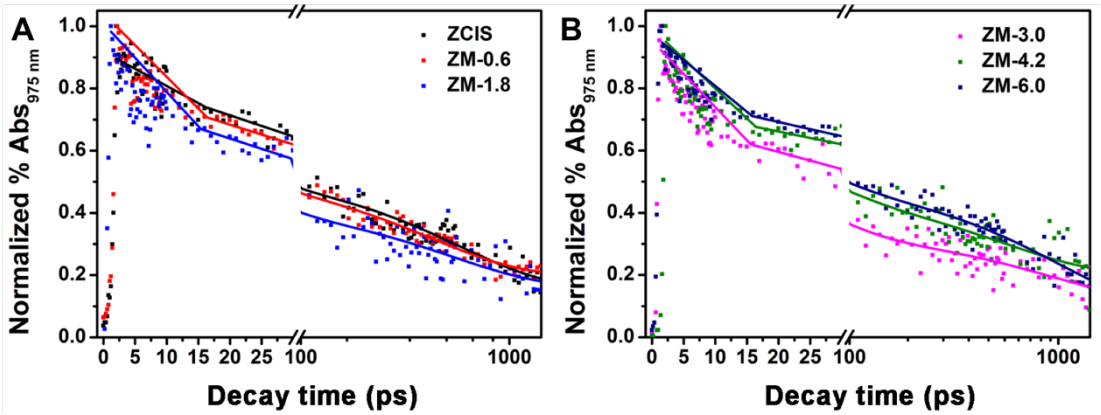

Figure 9 (A) Time profiles of normalized transient absorption at 975 nm for ZCIS, ZM-0.6, and ZM-1.8 after 420-nm laser irradiation. (B) Time profiles of normalized transient absorption at 975 nm for ZM-3.0, ZM-4.2, and ZM-6.0 after 420-nm laser irradiation.

Representative decay traces transient absorption at 975 nm are illustrated in Figure 9 and fitted by a multiexponential function: $\Delta A = \Delta A_0 + \sum_i A_i e^{\left(-\frac{t}{\tau_i}\right)}$, where A and τ refer the amplitudes and lifetimes, respectively.[30] The smallest number of decay lifetimes, τ_i resulted in the minimum χ^2, is used for each fit.[31] Kinetic parameters for these three samples are listed in Table 1. In the case of pure ZCIS, a biexponential decay function is used and the time constants are evaluated to be $\tau_1 = 28.0 \pm 3.4$ ps and $\tau_2 = 580 \pm 139$ ps, which are assigned to electron tapped at defect states and the charge carriers recombination process, respectively.[28,32,33] On the contrary, the decay curves of ZM-*X* samples are fitted by a triexponential function, demonstrating the existence of an additional deactivation path, i.e., electron transfer process. This extra route is extremely short, less than 5 ps, attributing to the interfacial electron transfer from ZCIS to MoS_2

and ZM-3.0 exhibites the fastest electron injection with only 1.12 ps among all ZM-*X* samples. According to the TEM image, hydrothermal formed MoS_2 are mostly deposited on the outside of ZCIS microsphere, therefore, the time constant of several tens picoseconds (τ_2 = 26.9 – 51.9 ps) may due to the electrons injection from ZCIS to MoS_2 with a long distance or the trapped electrons at defect sites of ZCIS. For the further long-lived component up to several hundred picoseconds, τ_3 is attributed to the slow recombination of photogenerated electron-hole pairs. Based on the fitting data, we calculated the mean lifetime of the sample according to the equation: $<\tau_{ave}> = \frac{\sum_i A_i \tau_i}{\sum_i A_i}$.[34] The average lifetime firstly exhibits a sharp decrease from 293 ps (ZCIS) to 87.8 ps (ZM-3.0), and then gradually increase to 178 ps (ZM-6.0). In common, the shorter mean lifetime indicates more rapid the interfacial electron separation. Therefore, this calculated results clearly show that the electrons are injected from ZCIS to MoS_2 within a much shorter time scale in ZM-3.0 than other ZM-*X* samples.

Table 1. Kinetic parameters of transient absorption decays.

Sample	A_1	A_2	A_3	τ_1 (ps)	τ_2 (ps)	τ_3 (ps)	τ_{ave} (ps)	η_{inj} (%)	χ^2
ZCIS	0.400 (52.0%)	0.369 (48.0%)	-	28.0 ± 3.40	580 ± 139	-	293	-	0.967
ZM-0.6	0.305 (33.4%)	0.388 (42.3%)	0.222 (24.3%)	3.76 ± 0.83	49.3 ± 14.5	555 ± 261	157	46.4	0.970
ZM-1.8	0.706 (53.3%)	0.354 (26.7%)	0.265 (20.0%)	1.25 ± 0.49	33.1 ± 5.50	533 ± 209	116	60.3	0.956
ZM-3.0	1.01 (59.6%)	0.361 (21.3%)	0.324 (19.1%)	1.12 ± 0.35	26.9 ± 3.30	426 ± 66.2	87.8	69.9	0.983
ZM-4.2	0.599 (52.1%)	0.313 (27.2%)	0.238 (20.7%)	2.86 ± 1.00	51.9 ± 9.00	523 ± 186	124	57.7	0.958
ZM-6.0	0.346 (26.0%)	0.573 (43.1%)	0.411 (30.9%)	4.82 ± 1.33	49.6 ± 10.7	503 ± 111	178	39.2	0.980

As a more significant parameter for photocatalytic performance, the efficiency of electron injection (η_{inj}) from ZCIS into MoS_2 was also acquired as $\eta_{inj} = 1 - \frac{\tau_{ave}(ZM-X)}{\tau_{ave}(ZCIS)}$.[35] ZM-3.0 also shows the highest injection efficiency (69.9%) than other samples. Considering the different loading amount of MoS_2 in ZM-*X*, this result offers more straightforward and powerful evidence that most efficient transportation of photogenerated electrons between ZCIS and MoS_2 happens in ZM-3.0 sample. The

electrons injection could greatly increase their opportunities to involve into the photocatalysis H_2 evolution before the recombination of electron-hole pairs. Therefore, the results of photoelectrochemical and femtosecond time-resolved transient absorption together indicate that the photogenerated electrons could migrate from ZCIS to MoS_2, thus to enhance the photocatalytic activity of ZCIS. More importantly, ZM-3.0 shows the fastest electron injection rate and most efficient injection efficiency, which account for its significantly enhanced photocatalytic H_2 evolution performance.

In addition to the electrons injection from ZCIS to MoS_2 in photocatalysts, the amount of reactive sites in co-catalysts also plays an important role on their photocatalytic H_2 evolution activity. According to previous reports, the active sulfur atoms on the exposed edges of MoS_2 increase not only its electrocatalytic activity, but also photocatalytic activity.[16,36] These unsaturated active sulfur atoms bind strongly with H^+ in solution, which are easily reduced to H_2 by electrons. Due to the abundance of H^+ ions in lactic acid solution, unsaturated active sulfur atoms on the exposed edges of MoS_2 more easily capture H^+ ions, thus facilitating H_2 generation. Sulfur atoms on the basal plane with three-coordination, however, have no activity.[37] In this case, the enhancing photocatalytic activity from ZM-0.6 to ZM-3.0 is probably because of the increasing amount of active sites in MoS_2. While with further raising amount of MoS_2 to ZM-4.2 and ZM-6.0, aggregated MoS_2 nanoflowers start to appear, which greatly decrease the amount of unsaturated sulfur atoms and inhibit the electron mobility.[33] Thereby, ZM-3.0 exhibits the highest activity for photocatalytic H_2 generation.

Considering that the CB minimum position of few-layer MoS_2 locates at -0.13 V *vs.* NHE together with the above experimental results and analysis, a reasonable charge migration route in ZM-*X* heterostructure and the photocatalytic mechanism for H_2 evolution from water is proposed in Figure 10. Under visible light irradiation, electron-hole pairs are formed and separated in ZCIS microsphere. Some electrons approaching to MoS_2 are injected into MoS_2 in several picoseconds confirmed by the TDR results. Some other electrons far from MoS_2 may transfer to MoS_2 within tens picoseconds. These electrons subsequently move to active sites on MoS_2 to reduce H^+ to H_2. At the same time, the photogenerated holes are consumed by hole scavenger. Due to the fast

recombination of electron and hole pairs and lack of active sites, however, pure ZCIS possesses a poor H_2 evolution activity.

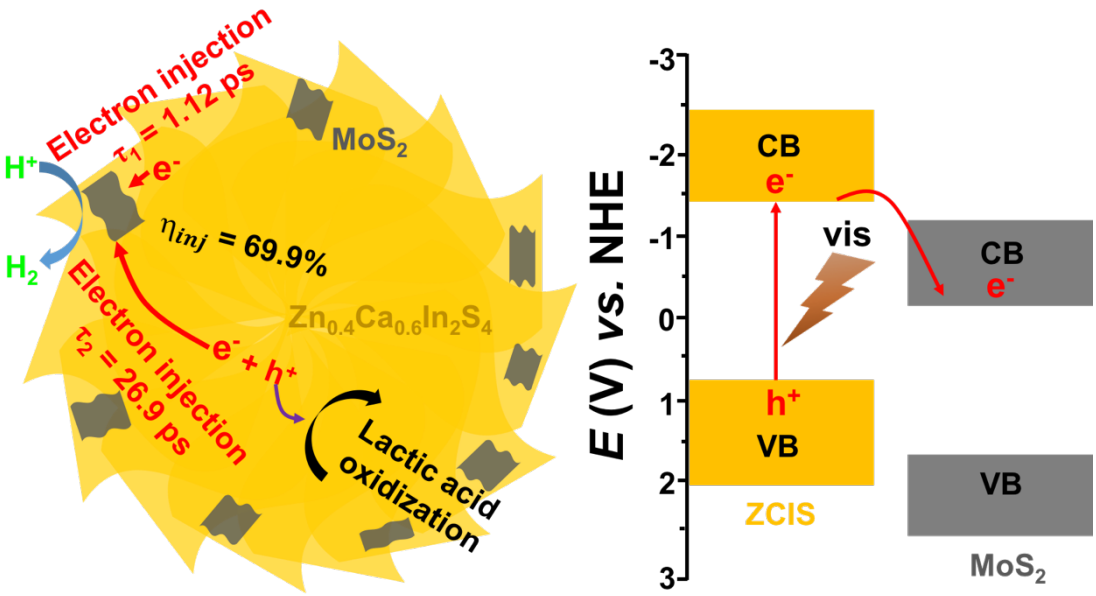

Figure 10 Schematic illustration of photogenerated charge transfer in ZM-3.0, and the proposed photocatalytic mechanism of H_2 evolution.

4. Conclusion

In summary, quaternary sulfur semiconductor $Zn_{0.4}Ca_{0.6}In_2S_4$ combined with different amount of layer structured MoS_2 are synthesized for visible-light-driven H_2 production from water. ZM-3.0 photocatalyst exhibits the maximum H_2 evolution rate of 3.5 μmol h^{-1} under visible light irradiation, which is about 27 times higher than that of bare ZCIS. The superior photocatalytic H_2 evolution activity of ZM-*X* is ascribed to 2D-2D structure, which greatly increases the contact surface area for charge transfer and supplies more active sites for photocatalytic reaction. The improved charge separation is confirmed by decreasing arc radius of Nyquist plot and significantly enhancement of photocurrent responses. Femtosecond time-resolved diffused reflectance spectroscopy gives a detail information of charge carrier transfer dynamics. It is demonstrated that the electrons could migrate from ZCIS to MoS_2 within several picoseconds, causing an efficient charge separation. In addition, the electron injection efficiency in ZM-3.0 is 69.9% and the injection time-scale is the shortest within only 1.12 ps, which are the highest and fastest. Overall, these results suggest that the

quaternary sulfur semiconductor can be served as a new kind of photocatalysts for water splitting with the characteristics of visible light responding and environmental friendly.

5. References

(1) Hou, Y.; Abrams, B. L.; Vesborg, P. C.; Björketun, M. E.; Herbst, K.; Bech, L.; Setti, A. M.; Damsgaard, C. D.; Pedersen, T.; Hansen, O. *Nat. Mater.* **2011,** 10 (6), 434.

(2) Tong, H.; Ouyang, S.; Bi, Y.; Umezawa, N.; Oshikiri, M.; Ye, J. *Adv. Mater.* **2012,** 24 (2), 229.

(3) Zhang, J.; Yu, J.; Zhang, Y.; Li, Q.; Gong, J. R. *Nano Lett.* **2011,** 11 (11), 4774.

(4) Wang, X.; Maeda, K.; Thomas, A.; Takanabe, K.; Xin, G.; Carlsson, J. M.; Domen, K.; Antonietti, M. *Nat. Mater.* **2009,** 8 (1), 76.

(5) Zhang, Z.; Huang, J.; Fang, Y.; Zhang, M.; Liu, K.; Dong, B. *Adv. Mater.* **2017,** 29 (18), 1606688.

(6) Asahi, R.; Morikawa, T.; Irie, H.; Ohwaki, T. *Chem. Rev.* **2014,** 114 (19), 9824.

(7) Simon, T.; Bouchonville, N.; Berr, M. J.; Vaneski, A.; Adrović, A.; Volbers, D.; Wyrwich, R.; Döblinger, M.; Susha, A. S.; Rogach, A. L.; Jäckel, F.; Stolarczyk, J. K.; Feldmann, J. *Nat. Mater.* **2014,** 13, 1013.

(8) Zeng, C.; Huang, H.; Zhang, T.; Dong, F.; Zhang, Y.; Hu, Y. *ACS Appl. Mater. Interfaces* **2017,** 9 (33), 27773.

(9) Sun, J.; Chen, G.; Xiong, G.; Pei, J.; Dong, H. *Int. J. Hydrogen Energy* **2013,** 38 (25), 10731.

(10) Ouyang, S.; Ye, J. *J. Am. Chem. Soc.* **2011,** 133 (20), 7757.

(11) Jiao, X.; Chen, Z.; Li, X.; Sun, Y.; Gao, S.; Yan, W.; Wang, C.; Zhang, Q.; Lin, Y.; Luo, Y.; Xie, Y. *J. Am. Chem. Soc.* **2017,** 139 (22), 7586.

(12) Yuan, Y.-J.; Chen, D.; Zhong, J.; Yang, L.-X.; Wang, J.; Liu, M.-J.; Tu, W.-G.; Yu, Z.-T.; Zou, Z.-G. *J. Mater. Chem. A* **2017,** 5 (30), 15771.

(13) Chang, K.; Mei, Z.; Wang, T.; Kang, Q.; Ouyang, S.; Ye, J. *ACS Nano* **2014,** 8 (7), 7078.

(14) Li, Y.; Wang, H.; Xie, L.; Liang, Y.; Hong, G.; Dai, H. *J. Am. Chem. Soc.* **2011,** 133 (19), 7296.

(15) Karunadasa, H. I.; Montalvo, E.; Sun, Y.; Majda, M.; Long, J. R.; Chang, C. J. *Science* **2012,** 335 (6069), 698.

(16) Chang, K.; Li, M.; Wang, T.; Ouyang, S.; Li, P.; Liu, L.; Ye, J. *Adv. Energy Mater.* **2015,** 5 (10), 1402279.

(17) Hinnemann, B.; Moses, P. G.; Bonde, J.; Jørgensen, K. P.; Nielsen, J. H.; Horch, S.; Chorkendorff, I.; Nørskov, J. K. *J. Am. Chem. Soc.* **2005,** 127 (15), 5308.

(18) Godin, R.; Wang, Y.; Zwijnenburg, M. A.; Tang, J.; Durrant, J. R. *J. Am. Chem.*

Soc. **2017,** 139 (14), 5216.
(19) Pendlebury, S. R.; Wang, X.; Le Formal, F.; Cornuz, M.; Kafizas, A.; Tilley, S. D.; Gratzel, M.; Durrant, J. R. *J. Am. Chem. Soc.* **2014,** 136 (28), 9854.
(20) Li, X. B.; Gao, Y. J.; Wang, Y.; Zhan, F.; Zhang, X. Y.; Kong, Q. Y.; Zhao, N. J.; Guo, Q.; Wu, H. L.; Li, Z. J.; Tao, Y.; Zhang, J. P.; Chen, B.; Tung, C. H.; Wu, L. Z. *J. Am. Chem. Soc.* **2017,** 139 (13), 4789.
(21) Yin, W.; Bai, L.; Zhu, Y.; Zhong, S.; Zhao, L.; Li, Z.; Bai, S. *ACS Appl. Mater. Interfaces* **2016,** 8 (35), 23133.
(22) Shi, X.; Fujitsuka, M.; Kim, S.; Majima, T. *Small* **2018**, 14, 1703277.
(23) Yang, M.-Q.; Han, C.; Xu, Y.-J. *J. Phys. Chem. C* **2015,** 119 (49), 27234.
(24) Li, Y.; Jin, R.; Xing, Y.; Li, J.; Song, S.; Liu, X.; Li, M.; Jin, R. *Adv. Energy Mater.* **2016,** 6 (24), 1601273.
(25) Zeng, C.; Hu, Y.; Huang, H. *ACS Sustainable Chem. Eng.* **2017,** 5 (5), 3897.
(26) Shi, X.; Fujitsuka, M.; Lou, Z.; Zhang, P.; Majima, T. *J. Mater. Chem. A* **2017,** 5 (20), 9671.
(27) Yuan, L.; Yang, M.-Q.; Xu, Y.-J. *J. Mater. Chem. A* **2014,** 2 (35), 14401.
(28) Ravensbergen, J.; Abdi, F. F.; van Santen, J. H.; Frese, R. N.; Dam, B.; van de Krol, R.; Kennis, J. T. M. *J. Phys. Chem. C* **2014,** 118 (48), 27793.
(29) Bian, Z.; Tachikawa, T.; Zhang, P.; Fujitsuka, M.; Majima, T. *J. Am. Chem. Soc.* **2014,** 136 (1), 458.
(30) Grigioni, I.; Stamplecoskie, K. G.; Selli, E.; Kamat, P. V. *J. Phys. Chem. C* **2015,** 119 (36), 20792.
(31) Milleville, C. C.; Pelcher, K. E.; Sfeir, M. Y.; Banerjee, S.; Watson, D. F. *J. Phys. Chem. C* **2016,** 120 (9), 5221.
(32) Yin, X.-L.; He, G.-Y.; Sun, B.; Jiang, W.-J.; Xue, D.-J.; Xia, A.-D.; Wan, L.-J.; Hu, J.-S. *Nano Energy* **2016,** 28, 319.
(33) Shi, X.; Fujitsuka, M.; Lou, Z.; Zhang, P.; Majima, T. *J. Mater. Chem. A* **2017**, 5 9671.
(34) Ong, W.-J.; Putri, L. K.; Tan, Y.-C.; Tan, L.-L.; Li, N.; Ng, Y. H.; Wen, X.; Chai, S.-P. *Nano Research* **2017,** 10 (5), 1673.
(35) Abdellah, M.; Žídek, K.; Zheng, K.; Chábera, P.; Messing, M. E.; Pullerits, T. *J. Phys. Chem. Lett.* **2013,** 4 (11), 1760.
(36) Yu, X.-Y.; Hu, H.; Wang, Y.; Chen, H.; Lou, X. W. *Angew. Chem. Int. Ed.* **2015,** 54 (25), 7395.
(37) Lukowski, M. A.; Daniel, A. S.; Meng, F.; Forticaux, A.; Li, L.; Jin, S. *J. Am. Chem. Soc.* **2013,** 135 (28), 10274.

General Conclusion

Throughout this dissertation, the photocatalytic activities of semiconductor-based composites have been studied. Importantly, the charge transfer kinetics was thoroughly explored using femtosecond time-resolved diffuse reflectance spectroscopy and single-particle confocal fluorescence microscopy technique.

In Chapter 1, Au-TiO_2 and 3D-array were fabricated to carefully explore the multi-scattering effect on the photocatalytic activity of H_2 generation. 3D-array exhibited a much higher photocatalytic activity of H_2 generation (3.5 folds under visible light irradiation, 1.4 folds under solar light irradiation) than Au-TiO_2. According to the single-particle plasmonic photoluminescence measurement, it was suggested that the hot electrons generated by AuNS under visible light irradiation play a significant role during the photocatalysis process. The higher activity of 3D-array is due to the elongation of light path length because of multi-scattering in-between Au-TiO_2.

In Chapter 2, a facile impregnated method was explored to synthesize products gradually varying from N-TiO_2 to N-TCN-x by mixing and calcining TiO_2 hollow nanospheres with cyanamide. Due to the mesoporous structure of TiO_2, g-C_3N_4 is formed both inside and outside of nanospheres. In addition, formation of g-C_3N_4 outside of TiO_2 small grains (3 nm) restrains their recrystallization to large particles (20 nm). Among series of N-TCN-x, N-TCN-700 exhibited the best activity in H_2 evolution of 296.4 μmol g^{-1} h^{-1} under visible light irradiation ($\lambda \geq 420$ nm) without any co-catalyst. Charge carrier lifetimes of N-TCN-x were measured by femtosecond time-resolved diffused reflectance spectroscopy to indicate that photogenerated electrons in CB of g-C_3N_4 transfers to that of N-TiO_2 within several to tens picoseconds, leading to efficient charge separation and photocatalytic activity.

In Chapter 3-1, facile processes were developed to synthesize g-C_3N_4-based hybrid photocatalysts containing different MoS_2 structures as co-catalyst, nanodot and monolayer. Photocatalytic H_2 evolution activity of MC-3.2% is 660 μmol g^{-1} h^{-1} under visible light irradiation, which is 7.9 times higher than that of Mix-6.4% (83.8 μmol g^{-1} h^{-1}). Charge carrier dynamics of g-C_3N_4, MC-3.2%, and Mix-6.4% measured by

femtosecond time-resolved diffused reflectance spectroscopy indicated that the electron injection took place within 1.7 ps in MC-3.2% compared to 4.0 ps in Mix-6.4% and the injection efficiencies were 73% and 36% in MC-3.2% and Mix-6.4%, respectively. In addition, MoS_2 nanodots with the small size contain more unsaturated active S atoms than MoS_2 monolayer, which could adsorb more H^+ ions.

In Chapter 3-2, quaternary sulfur semiconductor $Zn_{0.4}Ca_{0.6}In_2S_4$ (ZCIS) microspheres composed of cross-linked nanosheets and ZCIS microspheres modified with MoS_2 were designed and prepared *via* hydrothermal methods. Detailed characterizations indicated that the layer structured MoS_2 nanosheets are mainly deposited on the surface of ZCIS nanosheet to form a 2D-2D structure which increases greatly the contact surface area for charge transfer. It is demonstrated that ZM-3.0 (ZCIS with 3 wt% MoS_2 loading amount) exhibited the fastest electron injection within only 1.1 ps and the highest efficient injection efficiency of 70%. As a result, ZM-3.0 exhibited the H_2 evolution rate of 3.5 μmol h^{-1} under visible light irradiation ($\lambda \geq 420$ nm), which is 27 times higher than that of ZCIS (0.13 μmol h^{-1}).

To conclude, this thesis introduces three methods to increase the performances of semiconductors for photocatalytic hydrogen/oxygen generation processes, which are enhancing incident light absorption, retardation of electron-hole pairs recombination and providing sufficient active sites for photocatalysis reactions. All works help us to gain an in-depth understanding on photocatalytic activities. With intensive investigations of charge transfer kinetics in semiconductor-based materials, photophysical properties will be gradually unveiled, which is a fundamental guidance for designing photocatalysts with novel structure and extraordinary performance. The photocatalytic reactions are still at the early stage of development, the promising future of it will be foreseen as the basic building block for the resolving energy shortcoming and environment pollutant.

List of Publications

1. 3D-array of Au-TiO_2 Yolk-shell as Plasmonic Photocatalyst Boosting Multi-Scattering with Enhanced Hydrogen Evolution
   Xiaowei Shi, Zaizhu Lou, Peng Zhang, Mamoru Fujitsuka, and Tetsuro Majima
   ACS Appl. Mater. Interface **2016**, *8*, 31738-31745.

2. *In situ* nitrogen-doped hollow-TiO_2/g-C_3N_4 composite photocatalysts with efficient charge separation boosting water reduction under visible light
   Xiaowei Shi, Mamoru Fujitsuka, Zaizhu Lou, Peng Zhang, and Tesuro Majima.
   Journal of Materials Chemistry A **2017**, *5*, 9671-9681.

3. Faster Electron Injection and More Active Sites for Efficient Photocatalytic H_2 Evolution in g-C_3N_4 /MoS_2 Hybrid
   Xiaowei Shi, Mamoru Fujitsuka, Sooyeon Kim, and Tetsuro Majima.
   Small 2018, 14, 1703277.

4. Electron Transfer Dynamics of Quaternary Sulfur Semiconductor/MoS_2 Layer-on-Layer for Efficient Visible-Light H_2 Evolution
   Xiaowei Shi, Mamoru Fujitsuka, and Tetsuro Majima.
   Appl. Catal. B: Environ. **2018**, 235, 9-16.

Other publication

1. *In Situ* Observation of Single Au Triangular Nanoprism Etching to Various Shapes for Plasmonic Photocatalytic Hydrogen Generation
   Zaizhu Lou, Sooyeon Kim, Peng Zhang, Xiaowei Shi, Mamoru Fujitsuka, and Tetsuro Majima.
   ACS Nano, **2017**, 11, 968-974.

2. *In Situ* Monitoring Charge Transfer from TiO_2 to NiS During NiS Photodeposition on TiO_2 Mesocrystal with Single-particle Photoluminescence for Enhancing Photocatalytic Hydrogen Production
   under preparation.

Acknowledgements

The author wishes to express his sincerest gratitude to Professor Tetsuro Majima, the Institute of Science and Industrial Research (SANKEN), Osaka University, for his invaluable supervision, guidance, and advice throughout the doctoral study.

The author deeply appreciates Assistant Professor Mamoru Fujitsuka for his helpful guidance of research activities in laser flash photolysis. The author is also indebted to Professor Akira Sugimoto, Professor Mikiji Miyata, Assistant Professor Yasuko Osakada, and Assistant Professor Sooyeon Kim for their kind helps and advice.

The author would like to thank all the members of Professor Majima's research group, including Dr. Shaoqing Song, Dr. Zaizhu Lou, Dr. Mingshan Zhu, Dr. Peng Zhang, Dr. Shih-Hsun Lin, Dr. Chao Lu, Dr. Xiaoyan Cai, Dr. Aihua Yan, Dr. Jing Xu, Dr. Atsushi Tanaka, Dr. Ossama Elbanna, Dr. Ke Zhang, Mr. Daming Ruan, Miss Jie Xu, Mr. Jiawei Xue, Mr. Bo Zhuang, Miss Ayaka Kuroda, Mr. Kota Nomura, Mr. Yoji Yamamoto, Mr. Yuma Ichinose, Mr. Yang Zhou, Mr. Kawakami Hiroki, Miss Kubo Haruna, and Miss Sanae Tominaga (SANKEN) for their encouragement and help from research discussions to daily lives in Japan. In addition, the author gives thanks to China Scholarship Council (CSC) for their financial support during my doctor course in these three years.

Finally, the author expresses thank to his family, father Minjiang Shi, mother Yanju Chen, and wife Shiting Wu, for their endless supports, encouragements and love during his doctoral study.

SHI XIAOWEI

2018